The Pennsylvania State University

The Graduate School

College of Earth and Mineral Sciences

HYDRODYNAMICS OF THE US MID-ATLANTIC CONTINENTAL SLOPE,

OFFSHORE NEW JERSEY

A Thesis in

Geosciences

by

Brandon Dugan

Submitted in Partial Fulfillment
of the Requirements
for the Degree of

Doctor of Philosophy

May 2003

We approve the thesis of Brandon Dugan.

Date of Signature

_____   _____

Peter B. Flemings
Associate Professor of Geosciences
Thesis Advisor
Chair of Committee

_____   _____

Richard B. Alley
Professor of Geosciences

_____   _____

Derek Elsworth
Professor of Energy and Geo-Environmental Engineering

_____   _____

Rudy L. Slingerland
Professor of Geosciences

_____   _____

Barry Voight
Professor of Geosciences

_____   _____

Peter Deines
Professor of Geosciences
Associate Head for Graduate Programs and Research

Abstract

Fluid pressures in Miocene-Pleistocene sediments of the US mid-Atlantic continental slope approach the lithostatic stress and are an important control on the stability of the slope. Fluid pressures in excess of hydrostatic were generated by regional depositional patterns and sedimentation rates. Fluid migration within porous and permeable Miocene silty sand layers redistributed pressure and generated low vertical effective stress where Pleistocene overburden is thin. Fluid pressures that nearly equal the overburden stress cause failure on the lower slope and initiate headward erosion; we interpret this process is contributes to canyon formation along the US mid-Atlantic margin. Consolidation is a function of stress history; therefore we can interpret fluid overpressure and effective stress from porosity of samples from Ocean Drilling Program (ODP) Sites 902, 903, 904, and 1073. Stress and pressure interpretations from consolidation experiments on samples from ODP Site 1073 are consistent with porosity-predicted conditions. The borehole data were used to calibrate a relationship between seismic interval velocity and vertical effective stress. Seismic analyses predict low effective stress and high overpressure in Miocene and Pleistocene sediments where Pleistocene accumulation was greatest. Two-dimensional sedimentation-flow models, using laboratory-measured rock properties, simulated how rapid deposition of Miocene and Pleistocene sediments along the upper slope generated significant excess pressures that drove fluids upward toward the seafloor and laterally to the middle slope in permeable Miocene sediments. Along the Hudson Apron, sedimenta-

tion and pore pressure generated near-failure conditions, but stability analyses did not predict failures. This is compatible with observations of the smooth apron. Southwest of the Hudson Apron, where canyons exist, Pleistocene accumulations are thin and Miocene sedimentation rates were high. We interpret that the Miocene-Pleistocene deposition generated excess fluid pressures and a focussed flow field that generated failures, which in turn led to the formation of canyons on the middle and lower slope.

Table of Contents

List of Figures

List of Tables

Acknowledgements

Chapter 1: Overpressure and Fluid Flow in the New Jersey Continental Slope: Implications for Slope Failure and Cold Seeps

Abstract

Miocene through Pleistocene sediments on the New Jersey continental slope (ODP Site 1073) are undercompacted (porosity between 40 - 65%) to 640 meters below sea floor and this is interpreted to record fluid pressures that reach 95% of the lithostatic stress. A two-dimensional model, where rapid Pleistocene sedimentation loads permeable sandy silt of Miocene age, successfully predicts the observed pressures. The model describes how lateral pressure equilibration in permeable beds produces fluid pressures that approach the lithostatic stress where overburden is thin. This type of pressure transfer may cause slope failure and drive cold seeps on passive margins around the world.

1.1 Introduction

Rapid sediment loading (> 1 mm yr^{-1}) is documented as a source of overpressure (P^*, pressure in excess of hydrostatic) in basins around the world (Fertl, 1976; Rubey and Hubbert, 1959). There is a suite of models that describe how overpressure is generated during rapid deposition (Gibson, 1958; Bredehoeft and Hanshaw, 1968; Koppula and Morgenstern, 1982; Bethke, 1986). These models quantify the rock properties and sedimentation

rates required to generate and maintain overpressure. The US mid-Atlantic continental slope offshore New Jersey is a type location to study the relation between overpressure, fluid flow, and slope stability because of the existence of physical properties and sedimentation data, and because the margin has failed and stable slopes. Mass and volume measurements of wet and dry core samples provide porosity data (Austin *et al*., 1998) that we use to document overpressures on the New Jersey continental slope (Figure 1.1). Forward sedimentation models are used to simulate the spatial and temporal evolution of pressure and stress for the slope.

1.2 Porosity, Stress, and Pressure

We divide the porosity (ϕ) at ODP Site 1073 into three depth intervals (Figure 1.2). Zone 1 extends from the sea floor to 100 mbsf (meters below sea floor); in this zone, porosity exponentially decreases from 62% to about 45%. Zone 2 is 450 m thick, underlies zone 1, and has nearly constant porosity ($\phi \sim 45\%$). Zone 3, the deepest section, begins with an abrupt increase in porosity that is followed by a rapid porosity decrease. These porosity zones may record three distinct pressure regimes: zone 1 is normally compacted and hydrostatically pressured; zone 2 is underconsolidated, overpressured, and has a lithostatic fluid pressure gradient; and zone 3 is underconsolidated, overpressured, and has a hydrostatic fluid pressure gradient.
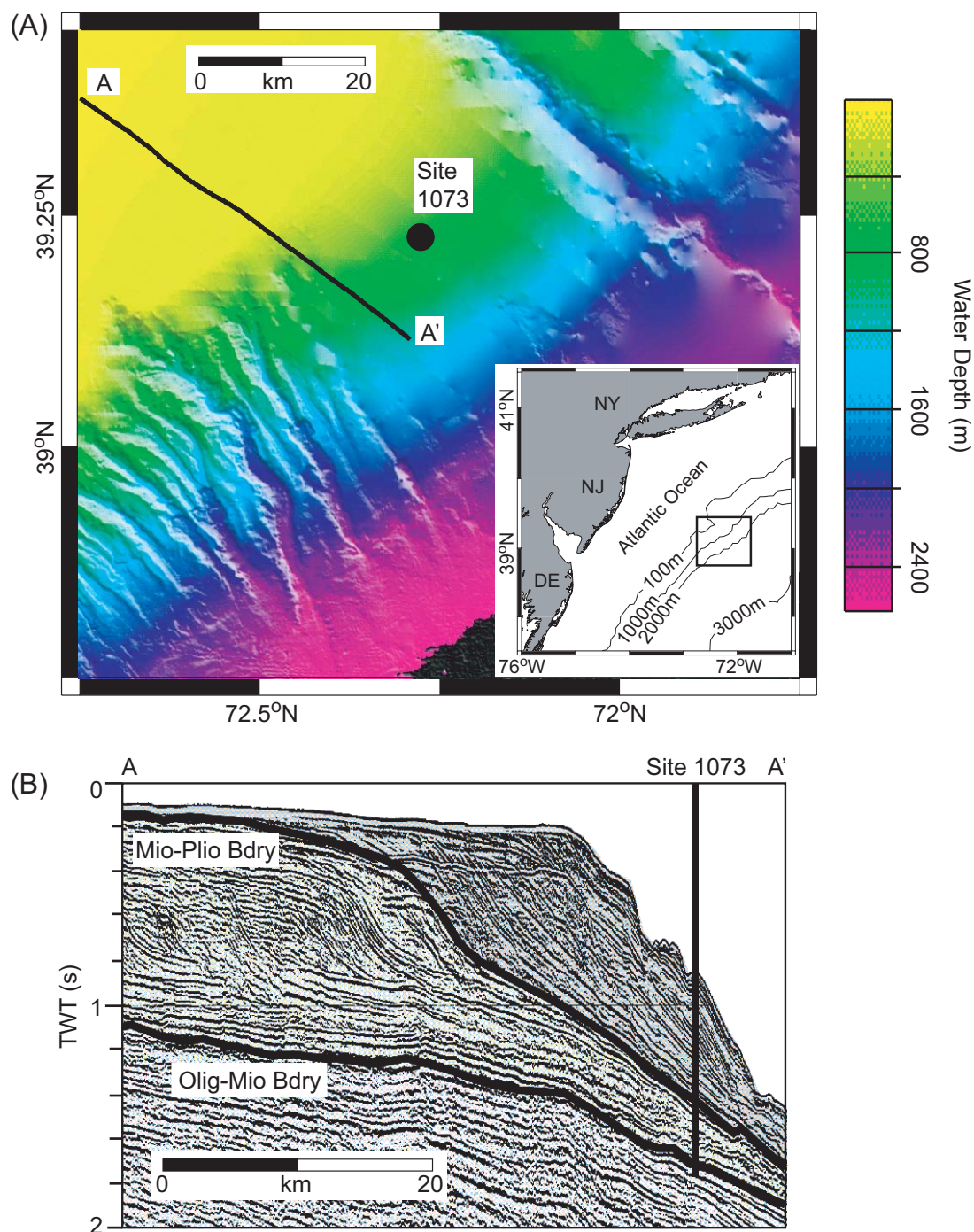
Figure 1.1: (A) Bathymetric map of the New Jersey continental slope. ODP Leg 174A Site 1073 is located in 639 m water depth on a smooth portion of the slope. Along the smooth slope, Pleistocene sediments completely cover the Miocene strata whereas where canyons are present, the Miocene is exposed (Hampson and Robb, 1984). (B) Dip seismic line 1002 shows the regional Miocene-Pleistocene stratigraphy. Black lines identify age boundaries (Bdry).
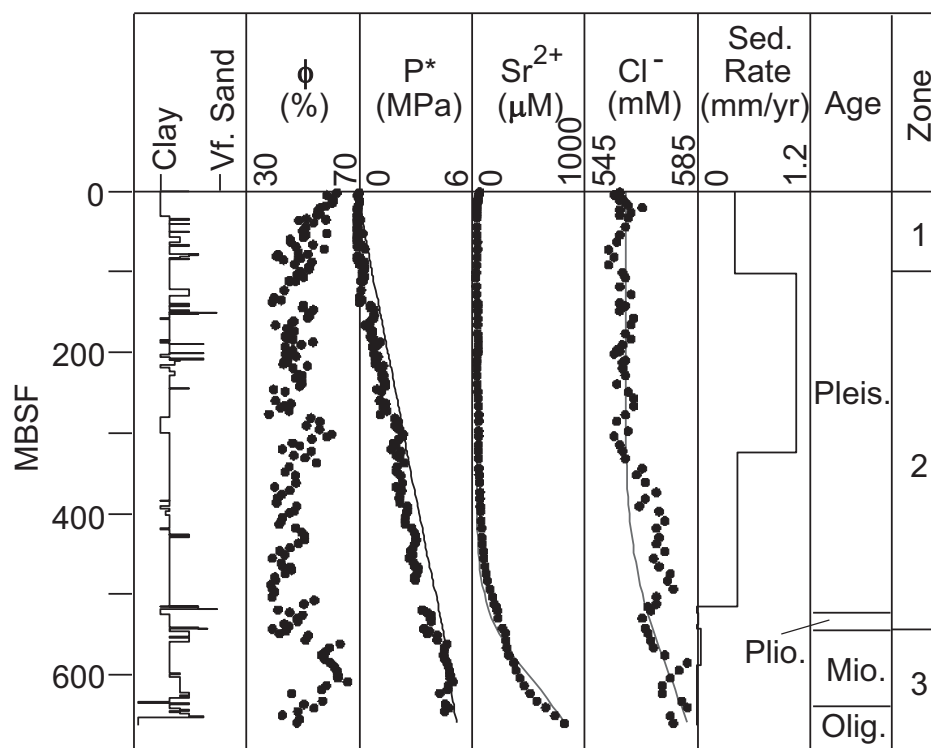
Figure 1.2: Core data from ODP Site 1073 (Figure 1.1) (Shipboard Scientific Party, 1998). Porosity was determined from wet and dry measurements of mass and volume of core samples. *P** are overpressures predicted from porosity. The solid line on the *P** plot is the reduced lithostatic stress (S_v-$\rho_w gz$). Diffusion-modeled Sr^{2+} and Cl^- profiles are solid lines; observations are circles. Pleistocene sedimentation rates far exceeded Miocene and Pliocene sedimentation rates as inferred from biostratigraphic data.

We quantify this interpretation by employing an empirical relation between porosity and vertical effective stress ($\sigma_v = S_v\text{-}\rho_w gz\text{-}P^*$) in the silt and clay sediments (Rubey and Hubbert, 1959; Hart *et al*., 1995).

$$\phi = \phi_o e^{-\beta\sigma_v} \tag{1.1}$$

ϕ_o is a reference porosity, β is the bulk compressibility, S_v is the overburden (Appendix A), ρ_w is the water density, g is the acceleration due to gravity, and z is the depth below sea surface (Table 1.1). This relationship is constrained ($\phi_o = 61\%$ and $\beta = 0.44$ MPa^{-1}) in zone 1 (Appendix A) (Athy, 1930; Hart *et al*., 1995). After constraining β and ϕ_o, Equation 1.1 is rearranged and porosity is used to predict overpressure deeper in the section. The regression (Equation 1.1) and pressure prediction (Equation 1.2) are only performed on clay and silt sediments.

$$P^* = S_v - \frac{1}{\beta}\ln\left(\frac{\phi_o}{\phi}\right) - \rho_w gz \tag{1.2}$$

In zone 1, where the model was constrained, predicted pressures are hydrostatic. Predicted pressures in zone 2 are 95% of the lithostatic stress (Figure 1.2). The predicted overpressures at the top of zone 3 approach the reduced lithostatic stress and remain constant at 4.8 MPa through the zone. The constant overpressure indicates a hydrostatic fluid pressure gradient in zone 3.

Table 1.1: Nomenclature

Variable	Definition	Dimensions
g	acceleration due to gravity	L/T^2
k	permeability	L^2
k_h	bedding-parallel permeability	L^2
k_v	bedding-perpendicular permeability	L^2
P	fluid pressure	M/LT^2
$P*$	overpressure	M/LT^2
P_ϕ	porosity-predicted overpressure	M/LT^2
S_t	storage coefficient	LT^2/M
S_v	overburden stress	M/LT^2
S_{vmax}	maximum overburden stress	M/LT^2
t	time	T
TD	total sediment thickness	L
z	depth	L
β	bulk compressibility	LT^2/M
β_f	fluid compressibility	LT^2/M
ϕ	porosity	dimensionless
ϕ_o	reference porosity	dimensionless
ρ_w	water density	M/L^3
σ_v	vertical effective stress	M/LT^2
μ	dynamic viscosity	M/LT

1.3 Sedimentation-Flow Modelling

A sedimentation-compaction model (Gibson, 1958; Gordon and Flemings, 1998) is used to simulate the fluid pressure evolution for the New Jersey slope at Site 1073. Equation 1.3 is derived in material coordinates, tracks the solid grains during burial, and is solved with a finite element approach.

$$\frac{DP}{Dt} = \left[\frac{k(1-\phi)^2}{S_t\mu}\right]\nabla^2 P^* + \left[\frac{\phi\beta}{S_t(1-\phi)}\right]\frac{DS_v}{Dt} \tag{1.3}$$

where k is the permeability, μ is the dynamic viscosity, and S_t is the storage coefficient [$S_t = \phi\beta/(1-\phi)+\phi\beta_f$] assuming incompressible grains (Table 1.1).

The model assumes that sediment loading (DS_v/Dt) is the only source of fluid pressure, the sediments compact according to Equation 1.1, and fluid flow follows Darcy's law. The base of the model is a no-flow boundary. The upper boundary (sea floor) is a constant pressure boundary ($P^* = 0$). All sediments are deposited with 61% initial porosity (ϕ_o) and with a bulk compressibility (β) equal to 0.44 MPa^{-1} as determined at Site 1073. Compaction is assumed to be irreversible (Appendix A) (Lambe and Whitman, 1979; Craig, 1992). The bedding-perpendicular permeability (k_v) assigned to the Plio-Pleistocene sediments is 1x10^{-18} m^2. The permeability is constrained by experiments on nearby sediments of similar age and lithology (Blum *et al.*, 1996). The model permeability for the Miocene strata is higher ($k_v = 3$x10^{-16} m^2) than that of the Plio-Pleistocene sediments because they

are coarser grained (Figure 1.2). The bedding-parallel permeability (k_h) for all sediments is assumed to be one order of magnitude greater than k_v ($k_h = 10k_v$).

We first solve Equation 1.3 in one-dimension and then solve it for a two-dimensional system. In the one-dimensional model, the Miocene sediments are assumed to be hydrostatically pressured before they are loaded by the Plio-Pleistocene strata. The modeled Plio-Pleistocene sedimentation rate follows that observed at Site 1073 (Figure 1.2). At the end of the Plio-Pleistocene deposition, modeled pressures for zone 1 exceed those predicted from porosity (Figure 1.3A). Modeled pressures in zones 2 and 3 reach only 25% of the porosity-predicted pressures (Figure 1.3A). To match the porosity-predicted pressures, the model permeability must be decreased two orders of magnitude. This is representative of a homogeneous clay and is unrealistically low for the silt-dominated New Jersey slope (Strack, 1989; Neuzil, 1994).

In the two-dimensional model, a 20 km wide, 0.1 km thick layer of hydrostatically pressured, permeable Miocene sandy silt is buried for one million years by lower permeability Plio-Pleistocene silt and clay (Figure 1.3). The model sedimentation rate (DS_v/Dt) decreases linearly from the left boundary to the right boundary and varies temporally following the observations at Site 1073 (Figure 1.2).
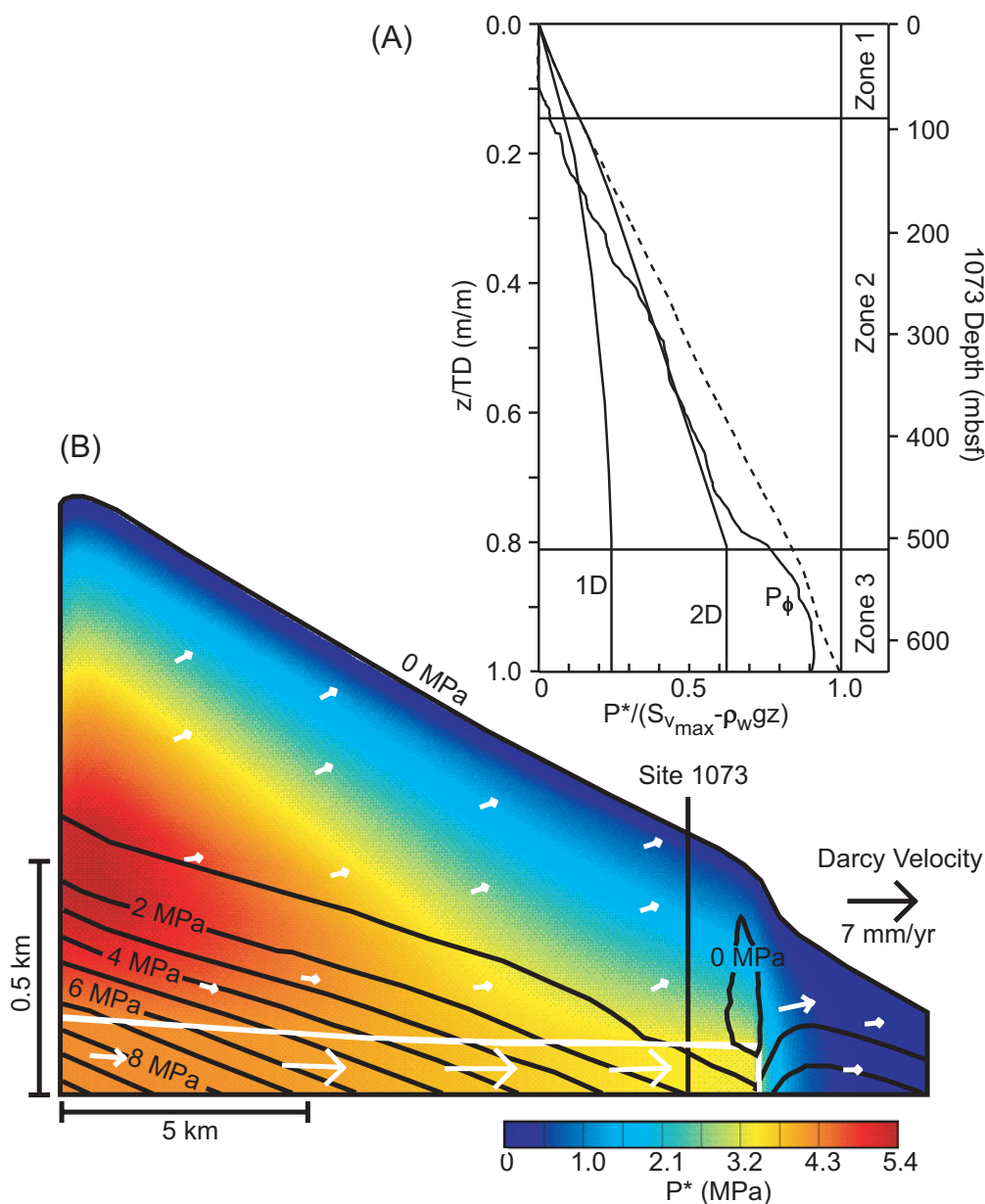
Figure 1.3: (A) Normalized plot of overpressures for Site 1073. *TD* **is the total sediment thickness at Site 1073 and** *z* **is the distance below the sea floor. The dashed line is the reduced lithostat. Solid lines are one-dimensional model (1D), two-dimensional model (2D), and porosity-predicted (P$_\phi$) pressures at Site 1073. Porosity zones and measured depth for Site 1073 are labelled for reference (Figure 1.2). (B) Simulated two-dimensional vertical effective stress (contour interval = 1 MPa), overpressure (color contours), and flow fields for the New Jersey slope after one million years of simulation. The left edge (upper slope) is a no flow boundary and the right edge (lower slope) is a constant pressure boundary (*P* = 0*). The model geometry is constrained from regional seismic data (Figure 1.1B). The white surface is the Miocene-Pliocene boundary. Vertical effective stress is less than 1 MPa for much of the section and is < 0 MPa above the toe of the Miocene bed. The low vertical effective stress indicates that the lower slope is at near failure conditions.**

The two-dimensional model predicts a large lateral flux along the higher permeability Miocene bed, where Darcy velocities reach 7 mm yr^{-1} (Figure 1.3B). At the toe of the Miocene strata, fluids are expelled laterally and vertically upward with an average Darcy velocity of 0.5 mm yr^{-1}. At the left edge of the model domain, where deposition is most rapid, fluids flow slowly (< 0.05 mm yr^{-1}) upward to the sea floor and downward to the permeable Miocene section. The shallow Pleistocene sediments (less than 100 mbsf) have low Darcy velocities < 0.005 mm yr^{-1}.

1.4 Discussion and Summary

Lateral pressure transfer towards the toe of the Miocene lens in the two-dimensional model elevates pressures at Site 1073 relative to the one-dimensional model (Figure 1.3A). The two-dimensional model pressures in the Plio-Pleistocene section (zones 1 and 2) are nearly lithostatic. The modeled pressures match the porosity-predicted pressures from 250-500 mbsf (Figure 1.3A). In zone 3, the model predicts high overpressures (68% of the nearly lithostatic overpressure predicted from porosity) and a hydrostatic gradient (Figure 1.3A). The results are consistent with the porosity-predicted pressures and gradients in zones 2 and 3, but the modeled pressures and gradients exceed the porosity-predicted pressures in zone 1 (Figure 1.3A). The difference between the model results and pressures predicted from porosity in zone 1 may result from the assumption of constant permeability. The sediments in zone 1 are probably more permeable than the deeper sediments because of their high porosity; this would aid fluid drainage and maintain hydrostatic pressure as is observed. Two effects may control the difference between modeled and porosity-predicted

pressures in zone 3. First, the porosity-vertical effective stress model constrained in porosity zone 1 may not describe the behavior of deeper sediments. A second possible explanation is that the Miocene sediments terminate at or near Site 1073 (Figure 1.3B). In this case, the model would predict pressures in zone 3 that are closer to the porosity-predicted pressures.

Sr^{2+} and Cl^- porewater concentrations are greatest in the Oligocene section and decrease upward to modern sea-water values (Figure 1.2). Brines that originated from dissolution of deeper Jurassic salt may be the source of the high Cl^- concentrations (Mountain *et al.*, 1994). Recrystallization or dissolution of Sr-rich carbonates at greater depths may have produced the high Sr^{2+} concentrations in Oligocene porewaters (Mountain *et al.*, 1994). We use these data as a geochemical tracer to demonstrate that the present day concentrations are compatible with the two-dimensional flow model. In a one-dimensional diffusion model, we assumed an initial Oligocene porewater concentration equal to that observed today, and we assumed the overlying beds have sea water concentrations. Oligocene porewater concentrations are modeled as constant because of the high concentration sources at depth. Sr^{2+} and Cl^- diffusivities are constant, $9.3 \times 10^{-11} m^2 s^{-1}$ and $2.5 \times 10^{-10} m^2 s^{-1}$, respectively, and are scaled for diffusion in a porous medium (Li and Gregory, 1974; Domenico and Schwartz, 1990). In much of the model domain, the modeled concentrations are less than the observed after one million years of diffusion (Figure 1.2). The predicted Sr^{2+} concentrations are 50% of those observed from 450 to 550 mbsf and the Cl^- concentrations are 5% less than those observed from 350 to 500 mbsf. These results suggest that the porewater chemistry is dominated by diffusive mass transport. The Darcy

velocities predicted by the two-dimensional flow model may provide the advective transport to account for the difference between the observed and predicted concentrations.

The flow model predicts that lateral flow along permeable pathways will decrease vertical effective stress where overburden is thin. As the vertical effective stress decreases to a critical value (Figure 1.3B), the sediments will become unstable (Terzaghi, 1943; Hubbert and Rubey, 1959; Rona and Clay, 1967). Sediment failure on the lower slope may act as a catalyst to headward erosion, a mechanism that contributes to submarine canyon formation (Figure 1.1A) (Robb *et al*., 1981; McGregor *et al*., 1982; Pratson and Coakley, 1996). Previous studies suggested that high fluid pressures aided canyon formation (Johnson, 1939; Rona, 1969; Robb, 1990); however, these studies were neglected because they called on a permeable aquifer that extends hundreds of kilometers across the continental shelf to create artesian conditions on the slope (Shepard, 1981). This lack of hydraulic connectivity from the shoreline to the slope prevents topographic flow from contributing to the elevated pressures on the slope. Our flow model suggests that the progradation of any low-permeability shelf margin over more permeable strata will provide a mechanism to focus flow and generate overpressure, slope failure, and slope seeps. Although this is a two-dimensional model, we envision that flow will occur in three dimensions, outward and along-slope toward any zone where the overburden is thin.

The flow model provides an explanation for the origin and distribution of sea floor seeps. Fluid expulsion would be expected at the toe of the slope where the pressure gradients are high. Seeps and geysers are reported on the lower slope of the New Jersey continental margin (Rona *et al*., 2000) and in many other rapidly loaded passive margins (MacDonald

et al., 1990; MacDonald *et al*., 1996). On the New Jersey slope, these seeps will be great-

est within canyons where high-permeability Miocene sediments are exposed. High-flux

seeps may themselves contribute to grain-by-grain erosion on the slope and on canyon

walls (Robb, 1990). Solutes in seep fluids can provide energy sources for biological com-

munities (Paull *et al*., 1984; Olu *et al*., 1997).

The observations at Site 1073 and model results for the slope show that the New Jersey

slope is overpressured and has low vertical effective stress below 100 mbsf. Recently dis-

covered sea floor cracks offshore Virginia and North Carolina may represent locally unsta-

ble conditions and low vertical effective stresses near the continental shelf-slope break

(Driscoll *et al*., 2000). Elevated fluid pressures caused by rapid sediment loading, as we

have modeled, may be a mechanism responsible for this low effective stress and slope

instability. The model predicts that rapid loading in any basin produces high pressures

near the depocenter and that lateral transfer of pressure creates near-constant overpressure

in permeable lenses. The lateral pressure transfer raises vertical effective stress where

overburden is thick and decreases vertical effective stress where overburden is thin. These

pressure and stress profiles are created solely by differential loading and variations in rock

properties (such as permeability and bulk compressibility) and do not require any other

mechanism to lower the permeability and increase overpressure (Kooi, 1997; Revil *et al*.,

1998). The model provides a simple mechanism for overpressure generation and slope

failure that may be active in basins around the world. The model also provides an explana-

tion for high overpressures that begin at shallow depth on the middle and lower slope.

These results revitalize the hypothesis that overpressure contributes to slope geomorphol-

ogy (Rona, 1969; Shepard, 1981; Robb, 1990). The lateral flow predicted describes how compaction-driven flow can contribute to the distribution, diversity, and size of cold seeps and the communities that thrive on the solutes in the seep fluids.

Acknowledgements

Appendix A: Model Constraints

A regression of Equation 1.1 is performed in zone 1, where *P** is assumed to be zero.

Hydrostatic pressures are assumed because the porosity decreases steadily through zone 1

(Athy, 1930; Hart *et al*., 1995). S_v is calculated by integrating the core density and

accounting for the water depth. β was also estimated for the Miocene sediments by assum-

ing that they were deposited at hydrostatic conditions. The results provide a β for deep

sediments that is similar to that inferred in zone 1. An alternative explanation of the

observed porosity-depth signature is that the deeper section is hydrostatically pressured;

but the compressibility (β) of the deeper sediments for hydrostatic pressures is only 10%

of that of the shallower sediments. We do not believe that sediment properties could have

changed this significantly within the same effective stress regime (Dugan *et al*., 2002) and

therefore interpret the sediments to be overpressured. For sediments that are unloading or

reloading, the sediments are considered to be stiffer than during initial consolidation so the

bulk compressibility is assumed to be 0.44×10^{-3} MPa^{-1}.

References

Athy, L.F., 1930, Density, Porosity, and Compaction of Sedimentary Rocks, AAPG Bulletin, v. 14, p. 1-24.

Austin Jr., J.A., Christie-Blick, N., Malone, M.J., *et al*., 1998, Proceedings of the Ocean Drilling Program, Initial Reports, College Station, Ocean Drilling Program, 324 p.

Bethke, C.M., 1986, Inverse Hydrologic Analysis of the Distribution and Origin of Gulf Coast-Type Geopressured Zones, Journal of Geophysical Research, v. 91, p. 6535-6545.

Blum, P., Xu, J., and Donthireddy, S., 1996, Geotechnical properties of Pleistocene sediments from the New Jersey upper continental slope, *in* Mountain, G.S., Miller, K.G., Poag, C.W., and Twichell, D.C. (eds.), Proceedings of the Ocean Drilling Program, Scientific Results, Volume 150, College Station, Ocean Drilling Program, p. 377-384.

Bredehoeft, and Hanshaw, 1968, On the Maintenance of Anomalous Fluid Pressures, GSA Bulletin, v. 79, p. 1097-1106.

Craig, R.F., 1992, Soil Mechanics, London, Chapman & Hall, 427 p.

Domenico, P.A., and Schwartz, F.W., 1990, Physical and Chemical Hydrogeology, New York, Wiley, 824 p.

Driscoll, N.W., Weissel, J.K., and Goff, J.A., 2000, Potential for large-scale submarine slope failure and tsunami generation along the US Mid-Atlantic coast, Geology, v. 28, p. 407-410.

Dugan, B., Olgaard, D.L., Flemings, P.B., and Gooch, M.J., 2002, Data report: Bulk physical properties of sediments from ODP site 1073, *in* Christie-Blick, N., Austin Jr., J.A., and Malone, M.J. (eds.), Proceedings of the Ocean Drilling Program, Scientific Results, Volume 174A, College Station, Ocean Drilling Program, p. 1-62.

Fertl, W.H., 1976, Abnormal Formation Pressures: Implications to Exploration, Drilling, and Production of Oil and Gas Resources, Amsterdam, Elsevier, 382 p.

Gibson, R.E., 1958, The progress of consolidation in a clay layer increasing in thickness with time, Geotechnique, v. 8, p. 171-182.

Gordon, D.S., and Flemings, P.B., 1998, Generation of overpressure and compaction-driven fluid flow in a Plio-Pleistocene growth-faulted basin, Eugene Island 330, offshore Louisiana, Basin Research, v. 10, p. 177-196.

Hampson, J.C., and Robb, J.M., 1984, A Geologic Map of the Continental Slope off New Jersey, Lindenkohl to Toms Canyons, Boulder, USGS.

Hart, B.S., Flemings, P.B., and Deshpande, A., 1995, Porosity and pressure; role of compaction disequilibrium in the development of geopressures in a Gulf Coast Pleistocene basin, Geology, v. 23, p. 45-48.

Hubbert, M.K., and Rubey, W.W., 1959, Mechanics of fluid-filled porous solids and its application to overthrust faulting, part 1 of role of fluid pressure in mechanics of overthrust faulting, GSA Bulletin, v. 70, p. 115-166.

Johnson, D.W., 1939, The Origin of Submarine Canyons: A Critical Review of Hypotheses, New York, Hafner, 126 p.

Kooi, H., 1997, Insufficiency of compaction disequilibrium as the sole cause of high pore fluid pressures in pre-Cenozoic sediments, Basin Research, v. 9, p. 227-241.

Koppula, S.D., and Morgenstern, N.R., 1982, On the consolidation of sedimenting clays, Canadian Geotechnical Journal, v. 19, p. 260-268.

Lambe, T.W., and Whitman, R.V., 1979, Soil Mechanics: SI Version, New York, John Wiley & Sons, 553 p.

Li, Y.H., and Gregory, S., 1974, Diffusion of ions in sea water and in deep-sea sediments, Geochemica et Cosmochimica Acta, v. 38, p. 703-714.

MacDonald, I.R., Guinasso Jr., N.L., Reilly, J.F., Brooks, J.M., Callender, W.R., and Gabrielle, S.G., 1990, Gulf of Mexico hydrocarbon seep communities; VI, patterns in community structure and habitat, Geo-Marine Letters, v. 10, p. 244-252.

MacDonald, I.R., Reilly, J.F., Best, S.E., Venkataramaiah, R., Sassen, R., Guinasso Jr., N.L., and Amos, J., 1996, Remote sensing inventory of active oil seeps and chemosynthetic communities in the northern Gulf of Mexico, *in* Schumacher, D., and Abrams, M.A. (eds.), AAPG Memoir 66, Tulsa, American Association of Petroleum Geologists, p. 27-37.

McGregor, B.A., Stubblefield, W.L., Ryan, W.B., and Twichell, D.C., 1982, Wilmington submarine canyon; a marine fluvial-like system, Geology, v. 10, p. 27-30.

Mountain, G.S., Miller, K.G., Blum, P., *et al*., 1994, Proceedings of the Ocean Drilling Program, Initial Reports, College Station, Ocean Drilling Program, 883 p.

Neuzil, C.E., 1994, How permeable are clays and shales?, Water Resources Research, v. 30, p. 145-150.

Olu, K., Lance, S., Sibuet, M., Henry, P., Fiala-Medioni, A., and Dinet, A., 1997, Cold seep communities as indicators of fluid expulsion patterns through mud volcanoes seaward of the Barbados accretionary prism, Deep-Sea Research Part I, v. 44, p. 811-841.

Paull, C.K., Hecker, B., Commeau, R., Freeman-Lynde, R.P., Neumann, C., Corso, W.P., Golubic, S., Hook, J.E., Sikes, E., and Curray, J., 1984, Biological communities at the Florida Escarpment resemble hydrothermal vent taxa, Science, v. 226, p. 965-967.

Pratson, L.F., and Coakley, B.J., 1996, A model for the headward erosion of submarine canyons induced by downslope-eroding sediment flows, GSA Bulletin, v. 108, p. 225-234.

Revil, A., Cathles III, L.M., Shosa, J.D., Pezard, P.A., and de Larouziere, F.D., 1998, Capillary sealing in sedimentary basins: a clear field example, Geophysical Research Letters, v. 25, p. 389-392.

Robb, J.M., 1990, Groundwater processes in the submarine environment, *in* Higgins, C.G., and Coates, D.R. (eds.), Groundwater Geomorphology: The Role of Subsurface Water in Earth-Surface Processes and Landforms, Boulder, Geological Society of America, p. 267-281.

Robb, J.M., Hampson Jr., J.C., and Twichell, D.C., 1981, Geomorphology and sediment stability of a segment of the U.S. continental slope off New Jersey, Science, v. 211, p. 935-937.

Rona, P.A., 1969, Middle Atlantic continental slope of United States; deposition and erosion, AAPG Bulletin, v. 53, p. 1453-1465.

Rona, P.A., and Clay, C.S., 1967, Stratigraphy and structure along a continuous seismic reflection profile from Cape Hatteras, North Carolina, to the Bermuda Rise, Journal of Geophysical Research, v. 72, p. 2107-2130.

Rona, P.A., Sheridan, R., Robb, J., Trotta, J., and Grassle, F., 2000, Geological processes on the New Jersey upper continental rise: deepwater dumpsite 106, Geological Society of America Abstracts with Programs, v. 32, p. 1-A-70.

Rubey, W.W., and Hubbert, M.K., 1959, Overthrust belt in geosynclinal area of western Wyoming in light of fluid-pressure hypothesis, part 2 of role of fluid pressure in mechanics of overthrust faulting, GSA Bulletin, v. 70, p. 167-205.

Shepard, F.P., 1981, Submarine canyons: multiple causes and long-time persistence, AAPG Bulletin, v. 65, p. 1062-1077.

Strack, O.D.L., 1989, Groundwater Mechanics, Englewood Cliffs, Prentice Hall, 732 p.

Terzaghi, K., 1943, Theoretical Soil Mechanics, London, Chapman and Hall, 510 p.

Chapter 2: Fluid flow and Stability of the US Continental Slope Offshore New Jersey from the Pleistocene to the Present

Abstract

We predict that portions of the New Jersey continental slope were unstable approximately 0.5 million years ago. This instability was caused by rapid sediment loading during a Pleistocene sea-level lowstand and by flow focusing in underlying, permeable Miocene strata. The simulated instability is consistent with soft-sediment deformation and small slumps in Pleistocene strata of the Hudson Apron. Stability of the New Jersey margin has increased since 0.3 Ma because sedimentation rate has decreased. Today, the modeled factor of safety (FS) for the upper slope is approximately 1.5 whereas in the lower slope it exceeds 3. We predict that sedimentation rate is a dominant factor on slope stability. When rapid and asymmetric loading of a highly permeable sedimentary layer occurs, the location of instability can shift seaward to regions where sedimentation rates are low. Stability calculations use pressures and effective stresses predicted by a coupled sedimentation-fluid flow model. This hydrodynamic analysis demonstrates how the interplay of sedimentation and fluid migration affect the distribution, timing, and size of sedimentary failures.

2.1 Introduction

Sedimentation rate and permeability architecture control the pore water hydrodynamics of continental slopes. Rapid deposition of low permeability sediments generates fluid overpressure, which supports a portion of the overburden. This creates low effective stress and affects the stability of the sediments. Where low-permeability sediments are interbedded with laterally continuous sands, spatial variations in sediment loading result in a complex flow field (Dugan and Flemings, 2000; Yardley and Swarbrick, 2000) that significantly alters the stability of the slope. Stability is lowest where overburden stress is low and overpressure is high. The rate of sediment loading and the rate at which fluids migrate in high- and low-permeability strata dictate the timing and location of slope failure.

We present a general model of how pore water hydrodynamics are influenced by a spatially varying sedimentation rate that is characteristic of passive margins. The model is extended by including an isolated aquifer in the margin and exploring the impact of this aquifer on regional fluid flow and stability. This general model is then applied to the stratigraphic geometry of offshore New Jersey where Pleistocene silty clay has rapidly and differentially buried more permeable Miocene sandy silt.

2.2 Fluid Flow and Stability Models

We use a two-dimensional sedimentation-fluid flow model to simulate the hydrodynamic evolution of the continental slope. Fluid pressure is modeled assuming that sedimentation is the only pressure source, solid and fluid mass are conserved, and that fluid flow is

defined by Darcy's law (Equation 2.1) (Dugan and Flemings, 2000; Gordon and Flemings, 1998).

$$\frac{DP}{Dt} = \left[\frac{k(1-\phi)^2}{S_t\mu}\right]\nabla^2 P* + \left[\frac{\phi\beta}{S_t(1-\phi)}\right]\frac{DS_v}{Dt} \tag{2.1}$$

$P = \rho_w gz + P*$, $S_t = \phi\beta/(1-\phi) + \phi\beta_f$, and solid grains are assumed incompressible. All variables are defined in Table 2.1. Porosity is modeled as a function of vertical effective stress, $d\phi/\phi = -\beta d\sigma_v$ following the approaches of Rubey and Hubbert (1959) and Hart *et al*. (1995). Equation 2.1 is presented in material coordinates referenced to the solid grains. All sediments are deposited with the same initial porosity ($\phi_o = 61\%$) and have the same bulk compressibility ($\beta = 0.44$ MPa^{-1}) as constrained from core data (Dugan and Flemings, 2000).

Permeability of silty clay sediments is modeled as a function of porosity, $\log(k_v) = I + B\phi$ (Mello *et al*., 1994). *I* equal to -18.5 and *B* equal to 1.25 are set constant to define vertical permeability (k_v) consistent with measurements from Pleistocene silty clay of the New Jersey continental slope (Blum *et al*., 1996). The vertical permeability of sandy silt aquifer sediments was set constant at 3x10^{-16} m^2. An anisotropy (k_h/k_v) of 10 was used for all sediments.

Table 2.1: Nomenclature

Variable	Definition	Dimensions
B	permeability model constant	dimensionless
c	cohesion of sediment	M/LT^2
FS	factor of safety	dimensionless
g	acceleration due to gravity	L/T^2
i	local segment index for stability calculation	integer
I	permeability model constant	dimensionless
k	permeability	L^2
k_h	horizontal permeability	L^2
k_v	vertical permeability	L^2
M	stability function	dimensionless
n	number of slices in stability calculation	integer
P	fluid pressure	M/LT^2
$P*$	overpressure	M/LT^2
S_t	storage coefficient	LT^2/M
S_v	overburden stress	M/LT^2
t	time	T
W	average force per unit width into plane	M/T^2
x	horizontal length	L
x_{loc}	horizontal position in model	L
y_{loc}	vertical position in model	L
z	depth below sea level	L
β	bulk compressibility	LT^2/M
β_f	fluid compressibility	LT^2/M
ϕ	porosity	dimensionless
ϕ_f	sediment friction angle	dimensionless
ϕ_o	initial porosity	dimensionless
ρ_w	water density	M/L^3
σ_v	vertical effective stress	M/LT^2
θ	local angle of failure plane	dimensionless
μ	dynamic viscosity	M/LT

The horizontal scale for all simulations is 20 km (Figure 2.1). Total vertical thickness varies depending on the sedimentation rate prescribed in the model. Overpressure is assumed to be zero at the sea floor. The basal and landward boundaries are treated as no-flow boundaries (Figure 2.1). The landward boundary represents the shelf-slope break and can be treated as a flow divide because loading and pressure generation decrease landward and seaward of this position; therefore fluids migrate landward and seaward from this location.

The infinite slope approximation is used to calculate the factor of safety (*FS*) for the model domain (Equation 2.2). *FS* > 1 represents stability and *FS* ≤ 1 represents instability. The analysis assumes that the failure surface is parallel to the sea floor, fluid pressure is constant along the failure plane, end effects and stresses can be neglected, and sediments on the slide surface are homogeneous (Lambe and Whitman, 1979; Loseth, 1998).

$$FS = \frac{c + [(S_v - \rho_w gz)\cos^2\theta - P^*]\tan\phi_f}{(S_v - \rho_w gz)\sin\theta\cos\theta} \tag{2.2}$$

All variables are defined in Table 2.1. We assume sediment cohesion (*c*) is equal to zero, a typical value for normally consolidated clays (Lambe and Whitman, 1979; Craig, 1992). The angle of internal friction (ϕ_f) is assumed to be a constant 26°. Internal friction angles range from 20-35° for clays and from 27-30° for silty sand (Craig, 1992). These assumptions provide a minimum estimate of stability because cohesion and higher internal friction angles will increase the calculated stability.
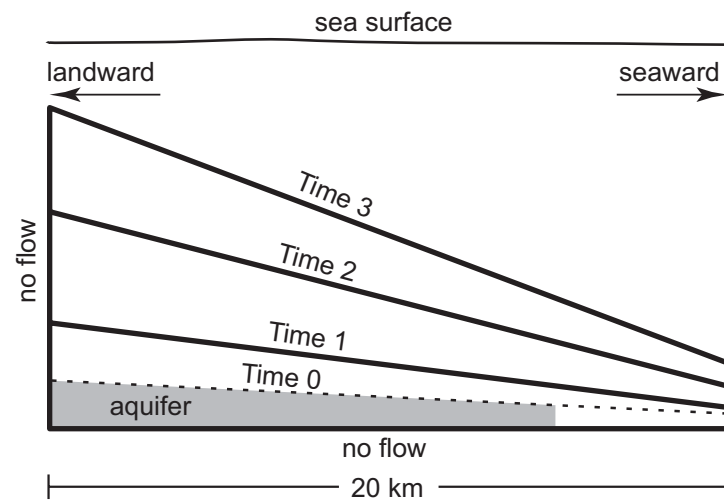
Figure 2.1: Schematic of the model system. Initial model domain (Time 0) was set as hydrostatic. Shaded region defines aquifer included in some simulations. The sea floor position varies in time (e.g., Time 1, Time 2, Time 3) as sediments are deposited.

We apply these models to two depositional architectures common in continental margins: (1) Silty Clay without Aquifer (Figure 2.2A) and (2) Silty Clay with Aquifer (Figure 2.2B). These architectures thin downslope to reflect increased distance from the sediment source. The initial condition for the model is a hydrostatically pressured sedimentary layer that extends the length of the basin (0.2 km thick at landward margin, 0.1 km thick at seaward margin) (Time 0, Figure 2.1). This layer is then loaded for one million years by silty clay (e.g. Time 1-3, Figure 2.1). In Figure 2.2, the sedimentation rate is 1.2 mm/yr at the landward margin and linearly decreases to 0.2 mm/yr at the seaward margin.

2.2.1 Silty Clay without Aquifer Model

Modeled overpressure in the silty clay is sub-parallel to the sea floor (Figure 2.2A). The maximum overpressure (4.5 MPa) is in the landward zone where sedimentation rate is highest and consequently sediments are thickest. Overpressure gradients drive fluids upward and outward toward the sea floor. Maximum flow velocities (0.3 mm/yr) are simulated in the shallow subsurface where porosity and permeability are high. Near the basal boundary, fluid velocity is an order of magnitude lower as a result of low porosity, low permeability, low pressure gradients, and the no-flow boundary (Figure 2.2A).

Because of the pressure field described above, vertical effective stress parallels the sea floor. The effective stress increases slowly downward in the shallow subsurface and rapidly increases deeper in the sedimentary column (Figure 2.2A). A maximum of 8 MPa of effective stress is predicted where sediment accumulation was greatest.
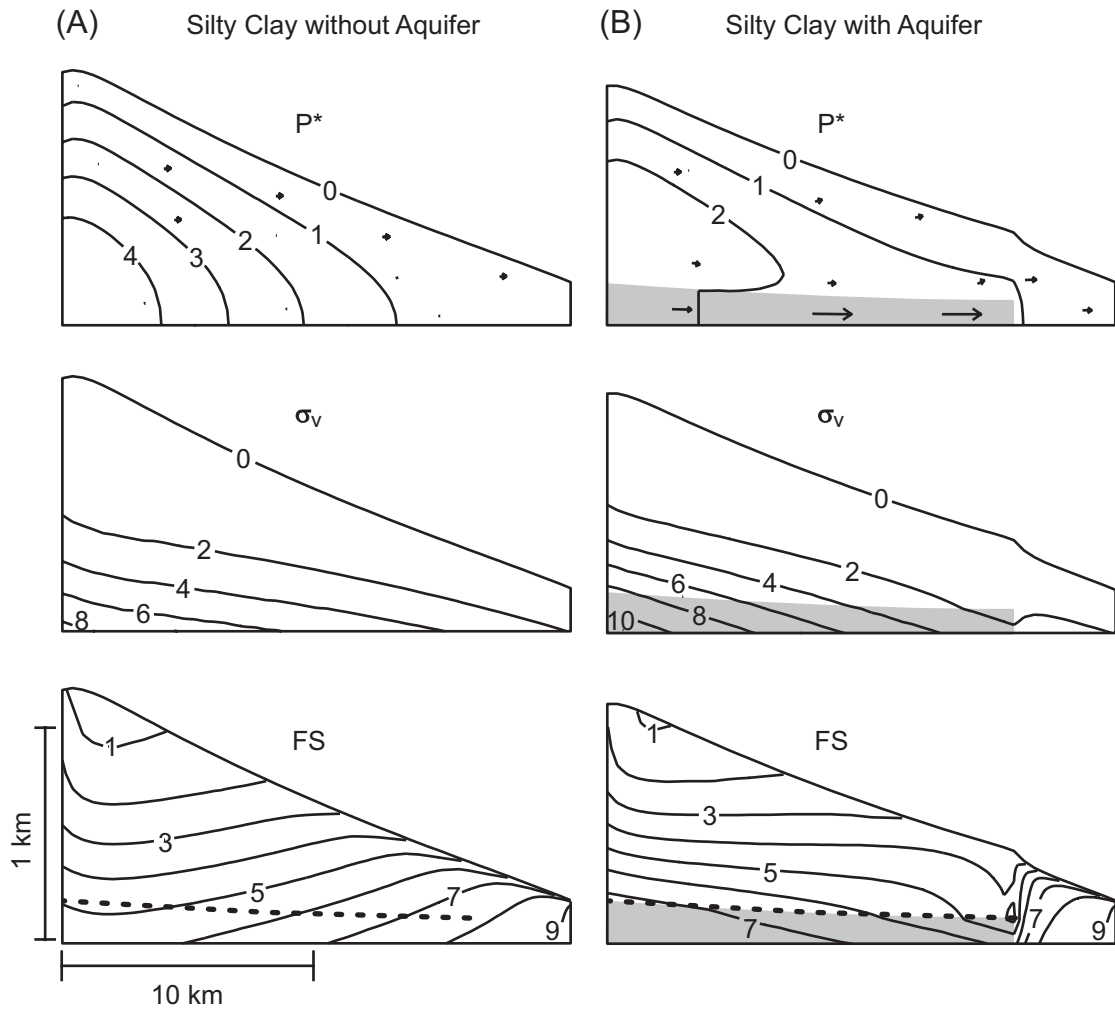
Figure 2.2: Overpressure (P^*), vertical effective stress (σ_v), and infinite slope factor of safety (FS) simulations for (A) Silty Clay without Aquifer model and (B) Silty Clay with Aquifer model. Aquifer is shaded grey. Arrows (P^* diagrams) are flow vectors. Maximum flow velocity is 3 mm/yr in the aquifer. Note vertical exaggeration.

Unstable conditions (factor of safety, $FS \leq 1$) are predicted for a small portion of the landward zone (Figure 2.2A). The FS equals 9 at the seaward margin where overpressure and effective stress are low. At the sea floor, effective stress is zero; however, near the sea floor FS increases seaward as overpressures decreases seaward (Figure 2.2A).

2.2.2 Silty Clay with Aquifer Model

The addition of a permeable aquifer beneath the silty clay decreases overpressure relative to the Silty Clay without Aquifer example (Figure 2.2B versus Figure 2.2A). Lower overpressure results because the aquifer acts as a drain to the silty clay where fluids migrate downward to the aquifer in addition to the vertical drainage toward the sea floor (Figure 2.2B). A maximum overpressure of 2.5 MPa is simulated near the landward margin. Flow within the aquifer reaches a maximum velocity of 3 mm/yr in contrast to the 0.3 mm/yr velocity in the overlying silty clay. Fluid discharge from the seaward end of the aquifer increases overpressure above that predicted for the equivalent location in the Silty Clay without Aquifer model (Figure 2.2).

The Silty Clay with Aquifer simulation has a vertical effective stress profile similar to the Silty Clay without Aquifer simulation (Figure 2.2). The shallow subsurface has low effective stress, and effective stress increases rapidly downward near the aquifer. The maximum effective stress of 10 MPa occurs in the deep, landward sediments where overpressure is moderate and total stress is high (Figure 2.2B).

Enhanced drainage by the permeable aquifer increases slope stability. *FS* increases with depth below sea floor and with distance seaward; a small zone of *FS* < 1 is present along the sea floor of the landward margin, and *FS* > 9 exists at the base of the seaward margin (Figure 2.2B). Flow focusing within the aquifer causes a *FS* drawdown at the seaward termination of the aquifer and a factor of safety increase in the landward region of the aquifer (Figure 2.2B versus Figure 2.2A).

2.2.3 Chronostability Analysis

We use a chronostability diagram (Figure 2.3) to describe the evolution of the stratigraphic surface immediately above the aquifer throughout its burial history (Figure 2.3B); the depth-equivalent surface is analyzed for the Silty Clay without Aquifer simulation (Figure 2.3A). Without an aquifer (Figure 2.3A), the surface is very stable (*FS* > 8) in its early history (1.0 – 0.9 Ma). This high stability exists because loading begins on a hydrostatically pressured zone and because surface slopes are low. As this surface is further buried, it becomes less stable until approximately 0.4 Ma. The stability of the surface has been near steady state since 0.4 Ma with *FS* < 5 in the landward zone and *FS* > 7 in the seaward zone (Figure 2.3A).
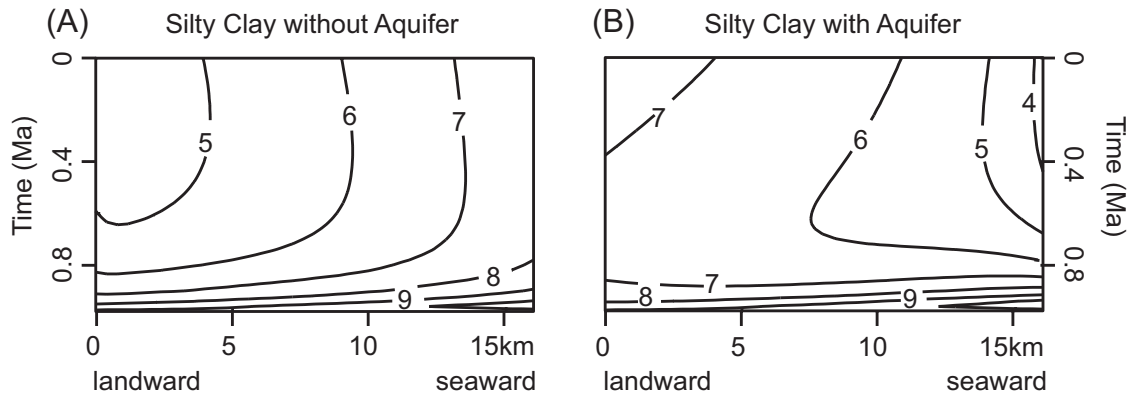
Figure 2.3: Chronostability diagrams for the Silty Clay without Aquifer simulation (A) and Silty Clay with Aquifer simulation (B). *FS* **contours are presented for the aquifer-silty clay boundary and the depth-equivalent surface for the Silty Clay without Aquifer model. Surfaces used in chronostability diagrams are located in Figure 2.2** *FS* **plots.**

The Silty Clay with Aquifer model (Figure 2.3B) has similar early behavior (1.0 - 0.9 Ma), but thereafter exhibits a strikingly different behavior. After 0.9 Ma, the stability of the aquifer surface decrease, but is still stable, in the seaward direction. This is the opposite of the trend observed in the Silty Clay without Aquifer model (Figures 2.3A, 2.3B). Along the landward margin, *FS* gradually decreases until 0.5 Ma, and then *FS* increases. The seaward margin has a factor of safety decrease to a minimum of 4 that persists from 0.4 Ma to present (Figure 2.3B).

2.2.4 Parameter Analysis

Table 2.2 describes some critical results on slope stability. For example, the minimum factor of safety for the Silty Clay with Aquifer example was 0.8 at 8% of total seaward extent and 9% of total depth (Figure 2.2B; Table 2.2). With a highly permeable aquifer that is buried rapidly, the instability originates in the landward zone (6% of total seaward extent, 15% of total depth; Fast Load High *k*, Table 2.2). As loading continues, flow focusing influences instability and the *FS* minimum migrates seaward (74% of total seaward extent; Fast Load High *k*, Table 2.2). This is important because it documents that downslope-decreasing sedimentation upon a permeable aquifer will tend to create instability downslope where sedimentation rates are low. For constant sedimentation rate simulations (Rows 1-6, Table 2.2), the minimum *FS* occurs chronologically at the end of the simulation, but its spatial location depends on the permeability architecture.

2.3 The New Jersey Continental Slope

2.3.1 Overview

We apply our model to the US East coast margin where low permeability Plio-Pleistocene sediments have rapidly loaded underlying, higher permeability Miocene strata (Figures 2.4, 2.5). Along the Hudson Apron, silt- and clay-sized Plio-Pleistocene sediments from the ancestral Hudson River buried Miocene strata. These sediments have formed a smooth continental slope of approximately 3° (Figure 2.4) (McAdoo et al., 2000).

In contrast, Miocene and older strata are exposed on rugose portions of the slope to the southwest where numerous canyons and failures exist (Figure 2.4) (Hampson and Robb, 1984). This canyon-incised region contains highly variable slopes ranging from 2° to 21° with a mean of 8° (McAdoo *et al*., 2000). Slope failure and erosion have been attributed to paleo-river systems, slope over-steepening, seismically-induced failure, excess water pressures driving failure, erosion from debris flows, and gas migration driving failure (Spencer, 1903; Johnson, 1939; Rona, 1969; Shepard, 1981; Twichell and Roberts, 1982; Farre *et al*., 1983; Pratson *et al*., 1994; Driscoll *et al*., 2000). A secondary debate is whether these canyons eroded upslope or downslope (e.g.; Twichell and Roberts, 1982; Farre *et al*., 1983; Pratson *et al*., 1994).

Table 2.2: Infinite Slope *FS* Parameter Analysis. Max.Sed. is the sedimentation rate at the landward margin of the simulation. NJ models had peak sedimentation rate of 3.0 mm/yr from 0.5-0.36 Ma (Figure 2.6). **Sed.Ratio** is the ratio of the landward sedimentation rate to the seaward sedimentation rate. k_{aq}/k_{mud} defines 'aquifer' permeability relative to the permeability of the silty clay being deposited. FS_{min} is the minimum *FS* simulated; FS_{min} is located spatially as a percent of total seaward extent (x_{min}) and as a percent of total depth at that location (y_{min}). 1st*FS*<1 defines the time at which instability was first simulated. The location of initial instability is defined by x_{1st} and y_{1st}, which are presented in percent of total seaward extent and percent of total thickness.

Model	Max. Sed. (mm/yr)	Sed. Ratio	k_{aq}/k_{mud}	FS_{min}	x_{min} (%)	y_{min} (%)	1st FS<1 (Ma)	x_{1st}	y_{1st}	Figure
Silty Clay w/o Aquifer	1.2	6	1	0.8	8	9	0.16	6	10	2.2A, 2.3
Silty Clay w/ Aquifer	1.2	6	300	1.0	6	8	0.00	6	8	2.2B, 2.3
Fast Load Aquifer	2.0	10	300	0.1	12	10	0.56	6	20	-
High k Aquifer	1.2	6	1000	1.3	6	10	-	-	-	-
Fast Load High k	1.5	7	1000	0.3	74	80	0.40	6	15	-
1D	0.4	1	300	4.7	-	7	-	-	-	-
NJ Slope	3.0*	6	300	0.4	8	8	0.40	6	20	2.7, 2.8, 2.9
NJ Silty Clay	3.0*	6	1	0.3	10	7	0.46	6	15	-
NJ High k Aquifer	3.0*	6	1000	0.4	80	75	0.40	6	22	-
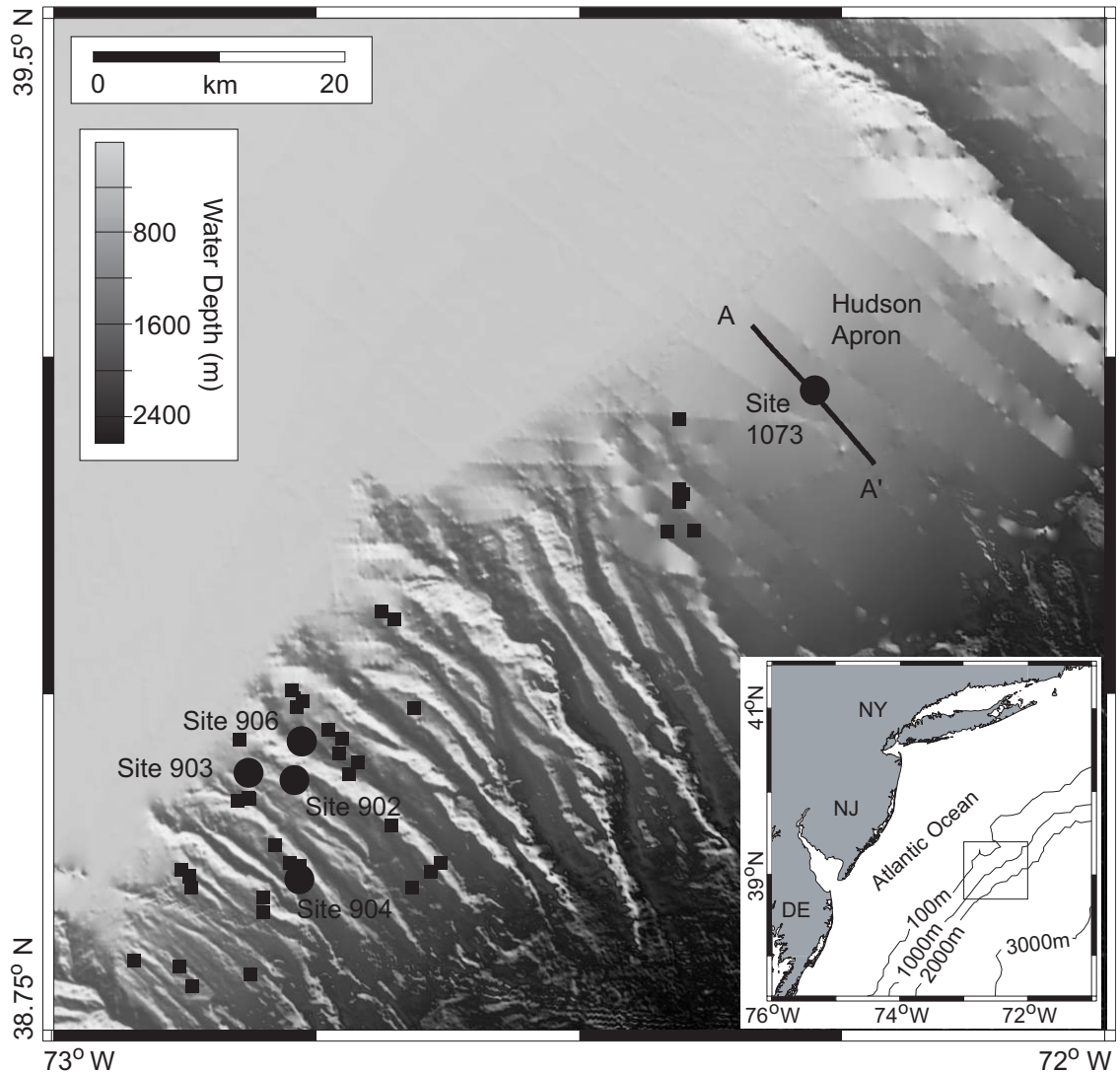
Figure 2.4: Basemap of the study region offshore from New Jersey showing rugose and smooth bathymetry of the slope. Circles are ODP Sites. Squares are locations of USGS geotechnical sites that sampled the upper 10 m of sediment column (Olsen and Rice, 1982; Booth *et al*., 1985). Seismic line A-A' is presented in Figure 2.5.
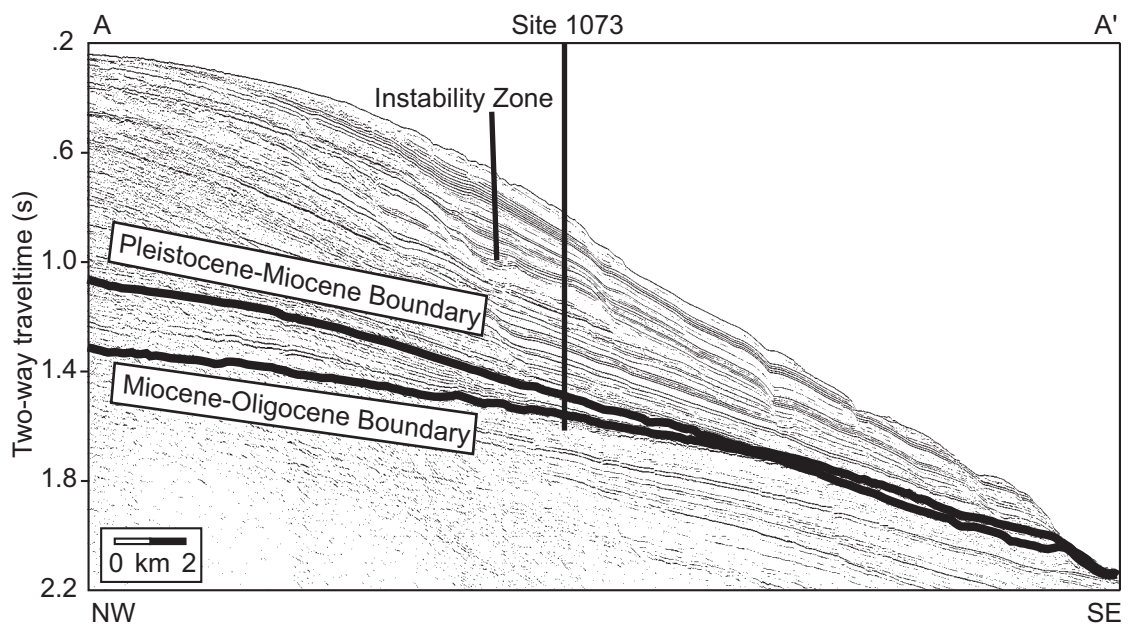
Figure 2.5: Seismic cross-section A-A' (located in Figure 2.4) (Mountain and Monteverde, 2000) used to characterize the geometry of the Miocene to Pleistocene strata of offshore New Jersey. Zones of previous sediment instability are interpreted based on slump features present in Pleistocene strata near Site 1073. Data are presented in two-way traveltime.

Geotechnical analyses of the upper 10 metres below the sea floor (mbsf) were interpreted

to reflect stable conditions for the modern US East coast continental slope (Figure 2.4)

(Olsen and Rice, 1982; Booth *et al*., 1984; Booth *et al*., 1985). These studies assumed

pressure is hydrostatic. Booth *et al.* (1984; 1985), however, estimated that overpressure

reaching 60-90% of hydrostatic effective stress ($S_v - \rho_w gz$) or ground accelerations >10%

of gravity would destabilize the slope. Dugan and Flemings (2000) predicted pressure that

reaches 90% of hydrostatic effective stress in the deeper sediments (100 – 650 mbsf) of

ODP Site 1073 of offshore New Jersey. This suggests the possibility for slope failure at

depth may be greater than previously predicted for the shallow subsurface.

2.3.2 Stratigraphic Architecture

The dominant lithology at Site 1073 is silty clay (Figure 2.6) (Shipboard Scientific Party,

1998; Hoyanagi and Omura, 2001). To 220 mbsf, numerous silt layers interrupt the silty

clay section. From 220-520 mbsf, the section is lithologically homogeneous with the only

lithologic variation being a clay layer (290-300 mbsf). Pliocene and Miocene strata have

higher silt and sandy silt content, relative to the overlying Pleistocene sediments (Figure

2.6). Sandy silt zones coincide with glauconite contents that reach 15-20% (Shipboard

Scientific Party, 1998). The glauconite is part of a regional glauconite layer formed *in situ*

in deep water (600-1000 m) during a sea level rise and highstand (Hesselbo and Huggett,

2001). The sandy glauconitic zone is partially cemented and as a result they retain high

porosity (> 60%) and have high shear strength (Figure 2.6). Measured permeability of the

Pleistocene silty clay is of order 10^{-18} m^2 (Blum *et al*., 1996), whereas permeability of the

high porosity Miocene strata is an order of magnitude greater (Olgaard *et al*., 2001).
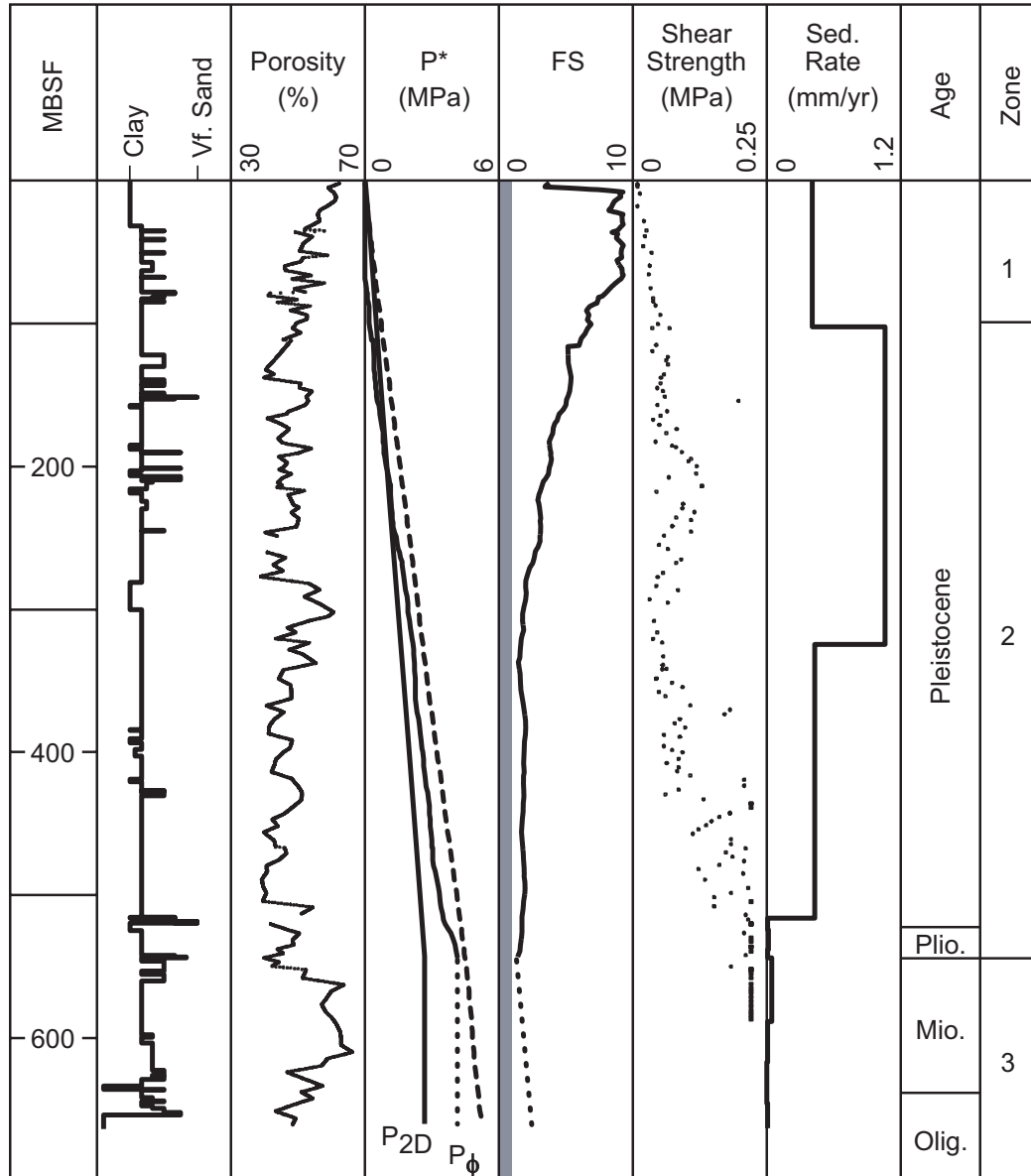
Figure 2.6: Well profile for ODP Site 1073 (located in Figure 2.4) based on observations and interpretations from core (Shipboard Scientific Party, 1998). P_ϕ **is a moving average of the overpressure interpreted from porosity and is plotted in comparison to the hydrostatic effective stress (dashed line) (Dugan and Flemings, 2000).** P_{2D} **is the overpressure predicted from the fluid flow model (NJ Slope of Table 2.2; Figure 2.7) at Site 1073.** *FS* **from infinite slope analysis based on the porosity-predicted pressures.** *FS* < 1 **(shaded region) represents unstable conditions. Shear strength measurements were made with the automated vane shear and the penetrometer. Shear strength of Miocene strata is at least 0.22 MPa, the measurement limit of the penetrometer.**

2.3.3 Pressure from Porosity

Porosity at Site 1073 is separated into three zones (Figure 2.6). Porosity decreases from 62% at the sea floor to 45% at 100 mbsf (Zone 1). Zone 2 is a 450 m thick section charac-terized by porosity between 45% and 50%. An increase in porosity to 60% marks the top of Zone 3 near the Pliocene-Miocene boundary. Within Zone 3, porosity is constant at 60% for 60 metres and the underlying sediments show a gradual porosity decrease to 50%.

An exponential porosity-stress relation (Rubey and Hubbert, 1959; Hart *et al*., 1995; Dugan and Flemings, 2000) was use to estimate overpressure from measured porosity at ODP Site 1073 (Figure 2.6). The model was constrained in Zone 1 assuming hydrostatic fluid pressure ($P^* = 0.0$ MPa). Predicted pressure in Zone 2 reaches 95% of the lithostatic stress. Overpressure in Zone 3 is assumed to be in equilibrium with the overlying Plio-Pleistocene strata and to have a hydrostatic gradient ($P^* = $ constant $= 3.7$ MPa). Overpres-sure is not predicted from porosity in the Miocene section because the porosity of cemented sediments does not reflect the state of stress. A hydrostatic pressure gradient is inferred in the Miocene and Oligocene sediments because high porosity and high perme-ability facilitate pressure equilibration.

2.3.4 Stability Analysis

An infinite-slope analysis (Equation 2.2) at Site 1073 predicts stable conditions (Figure 2.6). We used a failure plane equal to 3°, assumed zero cohesion, and prescribed a 26°

angle of internal friction. From the sea floor to 20 mbsf, the factor of safety (*FS*) rapidly

increases from 3 to 10. The stability of this section is highly sensitive to subtle variations

in bulk density. Constant *FS* equal to 10 exists from 20-100 mbsf and corresponds to

hydrostatic fluid pressures and normal compaction. Below 100 mbsf, *FS* gradually

declines to nearly 1 at the top of the Miocene sediments. This decline begins at the onset

of overpressure and *FS* continues to decline with depth as effective stress decreases (Fig-

ure 2.6). Below the Miocene boundary, *FS* increases as effective stress increases.

Although the infinite slope analysis predicts near failure conditions at depth, the stability

is likely to be higher because these deeper sediments have higher shear strength than the

shallow sediments (Figure 2.6). This shear strength increase is not considered in the

model. Local strength increases correlate with increases in sand content. A small-scale

slump observed at Site 1073 near 440 mbsf (Shipboard Scientific Party, 1998) corresponds

to a local strength decrease.

2.3.5 New Jersey Slope Model

We apply the general Silty Clay with Aquifer model to the New Jersey continental slope

where Miocene sandy silt has been asymmetrically loaded by lower permeability Plio-

Pleistocene silty clay. The horizontal scale of the model is 20 km, identical to that of the

previous examples (Figures 2.2, 2.3). The vertical scale is changed slightly as the sedi-

mentation rate is varied for the New Jersey slope model. We constrain the rock properties

based on observations at Site 1073 and we constrain the permeability architecture from

seismic data (Figure 2.5). The permeability model is composed of a thin, permeable,

Miocene aquifer (k_v = 3x10^{-16} m^2) that has been isolated by low-permeability Plio-Pleis-

tocene silty clay [log(k_v) = -18.5 + 1.25ϕ]. The Miocene sediments are assumed to be

hydrostatically pressured; they are buried for one million years by Plio-Pleistocene silty

clay. The final model geometry (Figure 2.7) results from sedimentation rate that linearly

varies upslope and downslope from Site 1073. Sedimentation rates vary temporally as

interpreted at Site 1073 (Figure 2.6).

Overpressure: At the end of the simulation, overpressure varies as a function of sea floor

topography and proximity to the permeable Miocene aquifer (Figure 2.7A). In the shallow

Plio-Pleistocene section (<300 mbsf), overpressure parallels the sea floor. The highest

overpressure (4.6 MPa) is in the landward zone, where sediment accumulation was great-

est. The maximum aquifer overpressure is 3.0 MPa (landward region) while minimum

overpressure is 2.0 MPa at the seaward termination of the aquifer (Figure 2.7A). High

pressures at the seaward extent of the aquifer contribute to elevated overpressure in the

overlying Plio-Pleistocene sediments. Simulated overpressure matches the porosity-pre-

dicted pressures interpreted at Site 1073 (Figure 2.6) (Dugan and Flemings, 2000).
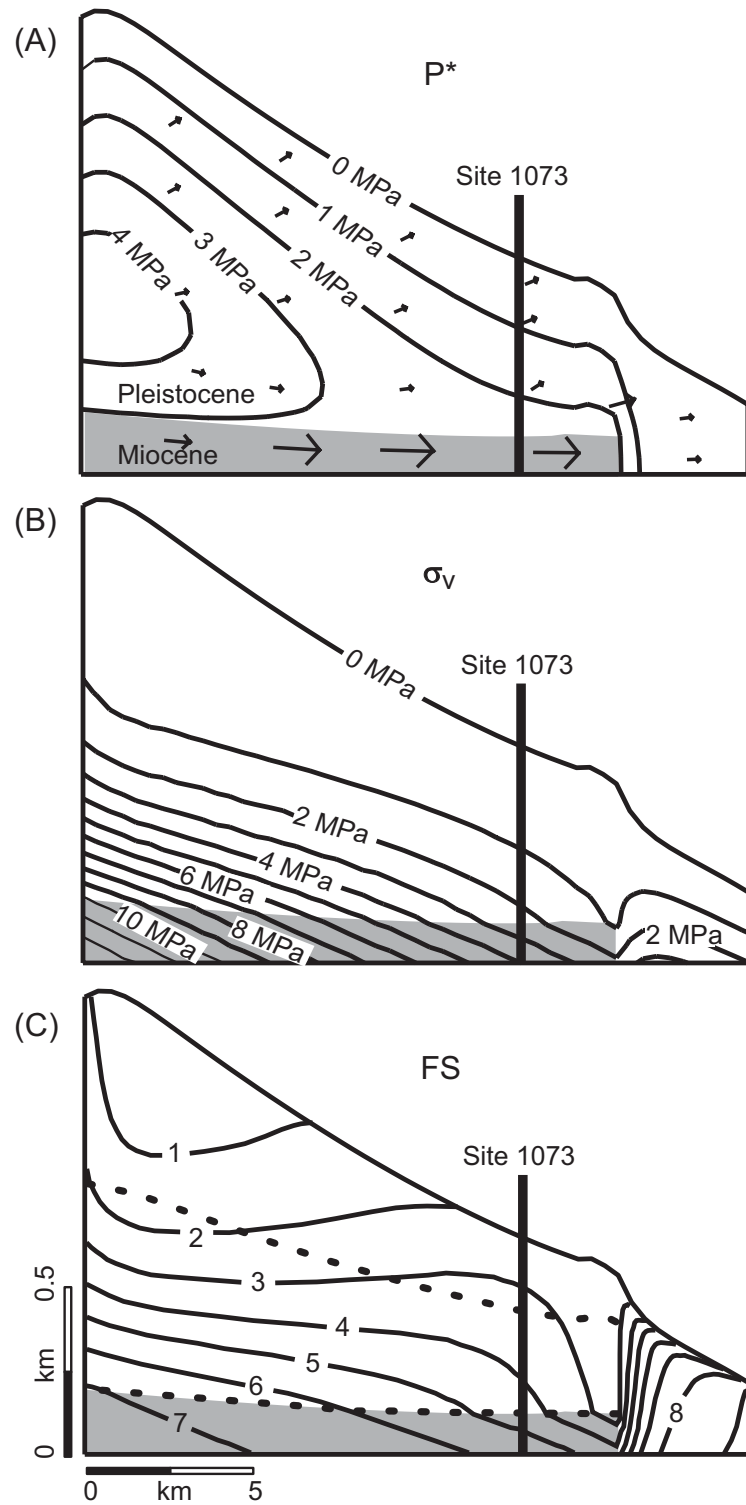
Figure 2.7: Simulated (A) overpressure, (B) effective stress, and (C) infinite slope *FS* for the modern New Jersey slope. Dashed surfaces in (C) are presented in chronostability diagram (Figure 2.8). Note vertical exaggeration.

Fluid Flow: In the shallow subsurface (< 300 mbsf), fluids migrate slowly (< 1 mm/yr) upward and seaward to the sea floor (Figure 2.7A). High overpressures in Plio-Pleistocene silty clay and lower overpressures in the Miocene aquifer create a second flow regime where fluids migrate downward to the Miocene aquifer. In the aquifer, fluid migration is rapid (up to 7 mm/yr). The permeability of the aquifer yields high fluid velocity even though pressure gradients are small. Ultimately, fluids are discharged vertically from the seaward termination of the aquifer into the overlying silty clay (Figure 2.7A).

Effective Stress: Vertical effective stress is less than 1 MPa in the upper 500 mbsf (Figure 2.7B). Below 500 mbsf, effective stress increases rapidly to a maximum of 12 MPa for the modern slope (Figure 2.7B). The highest effective stress exists in the Miocene section where the overburden is thick and pore pressure is relatively low. Effective stress is low where fluids are discharged vertically upward from the aquifer and overpressure is high (Figure 2.7).

Infinite Slope FS: Today, the only instability predicted is in the landward region of off-shore New Jersey, where shallow sediments are predicted to be unstable (Figure 2.7C). If measured cohesion values (0.0015-0.0045 MPa) from the US East coast slope (Booth *et al*., 1984) are included in the *FS* calculation, stable conditions are predicted. With increased depth below the sea floor, *FS* increases and reaches 7 at the Miocene aquifer. Directly above the Miocene aquifer, FS decreases seaward reaching a minimum of 2.8 (Figure 2.7C). Seaward of the aquifer, *FS* increases as overpressure decreases.

Chronostability: We examine the stability evolution for two surfaces: one immediately above the aquifer, and the 0.4 Ma surface (dashed lines, Figure 2.7C). For the surface above the aquifer, the stability from 1.0 to 0.5 Ma is similar to that described in Figure 2.3B (Silty Clay with Aquifer model). A significant difference occurs when sedimentation rate increases (0.5 Ma; Figure 2.8C) and there is a sharp decrease in stability along the aquifer surface (Figure 2.8A). The 0.4 Ma surface, which was deposited during this increased sedimentation, has two minima: one in the landward zone driven by sediment loading and one in the seaward zone driven by flow focusing (Figure 2.8B). This example provides insight into how stability of continental margins evolves. In the case of the New Jersey slope from Pleistocene to present, and perhaps many other margins, stability was at a minimum during rapid sedimentation and thereafter stability has increased.

Parameter Analysis: In the New Jersey slope simulation (Figure 2.7), unstable conditions originate in the landward zone during the pulse of increased sedimentation (NJ Slope, Table 2.2). The minimum *FS* equal to 0.4 for the NJ Slope simulation occurs in the shallow sediments of the landward region (8% of seaward extent, 8% of total depth) at the end of this sedimentation pulse. Without a permeable aquifer, the minimum *FS* decreases to 0.3, but still occurs in the landward zone during the period of most rapid sedimentation (NJ Silty Clay, Table 2.2). When the aquifer permeability is increased, the instability originates during the time period of most rapid loading, but moves seaward to the termination of the aquifer (NJ High *k* Aquifer, Table 2.2). This emphasizes the combined role of sediment loading and flow focusing in determining the timing and location of sedimentary failure.
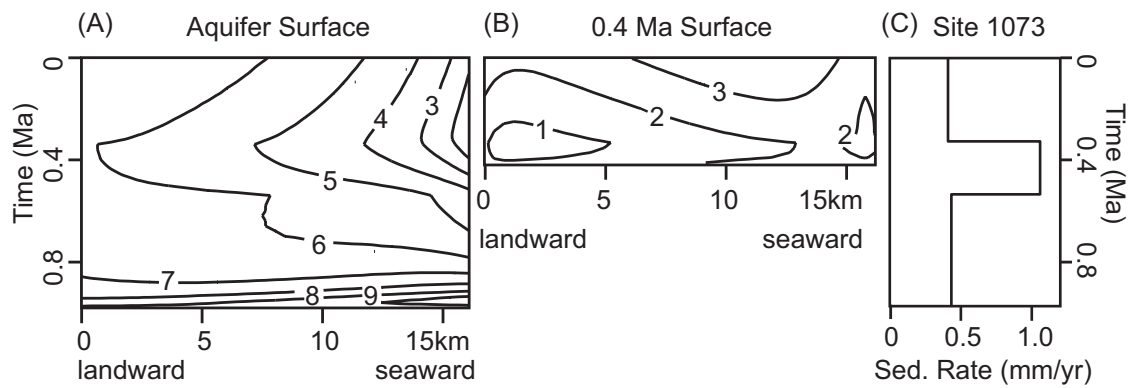
Figure 2.8: Chronostability diagram shows infinite slope *FS* evolution for aquifer surface (A) and 0.4 Ma surface (B) (located in Figure 2.7C) during burial. Sedimentation rate (C) at Site 1073 (13.5 km from landward margin) defines temporal loading history. Sharp increase in sedimentation rate (C) coincides with rapid decrease in stability of aquifer surface (A) and with minimum stability of the 0.4 Ma surface (B).

Bishop 2D FS: For comparison to the infinite slope analysis (Figure 2.6), we evaluate *FS*

in two dimensions using the Bishop method of slices (Equation 2.3) (Bishop, 1955;

Lambe and Whitman, 1979). The analysis involves defining a circular failure surface,

dividing that surface into discrete segments, and comparing the downslope gravitational

forces to the frictional resistance to failure along each segment (Equation 2.3).

$$FS = \frac{\sum_{i=1}^{i=n} [c\Delta x_i + (W_i - P_i \Delta x_i)\tan\phi_f]\left[\frac{1}{M_i(\theta)}\right]}{\sum_{i=1}^{i=n} W_i \sin\theta_i} \tag{2.3}$$

where $M_i(\theta) = \cos\theta_i (1 + \tan\theta_i \tan\phi_f / FS)$. All variables are defined in the nomenclature

table (Table 2.1). The gravitational driving force for each slice depends on the weight of

the sediments (*W*) and the local failure plane. The frictional resistance to sliding is a func-

tion of the effective stress normal to the failure surface, the coefficient of internal friction,

and the cohesion of the sediment. Shear and horizontal stresses within the failure are

neglected without loss of accuracy (Bishop, 1955).

We considered all circular arcs that existed completely within the model domain; all

potential failure surfaces intersect the sea floor at two locations and do not penetrate the

no-flow boundaries. Consistent with our initial the infinite slope analysis, zero cohesion is

assumed and a constant angle of internal friction (26°) is applied.

48
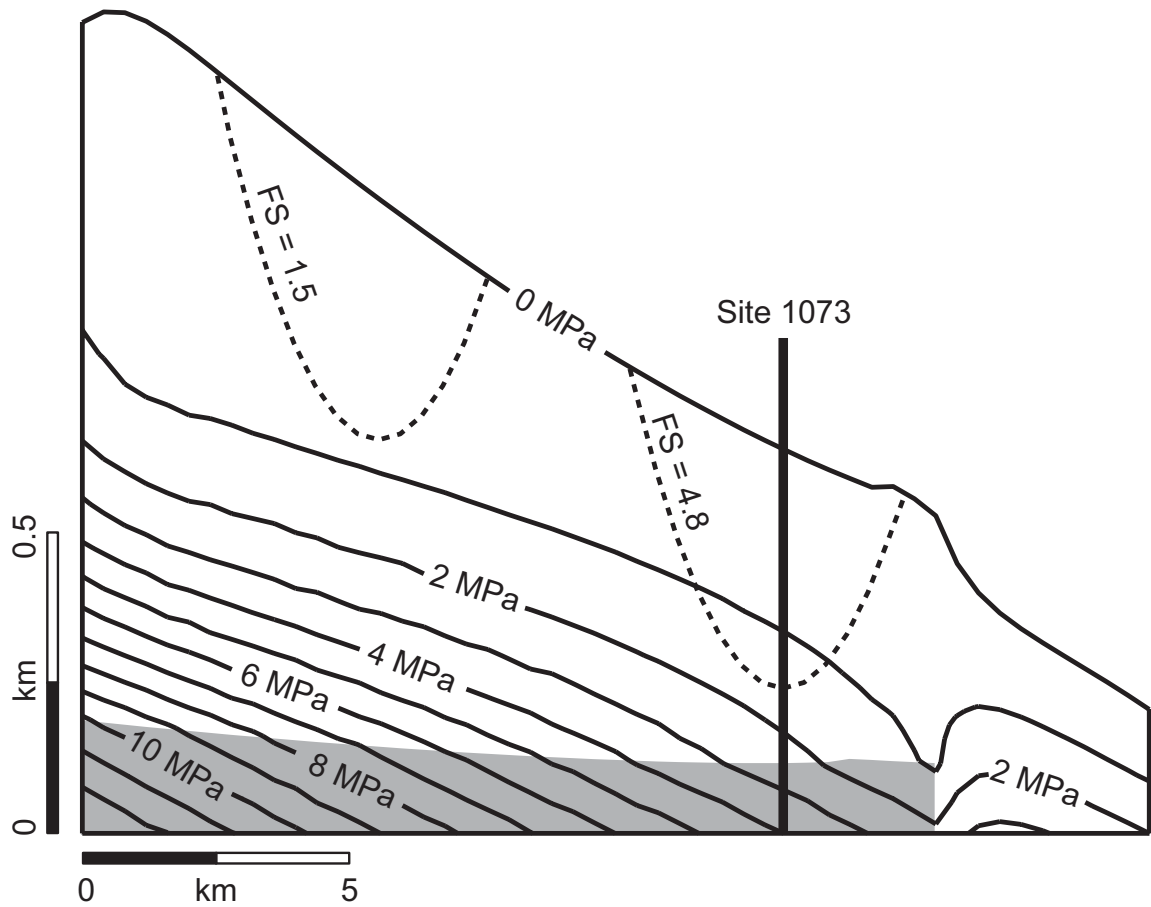
Figure 2.9: Two representative Bishop stability analyses (dashed surfaces) for the New Jersey continental slope margin overlain on simulated vertical effective stress. The analyzed surfaces have the same geometry but different FS because of downslope changes in vertical effective stress. Note vertical exaggeration.

A small portion of the shallow subsurface (<100 mbsf) is predicted to have *FS* < 1. These shallow failures are characterized by nearly zero vertical effective stress. Similar to the infinite slope analysis, a small cohesion value produces stable conditions. Potential failure arcs that extend deeper in the basin are predicted to have *FS* > 1 and *FS* increases seaward (FS > 4; Figure 2.9). The Bishop analysis also predicts the lowest stability during periods of most rapid sedimentation and that the stability of the New Jersey continental slope has increased since 0.3 Ma.

2.4 Discussion

Our general model for spatially varying sedimentation on a permeable aquifer it meant to be representative of the permeability architectures and depositional patterns characteristic of continental margins around the world. The two-dimensional flow field of these margins is markedly different than that predicted by one-dimensional models (e.g. Gibson, 1958). The stress and pressure associated with the flow field contribute to the stability and geo-morphology of the slope. Specifically, given rapid sedimentation and a highly permeable aquifer, flow focussing drives fluids slopeward until they are discharged where overburden is thin;. this flow focussing lowers effective stress at the toe of the slope and causes a sea-ward migration of locations where slope instability may occur. With this model of a rap-idly loaded aquifer and realistic rock properties, we can generate low FS deep in sedimentary sections, which could produce large sedimentary failure scars (e.g. McAdoo *et al*., 2000) that cannot be explained by one-dimensional models or predicted from shal-low geotechnical analyses. The model also explains a mechanism for overpressure genera-tion that drives failures on the middle and lower slope. These failures can initiate

headward erosion and canyon formation (e.g. Twichell and Roberts, 1982; Farre *et al.*, 1983).

The stability evolution simulated for the Hudson Apron is consistent with the slope geomorphology. We predict failure occurred in the Pleistocene silty clay that was deposited most rapidly, and failures have been identified in these strata (Figure 2.5). Deformation and failure features have also been identified in core samples of this rapidly deposited Pleistocene interval (Shipboard Scientific Party, 1998). The current slope is smooth and stable and our model predicts that stable conditions have been present since 0.3 Ma and that stability is currently increasing.

Cohesion is predicted as a critical factor in stabilizing the sediments near the sea floor and in increasing the overall stability of the margin. The importance of cohesion for stable strata is greatest in zones where effective stress is near zero. Cohesion also impacts the form of the mobilized failure; Iverson (1997) described how cohesion can prevent failures from evolving into large mass-mobilizing events or debris flows (Iverson, 1997).

2.5 Conclusions

We simulate an overpressured but stable New Jersey continental slope margin. Active fluid discharge along the slope (Rona *et al.*, 2000) and small failures in Pleistocene strata support our model that stability was at a minimum during pulses of rapid loading and that overpressure is being dissipated and fluids are being discharged in the modern system. The general result of the flow and stability models is that effective stress, overpressure, and

slope stability are controlled by two competing mechanisms: (1) local sedimentation rate and (2) flow focusing. Sedimentation generates high overpressure and low stability where accumulation rates are high. Flow focusing in permeable strata increases overpressure and decreases stability where sedimentation rates are low. The interplay of sediment loading, flow focusing, and slope stability is applicable to many geologic settings where high permeability conduits are differentially buried by low permeability sediments. One example of this is delta systems (e.g. Gulf of Mexico, Amazon Fan) where rapid sediment supply and fluid flow can drive delta-front and slope failures that supply sediments to deeper ocean basins. In convergent margins, similar processes can occur as underthrust strata are loaded by the thick accretionary complexes; failures are expressed in mud volcanism, hydrofracturing, and faulting.

Acknowledgments

References

Bishop, A.W., 1955, The use of the slip circle in the stability analysis of earth slopes, Geo-
technique, v. 5, p. 7-17.

Blum, P., Xu, J., and Donthireddy, S., 1996, Geotechnical properties of Pleistocene sedi-
ments from the New Jersey upper continental slope, *in* Mountain, G.S., Miller, K.G.,
Poag, C.W., and Twichell, D.C. (eds.), Proceedings of the Ocean Drilling Program,
Scientific Results, Volume 150, College Station, Ocean Drilling Program, p. 377-384.

Booth, J.S., Circe, R.C., and Dahl, A.G., 1985, Geotechnical characterization and mass-
movement potential of the United States Mid-Atlantic continental slope and rise,
USGS, 124 p.

Booth, J.S., Silva, A.J., and Jordan, S.A., 1984, Slope-stability analysis and creep suscep-
tibility of Quaternary sediments on the northeastern United States continental slope, *in*
Denness, B. (ed.), Seabed Mechanics, London, Graham & Trotman, p. 65-75.

Craig, R.F., 1992, Soil Mechanics, London, Chapman & Hall, 427 p.

Driscoll, N.W., Weissel, J.K., and Goff, J.A., 2000, Potential for large-scale submarine
slope failure and tsunami generation along the US Mid-Atlantic coast, Geology, v. 28,
p. 407-410.

Dugan, B., and Flemings, P.B., 2000, Overpressure and Fluid Flow in the New Jersey
Continental Slope: Implications for Slope Failure and Cold Seeps, Science, v. 289, p.
288-291.

Farre, J.A., McGregor, B.A., Ryan, W.B., and Robb, J.M., 1983, Breaching the shelfbreak: passage from youthful to mature phase in submarine canyon evolution, *in* Stanley, D.J., and Moore, G.T. (eds.), The Shelfbreak: Critical Interface on Continental Margins, Volume 33, Tulsa, Society of Economic Paleontologists and Mineralogists, p. 25-39.

Gibson, R.E., 1958, The progress of consolidation in a clay layer increasing in thickness with time, Geotechnique, v. 8, p. 171-182.

Gordon, D.S., and Flemings, P.B., 1998, Generation of overpressure and compaction-driven fluid flow in a Plio-Pleistocene growth-faulted basin, Eugene Island 330, offshore Louisiana, Basin Research, v. 10, p. 177-196.

Hampson, J.C., and Robb, J.M., 1984, A Geologic Map of the Continental Slope off New Jersey, Lindenkohl to Toms Canyons, Boulder, USGS.

Hart, B.S., Flemings, P.B., and Deshpande, A., 1995, Porosity and pressure; role of compaction disequilibrium in the development of geopressures in a Gulf Coast Pleistocene basin, Geology, v. 23, p. 45-48.

Hesselbo, S.P., and Huggett, J.M., 2001, Glaucony in ocean-margin sequence stratigraphy (Oligocene-Pliocene, offshore New Jersey, USA; ODP Leg 174A), Journal of Sedimentary Research, v. 71, p. 599-607.

Hoyanagi, K., and Omura, A., 2001, Data report: grain-size analysis of Pleistocene cores from ODP sites 1071, 1072, and 1073, New Jersey margin, *in* Christie-Blick, N., Austin Jr., J.A., and Malone, M.J. (eds.), Proceedings of the Ocean Drilling Program, Scientific Results, Volume 174A, College Station, Ocean Drilling Program, p. 1-18.

Iverson, R.M., 1997, The physics of debris flows, Reviews of Geophysics, v. 35, p. 245-295.

Johnson, D.W., 1939, The Origin of Submarine Canyons: A Critical Review of Hypotheses, New York, Hafner, 126 p.

Lambe, T.W., and Whitman, R.V., 1979, Soil Mechanics: SI Version, New York, John Wiley & Sons, 553 p.

Loseth, T.M., 1998, Submarine Massflow Sedimentation: Computer Modeling and Basin-Fill Stratigraphy, New York, Springer-Verlag, 156 p.

McAdoo, B.G., Pratson, L.F., and Orange, D.L., 2000, Submarine landslide geomorphology, US continental slope, Marine Geology, v. 169, p. 103-136.

Mello, U.T., Karner, G., and Anderson, R.N., 1994, A physical explanation for the positioning of the depth to the top of overpressure in shale-dominated sequences in the Gulf Coast basin, United States, Journal of Geophysical Research, v. 99, p. 2775-2789.

Mountain, G.S., and Monteverde, D.H., 2000, Pleistocene deposition across the New Jersey shelf-slope break, Eos Transactions of the AGU Fall Meeting Supplement, v. 81, p. F654.

Olgaard, D.L., Dugan, B.E., and Gooch, M.J., 2001, Near-sea floor compaction and shallow overpressures: constraints from high strain consolidation tests on ODP sediments, Eos Transactions of the AGU Fall Meeting Supplement, v. 82, p. F1128.

Olsen, H.W., and Rice, T.L., 1982, Geotechnical profiles for thirty-one sites on the Mid-Atlantic upper continental slope, USGS, 148 p.

Pratson, L.F., Ryan, W.B., Mountain, G.S., and Twichell, D.C., 1994, Submarine canyon initiation by downslope-eroding sediment flows; evidence in late Cenozoic strata on the New Jersey continental slope, GSA Bulletin, v. 106, p. 395-412.

Rona, P.A., 1969, Middle Atlantic continental slope of United States; deposition and erosion, AAPG Bulletin, v. 53, p. 1453-1465.

Rona, P.A., Sheridan, R., Robb, J., Trotta, J., and Grassle, F., 2000, Geological processes on the New Jersey upper continental rise: deepwater dumpsite 106, Geological Society of America Abstracts with Programs, v. 32, p. 1-A-70.

Rubey, W.W., and Hubbert, M.K., 1959, Overthrust belt in geosynclinal area of western Wyoming in light of fluid-pressure hypothesis, part 2 of Role of fluid pressure in mechanics of overthrust faulting, GSA Bulletin, v. 70, p. 167-205.

Shepard, F.P., 1981, Submarine canyons: multiple causes and long-time persistence, AAPG Bulletin, v. 65, p. 1062-1077.

Shipboard Scientific Party, 1998, Site 1073, *in* Austin Jr., J.A., Christie-Blick, N., Malone, M.J., *et al*. (eds.), Proceedings of the Ocean Drilling Program, Initial Reports, Volume 174A, College Station, Ocean Drilling Program, p. 153-191.

Spencer, J.W., 1903, Submarine valleys off the American coasts and in the North Atlantic, GSA Bulletin, v. 14, p. 207-226.

Twichell, D.C., and Roberts, D.G., 1982, Morphology, distribution, and development of submarine canyons on the United States Atlantic continental slope between Hudson and Baltimore Canyons, Geology, v. 10. p. 408-412

Yardley, G.S., and Swarbrick, R.E., 2000, Lateral transfer; a source of additional overpressure?, Marine and Petroleum Geology, v. 17, p. 523-537.

Chapter 3: Consolidation Behavior, Stress, and Pressure of Sediments from ODP Site 1073, US Mid-Atlantic Continental Slope

Abstract

Pore pressures inferred from uniaxial strain consolidation tests equal 80% of the overburden stress in Pleistocene mudstones at Ocean Drilling Program (ODP) Site 1073 of the US mid-Atlantic continental slope, offshore New Jersey. High void ratios ($e > 0.8$) in Pleistocene sediments were preserved by low effective stress that was created by overpressure. In contrast, cementation preserved high void ratios of Miocene and Oligocene sediments; these void ratios do not record overpressure and low effective stress. One-dimensional models simulate overpressure and high void ratio in the Pleistocene sediments when an external fluid source is coupled with sediment loading at ODP Site 1073. Lateral fluid migration in the Oligocene-Miocene sediments, which are 2.5 times more permeable than overlying Pleistocene mudstones, is interpreted as the fluid source that maintains high void ratio and overpressure in the mudstones.

3.1 Introduction

Stress, pressure, and fluid flow influence the geomorphology of continental slopes. Consolidation behavior, permeability, and sedimentation rate control pressure and stress state (Gibson, 1958; Green and Wang, 1986). Overpressure drives fluids along permeability pathways; this flow field affects the timing and distribution of deformation and failure (Johnson, 1939; Rona, 1969; Boehm and Moore, 2002; Dugan and Flemings, 2002) and can generate landslides on low angle slopes (Terzaghi, 1950; Bombolakis, 1981).

Direct measurements of *in situ* pressure have documented overpressure in the shallow subsurface, but these measurements are rare. Davis and Becker (1994) and Becker *et al*. (1997) used long term Ocean Drilling Program (ODP) observatories to record overpressures up to 1 MPa, to infer upward fluid migration, and to estimate physical properties. Ostermeier *et al*. (2001) measured overpressure near the seafloor in high porosity, rapidly deposited mudstones in the Gulf of Mexico. In lieu of direct measurements, *in situ* stress and pressure are inferred from consolidation behavior. Consolidation experiments are used to estimate *in situ* effective stress, fluid pressure, permeability, and sediment compressibility in accretionary prisms (e.g. Karig, 1996; Saffer *et al*., 2000), gas hydrate provinces (e.g. Winters, 2000), and passive margins (e.g. Blum *et al*., 1996; Stump and Flemings, 2002).

We used uniaxial strain consolidation tests to characterize the pressure and stress of Oligocene-Pleistocene sediments from ODP Site 1073, Hudson Apron, US mid-Atlantic con-

tinental slope (Figure 3.1). We documented the elastic and elasto-plastic (virgin)

deformation of the sediments. From this we estimated the maximum effective stress that

the sediments have experienced (preconsolidation stress, σ_{pc}'). We used σ_{pc}' to constrain

the minimum *in situ* fluid pressure. We also estimated *in situ* conditions by measuring the

ratio of horizontal to vertical stress required for uniaxial strain. We then developed a one-

dimensional model to constrain the flow and depositional conditions that explain the high

void ratio and overpressure of the Hudson Apron.

3.2 Overview

3.2.1 Geologic Setting

ODP Site 1073 is located on the Hudson Apron in 639 m of water (Figure 3.1A). The site

was drilled to 663 m below sea floor (mbsf) through a thick Pleistocene sedimentary pack-

age that is underlain by thin layers of Pliocene, Miocene, and Oligocene sediments (Fig-

ures 3.1B, 3.2) (Shipboard Scientific Party, 1998).

Oligocene through Pliocene sedimentation rates were low (< 0.1 mm yr^{-1} at ODP Site

1073) on the Hudson Apron and increased during the Pleistocene (average of 0.67 mm

yr^{-1} at ODP Site 1073) (Figure 3.2) (Shipboard Scientific Party, 1998). The Oligocene and

Miocene depositional conditions were suitable for the *in situ* formation of a regional,
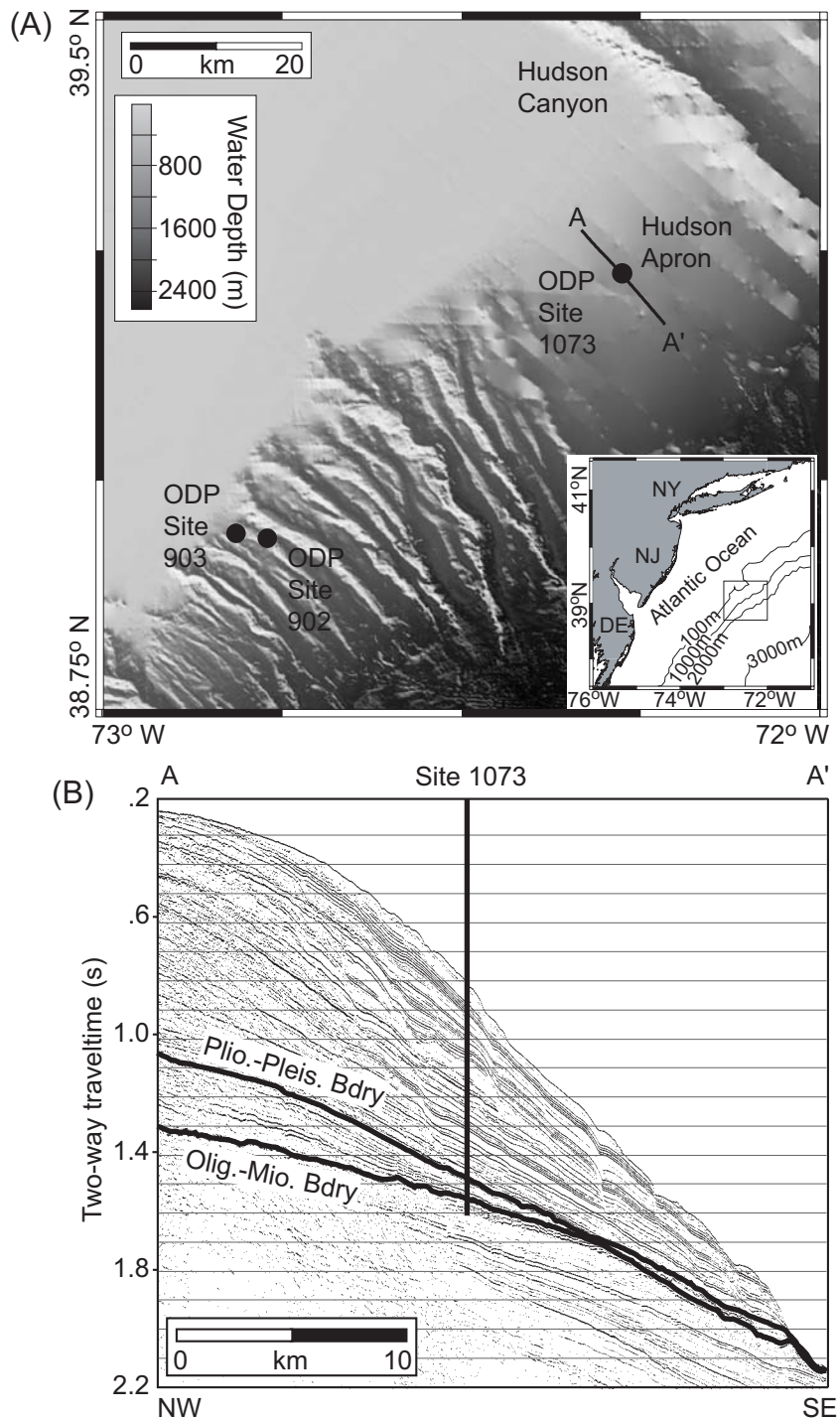
Figure 3.1: (A) Bathymetry in the region of ODP Site 1073, US mid-Atlantic continental slope. Inset shows the location of study region relative to east coast of North America. ODP Sites 902 and 903 are locations of nearby geotechnical analyses (Blum *et al*., 1996). (B) Seismic cross section A-A' (located in Figure 3.1A) showing the regional stratigraphy of the Hudson Apron. Pliocene-Pleistocene boundary (Plio.-Pleis. Bdry) and Oligocene-Miocene boundary (Olig.-Mio. Bdry) are identified. Vertical scale is in two-way travel time; 1 second two-way traveltime is approximately 1 km.

glauconitic silt and sand layer (Hesselbo and Huggett, 2001). This regional layer was rap-

idly and differentially buried by finer-grained Pleistocene sediments (Figure 3.1B).

3.2.2 Sample Descriptions

The Oligocene samples (Table 3.1; Figure 3.2) are dark greyish brown to very dark greyish

green on a fresh surface. The samples are dominated by glauconite (40%) and illite (32%)

and have a median grain size of 13.6 μm (Table 3.1). Initial void ratio of the samples (e_i)

was 0.942 (ϕ_i = 48.5%; $e = \phi/(1-\phi)$; Figure 3.2; Appendix B). The Pleistocene samples

(Figure 3.2; Table 3.1) are olive-grey silty clay, on a fresh surface, with median grain sizes

of 3.9 - 7.2 μm (Table 3.1). The samples are predominantly smectite, illite, and quartz

(Table 3.1). Initial void ratio of the samples (e_i) decreased from 1.08 (ϕ_i = 52%) at 64 mbsf

to 0.884 (ϕ_i = 47%) at 372 mbsf (Figure 3.2; Table 3.1).

3.3 Experimental Analysis

Uniaxial strain consolidation experiments were performed on samples from four depths

(Figure 3.2; Table 3.1). Dugan *et al*. (2002) described the experimental procedures and

presented the raw data. Effective vertical (axial) stress (σ_v') was prescribed during the

experiments while the effective horizontal (radial) stress (σ_h') required to maintain uniax-

ial strain was measured. Samples were first loaded to an isostatic effective stress of ~0.2

MPa. This was followed by uniaxial strain loading at 0.7 kPa min^{-1} to σ_v' = 5.2 MPa.
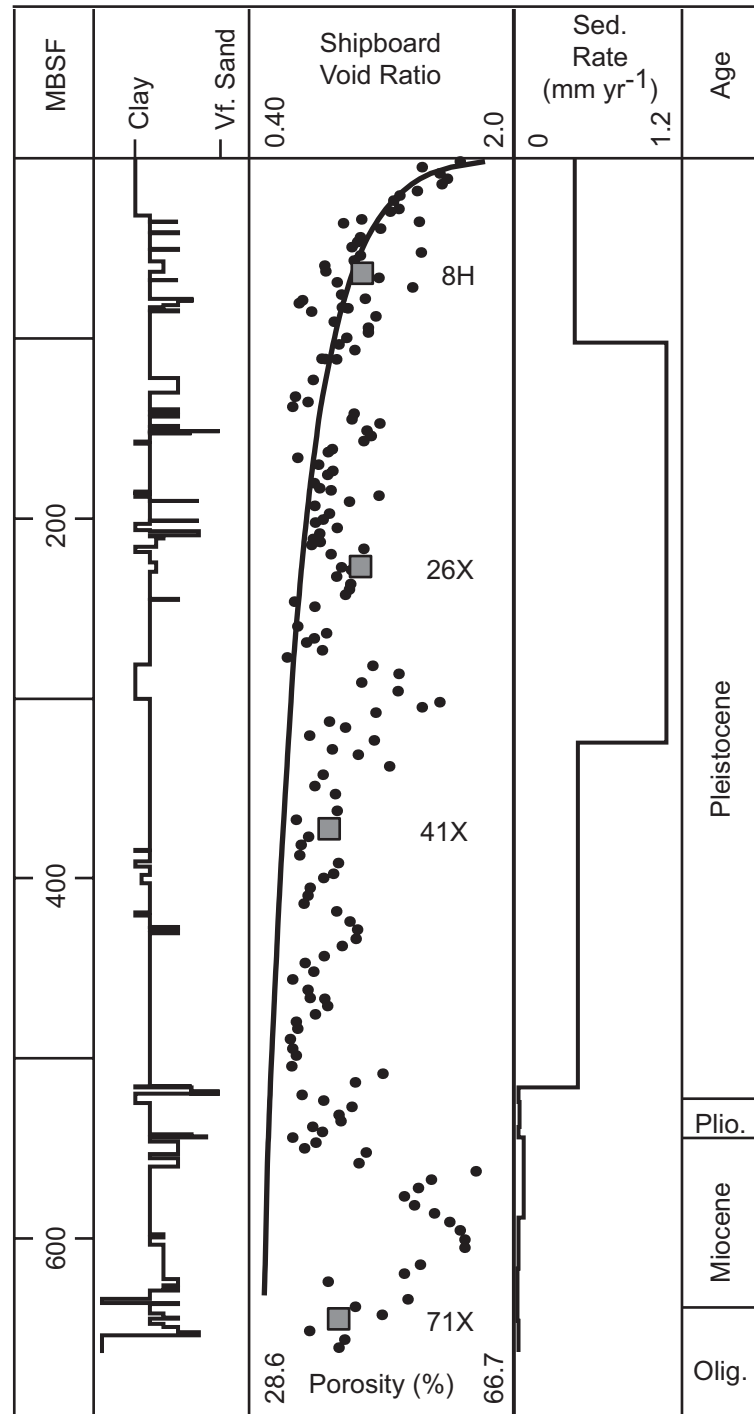
Figure 3.2: Shipboard observations (Shipboard Scientific Party, 1998) and interpretations from ODP Site 1073 (located in Figure 3.1). Lithology is dominantly silty clay with some very fine sand (Vf. Sand). Initial void ratio of samples (Equation B1) used in this study (grey squares) are plotted relative to shipboard void ratios measurements (black dots). Solid line is modelled void ratio (Equation 3.1) assuming hydrostatic fluid pressure, e_o of 0.85, and C_c of 0.51. Equivalent porosity is labeled on the void ratio column. Sedimentation rates (Sed. Rate) and ages are based on shipboard dates.

63

Table 3.1: Sample Summary

Sample	Depth (mbsf)	Geologic Age (my)	Grain Density (kg m^{-3})	e_i (%)	Median Grain Size (μm)	Sed. Rate (mm yr^{-1}) (McHugh and Olson, 2002; Shipboard Scientific Party, 1998)]	Composition	Experiment
8HA/8HB	63.75	Pleistocene (~0.067)	2720	1.08	3.9	0.37	15% quartz, 3% K-feldspar, 4% plagioclase, 0.5% calcite, 3% dolomite, 5% amphibole, 0.2% pyrite, 45.5% smectite, 15.4% illite, 2% glauconite	(A) consolidation (B) permeability
26XB	226.65	Pleistocene (~0.340)	2740	1.07	6.4	5.6	38% quartz, 5% K-feldspar, 19% plagioclase, 1% dolomite, 1% amphibole, 1% gypsum, 1% pyrite, 34% clay	consolidation
41X	372.35	Pleistocene (~0.517)	2740	0.884	7.2	62	30% quartz, 5% K-feldspar, 20% plagioclase, 13% calcite, 3% dolomite, 2% amphibole, 27% clay	consolidation
71XA /71XB	644.70	Oligocene (34.2-35)	2650	0.942	13.6	< 0.01	9% quartz, 1% K-feldspar, 1% plagioclase, 1.4% calcite, 0.6% amphibole, 1.4% pyrite, 12.4% smectite, 31.8% illite, 40.5% glauconite	(A) consolidation (B) permeability

Samples were then unloaded at 0.7 kPa min^{-1} to 4.2 MPa. Sample 8HA (64 mbsf) was subsequently loaded to 13 MPa at 0.7 kPa min^{-1}. Permeability was measured with constant flux experiments on Samples 8HB (64 mbsf) and 71XB (645 mbsf) under isostatic loading to 5 MPa.

3.3.1 Consolidation Results

We first describe the experimental results for Sample 8HA (64 mbsf). This sample was loaded to the highest stress and had an unload-reload cycle. We then describe the remaining experimental results working upward from the base of ODP Site 1073.

A uniaxial strain consolidation experiment performed on a sediment sample buried under uniaxial strain conditions will have a characteristic deformation behavior. On a void ratio-log(stress) [e-log($\sigma_v{}'$)] plot, deformation begins with a low and constant slope followed by a zone of increased and constant slope. Unload-reload cycles should parallel the initial load until $\sigma_v{}'$ exceeds the past maximum stress the sample experienced; then deformation will proceed with an increased and constant slope (Lambe and Whitman, 1979). The void ratio of sediments deforming along the yield surface is described by Equation 3.1 (e.g. Terzaghi, 1943; Lambe and Whitman, 1979).

$$e \; = \; e_o - C_c \log(\sigma_v{}') \qquad , \qquad\qquad\qquad\qquad (3.1)$$

where e_o is the void ratio at $\sigma_v' = 1$ MPa. C_c is the compression index describing deformation along the yield surface (i.e. virgin deformation; Appendix B). All variables are defined in the nomenclature table (Table 3.2).

Sample 8HA (64 mbsf) showed a different deformation behavior described by three e-log(σ_v') zones (Figure 3.3A): (1) deformation with increasing slope (< 1.2 MPa); (2) consolidation with constant and high slope (1.2-5.15 MPa and 5.5-13 MPa); and (3) expansion/recompression with constant and low slope during unloading/reloading (5.15-4.2 MPa; 4.2-5.0 MPa).

We interpret that the zone of increasing slope results from sample disturbance. Strains induced by coring, the stress decrease during sample extraction, and damage during sample preparation cause disturbance. Experimental studies have shown that disturbance increases the e-log(σ_v') slope at $\sigma_v' < \sigma_{pc}'$ and produces a rounded consolidation curve (La Rochelle *et al*., 1981; Santagata and Germaine, 2002). Sample 8HA (64 mbsf) has a rounded consolidation curve from 0.3 to 2.0 MPa (Figure 3.3A). The disturbance overprints the low, constant slope that should be observed during the initial load. At stresses between 2 and 5.12 MPa, Sample 8HA (64 mbsf) has a constant slope ($C_c = 0.31$; Table 3.3). We interpret that this linear behavior represents virgin consolidation (i.e. deformation at stresses above the maximum stress to which the sample has been exposed).

Table 3.2: Nomenclature

Variable	Definition	Dimensions
C_c	compression index	dimensionless
C_e	recompression/expansion index	dimensionless
e	void ratio	dimensionless
e_i	initial void ratio	dimensionless
e_o	reference void ratio	dimensionless
g	acceleration due to gravity	L/T^2
k	permeability	L^2
K_o	coefficient of earth pressure at rest	dimensionless
l	sample length	L
m	sample mass	M
m_v	coefficient of volume compressibility	LT^2/M
P^*	overpressure	M/LT^2
Q	fluid flux	L^3/T
r	sample radius	L
S_t	storage coefficient	LT^2/M
t	time	T
u	fluid pressure	M/LT^2
u_h	hydrostatic pressure	M/LT^2
V	sample volume	L^3
z	depth below sea level	L
β_f	fluid compressibility	LT^2/M
ΔP	differential pressure	M/LT^2
$\Delta\sigma_v'$	effective stress increment	M/LT^2
ϕ	porosity	dimensionless
ϕ_i	initial porosity	dimensionless
λ^*	normalized overpressure	dimensionless

Table 3.2: Nomenclature (continued)

Variable	Definition	Dimensions
ρ_b	bulk density	M/L^3
ρ_s	grain density	M/L^3
ρ_w	water density	M/L^3
$\sigma_c{}'$	confining stress	M/LT^2
$\sigma_{pc}{}'$	preconsolidation stress	M/LT^2
$\sigma_h{}'$	effective horizontal (radial) stress	M/LT^2
σ_v	overburden stress	M/LT^2
$\sigma_v{}'$	effective vertical (axial) stress	M/LT^2
$\sigma_{vh}{}'$	hydrostatic effective stress	M/LT^2
μ	dynamic viscosity	M/LT
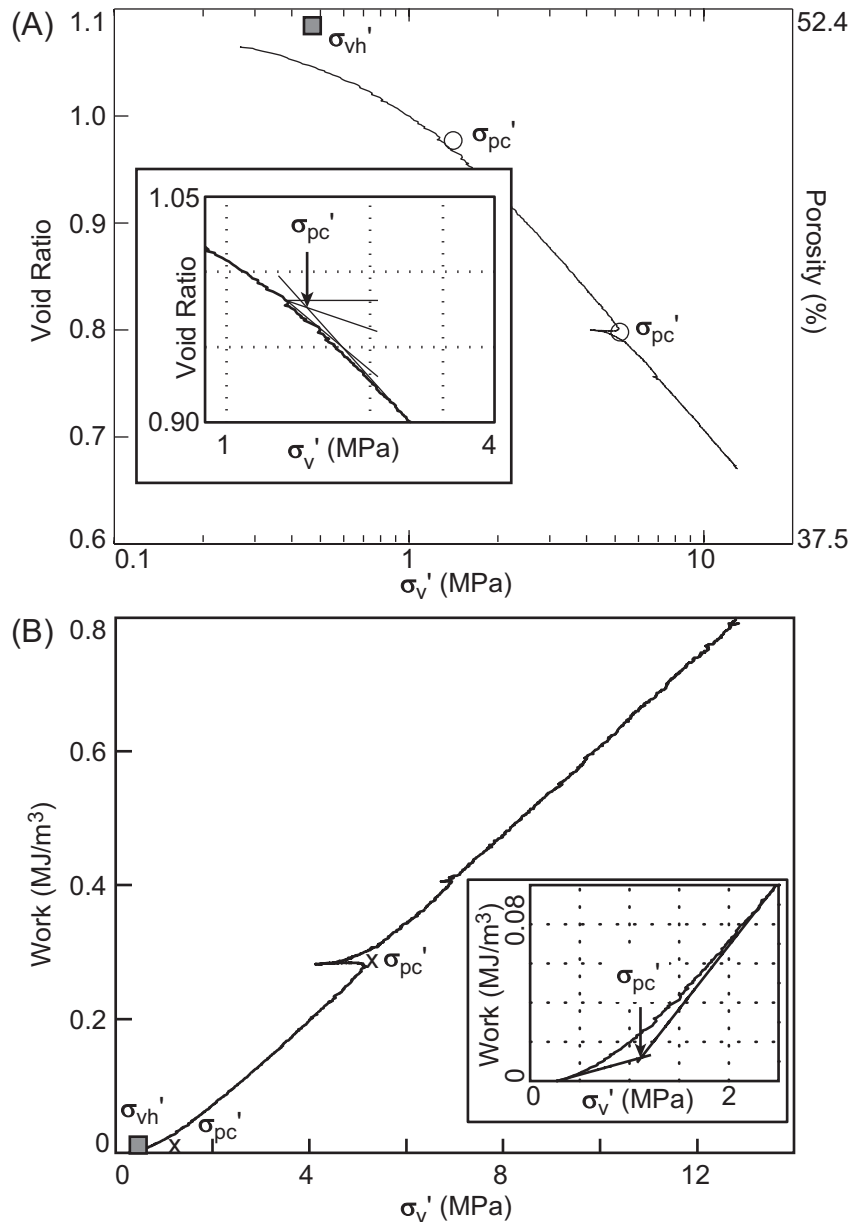
Figure 3.3: Consolidation experiment results for Sample 8HA (64 mbsf). (A) In the e-log(σ_v') plot, slope increases until virgin consolidation is achieved ($\sigma_v' > 2$ MPa). Virgin consolidation continues until unloading (5.15 to 4.2 MPa); after reloading deformation returns to the virgin consolidation trend. Grey square is the initial void ratio measured on Sample 8HA plotted against its hydrostatic effective stress (σ_{vh}'). Preconsolidation stresses (open circles) are based on the methodology of Casagrande (1936). Inset shows the Casagrande determination of σ_{pc}' (Casagrande, 1936) on the initial load. Equivalent porosity is labeled on the right vertical axis. (B) In a work-stress plot (Becker _et al._, 1987), virgin consolidation is identified as the linear trend from 2-5.15 MPa and during the reload at stresses above 5.5 MPa. Hydrostatic effective stress (grey square, σ_{vh}') is labeled for comparison to σ_{pc}' (x's). Inset shows the determination of the initial load σ_{pc}' by the intersection of the linear extrapolations of the initial load and the virgin deformation (Becker _et al._, 1987).

Table 3.3: Compression and Expansion Indices

Sample	C_c (stress range of constraint in MPa)	C_e (stress range of constraint in MPa)
8HA Initial Load	0.31 (2.00-5.12)	0.013 (4.91-4.15)
8HA Reload	0.32 (6.00-12.95)	0.050 (4.22-4.73)
26XB	0.38 (2.00-5.17)	0.025 (4.90-4.14)
41X	0.23 (2.00-5.18)	0.017 (4.91-4.22)
71XA	0.29 (4.02-5.15)	0.016 (4.68-4.15)
Core void ratio (0-85 mbsf)	0.51 (0.01-0.62)	-

Elastic deformation of Sample 8HA is observed in the unload-reload cycle where the e-log(σ_v') plot is nearly flat (Figure 3.3A). The expansion/recompression index (C_e) ranges from 0.01 to 0.05 (Table 3.3). C_e defines elastic deformation along the unload-reload path (Appendix B). The unload-reload slopes are less then those measured during initial loading (Figure 3.3A). This is a characteristic of disturbed samples (Santagata and Germaine, 2002). Deformation returns to the virgin consolidation trend ($C_c = 0.32$) at σ_v' above 5.5 MPa (Figure 3.3A; Table 3.3).

We determined preconsolidation stress (σ_{pc}') with two approaches: (1) the Casagrande method (Casagrande, 1936) and (2) the work-stress method (Becker *et al*., 1987). The Casagrande method is based on the curvature of the e-log(σ_v') plot and the virgin consolidation curve (Figure 3.3A inset). The work-stress method assumes linear behavior for consolidation at low stress and for virgin consolidation (Figure 3.3B inset). A third σ_{pc}' analysis that accounts for sample disturbance (Schmertmann, 1955) was also evaluated. The results of the Schmertmann method (Schmertmann, 1955) were similar to the Casagrande and work-stress methods; therefore, they are not presented.

The Casagrande estimate of σ_{pc}' for Sample 8HA (64 mbsf) is 1.42 MPa (Figure 3.3A; Table 3.4), nearly three times the hydrostatic vertical effective stress (σ_{vh}'; Appendix B). The work-stress σ_{pc}' estimate also exceeds σ_{vh}' (Figure 3.3B; Table 3.4). We interpret that the high preconsolidation stress results from sample disturbance. Santagata and Germaine (2002) experimentally determined that disturbance can produce high σ_{pc}' estimates. The

e-logσ_v' of Sample 8HA (64 mbsf) lacks a distinct break in slope, and the linear, virgin

consolidation trend was not achieved until stress exceeded σ_{vh}'; this produced a high σ_{pc}'

estimate. We consider σ_{vh}' as the upper bound on *in situ* stress for Sample 8HA (64 mbsf)

because no unloading (e.g. erosion) is evident in core or seismic data.

The Casagrande and work-stress analyses on the reload of Sample 8HA (4.2-13 MPa) pro-

duced σ_{pc}' of 5.20 and 5.22 MPa (Table 3.4). Prior to the reload, the sample was consoli-

dated to a maximum stress of 5.15 MPa. The similarity of σ_{pc}' to the maximum stress

demonstrates the application of these methods at ODP Site 1073.

Sample 71X (645 mbsf) had the least deformation during loading (Figure 3.4). The e-

log(σ_v') had a slight increase in slope from 0.2 - 4.2 MPa after which virgin consolidation

occurred (C_c = 0.29; Figure 3.4; Table 3.3). The small void ratio change during loading to

~4 MPa is interpreted to result from high strength caused by intergranular calcite cement

(Table 3.1) (Dugan *et al*., 2002). The increased deformation rate above 4 MPa measured

consolidation after the strength of the cement was exceeded. The elastic, unloading behav-

ior had a small void ratio change (C_e = 0.016; Table 3.3). The Casagrande estimate of σ_{pc}'

was 3.80 MPa (Figure 3.4; Table 3.4), whereas the work-stress analysis estimate was 3.19

MPa (Table 3.4). Both σ_{pc}' estimates are lower than σ_{vh}' (Figure 3.4; Table 3.4). Because

of the cement, we interpret that σ_{pc}' measures the strength of the cement and not the *in*

situ stress.

Table 3.4: Stress and Pressure for Experiment Samples

Sample	Depth (mbsf)	σ_v (MPa)	u_h (MPa)	$\sigma_{vh}{}'$ (MPa)	Void ratio-predicted $\sigma_v{}'$ (MPa)	Casagrande $\sigma_{pc}{}'$ (MPa)	Work-stress $\sigma_{pc}{}'$ (MPa)	K_o minimum (MPa)
8HA	63.75	7.55	7.08	0.47	0.38	1.42	1.15	0.43
8HA Reload	-	-	-	5.15	-	5.20	5.22	4.79
26XB	226.65	10.62	8.72	1.90	0.40	1.02	1.30	0.60/1.50
41X	372.35	13.34	10.18	3.16	1.02	0.85	1.51	0.81
71XA	644.70	18.33	12.93	5.4	0.77	3.80	3.19	2.33
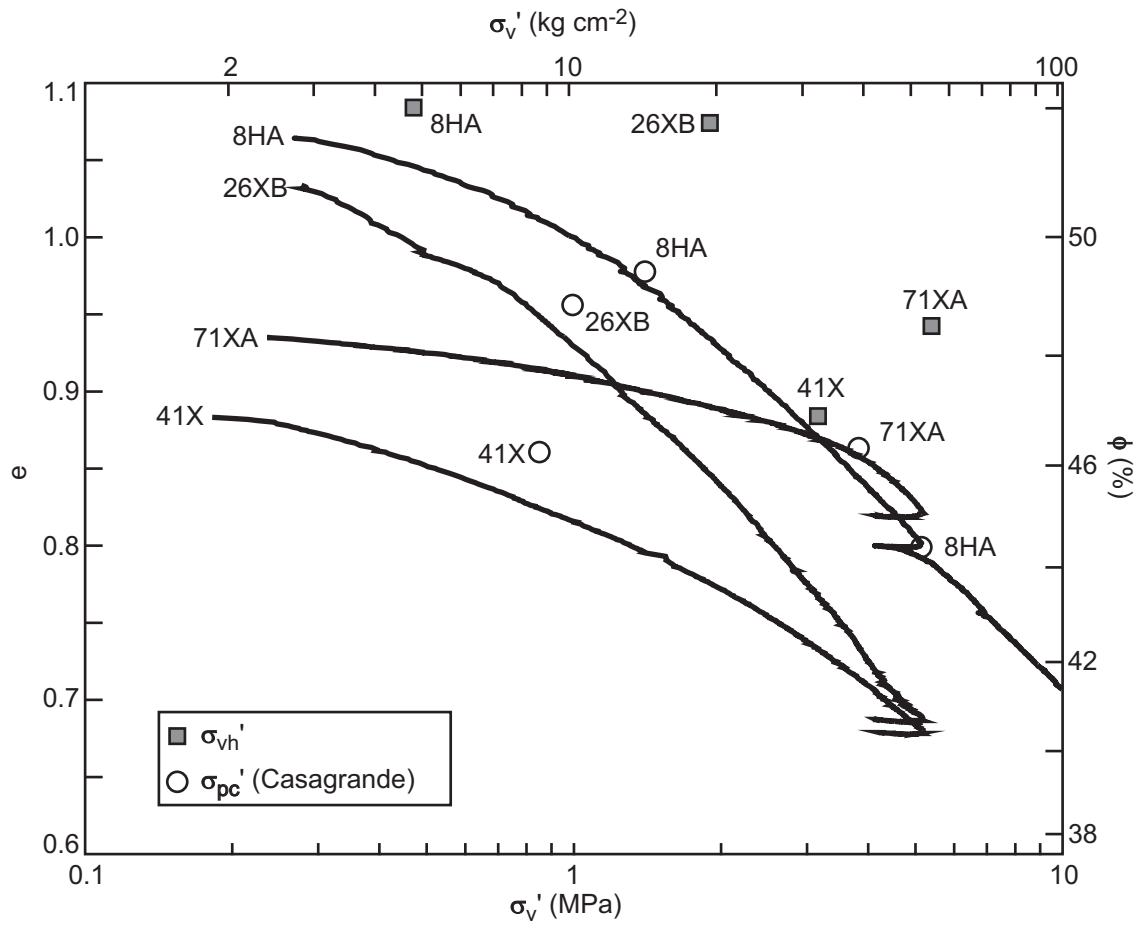
Figure 3.4: Consolidation results for Samples 8HA (64 mbsf), 26XB (227 mbsf), 41X (372 mbsf), and 71XA (645 mbsf); equivalent porosity is plotted on the right vertical axis. Grey squares are initial void ratio (Equation B1) of each sample plotted at its hydrostatic effective stress (σ_{vh}'). Open circles are σ_{pc}' determined by the Casagrande method (Casagrande, 1936).

Sample 41X (372 mbsf) had a linear e-log(σ_v') profile at $\sigma_v' > 2$ MPa. We inferred this to be the virgin consolidation trend: $C_c = 0.23$ (Figure 3.4; Table 3.3). C_e during unloading is similar to consolidation during initial loading (< 0.3 MPa) (Figure 3.4). The Casagrande analysis yielded σ_{pc}' of 0.85 MPa, which is lower than σ_{vh}' (3.16 MPa). The work-stress analysis provided a σ_{pc}' estimate of 1.51 MPa (Figure 3.4; Table 3.4). Similar to Sample 8HA (64 mbsf), we infer some sample disturbance based on the rounded e-log(σ_v') plot; therefore our estimates of *in situ* stress may be high (Santagata and Germaine, 2002).

The e-log(σ_v') plot for Sample 26XB (227 mbsf) did not have a well-defined break in slope (Figure 3.4). The plot was initially steep (0.3 - 0.5 MPa), then relatively flat (0.5 - 0.7 MPa), and finally slope increased until $\sigma_v' = 2$ MPa. Slope was constant from 2 to 5 MPa ($C_c = 0.38$; Table 3.3). The unload cycle had a C_e of 0.025 (Table 3.3). We inter- preted a preconsolidation stress of 1.02 MPa from the e-log(σ_v') data (Figure 3.4; Table 3.4). The work-stress analysis yielded a preconsolidation stress of 1.30 MPa (Table 3.4). In comparison to σ_{vh}', our preconsolidation stress estimates are at least 0.6 MPa lower (Table 3.4).

3.3.2 Laboratory versus In Situ Compression Behavior

Experimental compression indices ranged between 0.23 and 0.38 (Table 3.3). No relation between the compression indices and mineralogy or grain size exists (Tables 3.1, 3.2). Cementation influenced deformation of the Oligocene sample at low stresses (Figure 3.4).

Elastic deformation (C_e) of the samples was approximately 10% of the elasto-plastic

deformation (C_c) (Figure 3.4; Table 3.3). Karig (1996) and Blum *et al*. (1996) observed

similar recompression/expansion and compression behavior of silt and clay sediments.

C_c of 0.51 and e_o of 0.85 were constrained from 0-85 mbsf at ODP Site 1073. The con-

stants (Equation 3.1; Figure 3.2) was estimated assuming hydrostatic fluid pressures over

this depth interval. This compression index exceeded experimental values (Table 3.3).

Laboratory experiments are dominated by primary consolidation (e.g., grain re-orienta-

tion) that occurs over short time scales (e.g., days to weeks). *In situ* deformation occurs

over geologic time and is controlled by primary and secondary consolidation (Wood,

1990). Secondary consolidation increases the total deformation, makes the sample appear

more compliant, and thus produces a higher C_c.

3.3.3 Fluid Pressures

Two independent approaches were used to estimate *in situ* overpressure (P^*): (1) correla-

tion of core void ratio with a virgin consolidation trend (Equation 3.2; $C_c = 0.51$, $e_o = $

0.85); and (2) comparison of preconsolidation and hydrostatic effective stresses (Equation

3.3):

$$P* \ = \ \sigma_v - 10^{\left(\frac{e_o - e}{C_c}\right)} - u_h \quad .$$

(3.2)

$$P* \ = \ \sigma_{vh}{}' - \sigma_{pc}{}' \quad .$$

(3.3)

All variables are defined in the nomenclature table (Table 3.2)

Overpressure from core void ratio equals the overburden stress in the Oligocene-Miocene section (Figure 3.5) where void ratios are high (Figure 3.2). In most of the Pleistocene section (150-500 mbsf), pressure from void ratio increases at a lithostatic gradient (Figure 3.5). From the sea floor to 150 mbsf, the inversion yielded near-hydrostatic fluid pressure. The overpressure determined from preconsolidation stresses were similar to void ratio predicted overpressure in the Pleistocene section but differed in the Oligocene sediments (Figure 3.5). The Oligocene sample (Sample 71XA, 645 mbsf) was interpreted to have moderate overpressure.

The Oligocene-Miocene sediments had extremely high *in situ* void ratios (Figure 3.2), which equated to overpressure of ~ 5 MPa (Equation 3.3). From the *e*-logσ_v' path of Sample 71XA (645 mbsf), we estimated the cement strength and inferred that it represents a maximum value for the *in situ* stress. If *in situ* stress were higher, the cements would have yielded and lower void ratios would have been observed as documented experimentally (Figure 3.4). This maximum stress estimate correlates to overpressure of 1.6 - 2.2 MPa (Equation 3.2; Figure 3.5). These estimates are a lower bound on overpressure based on the cement strength, not the stress-strain history.
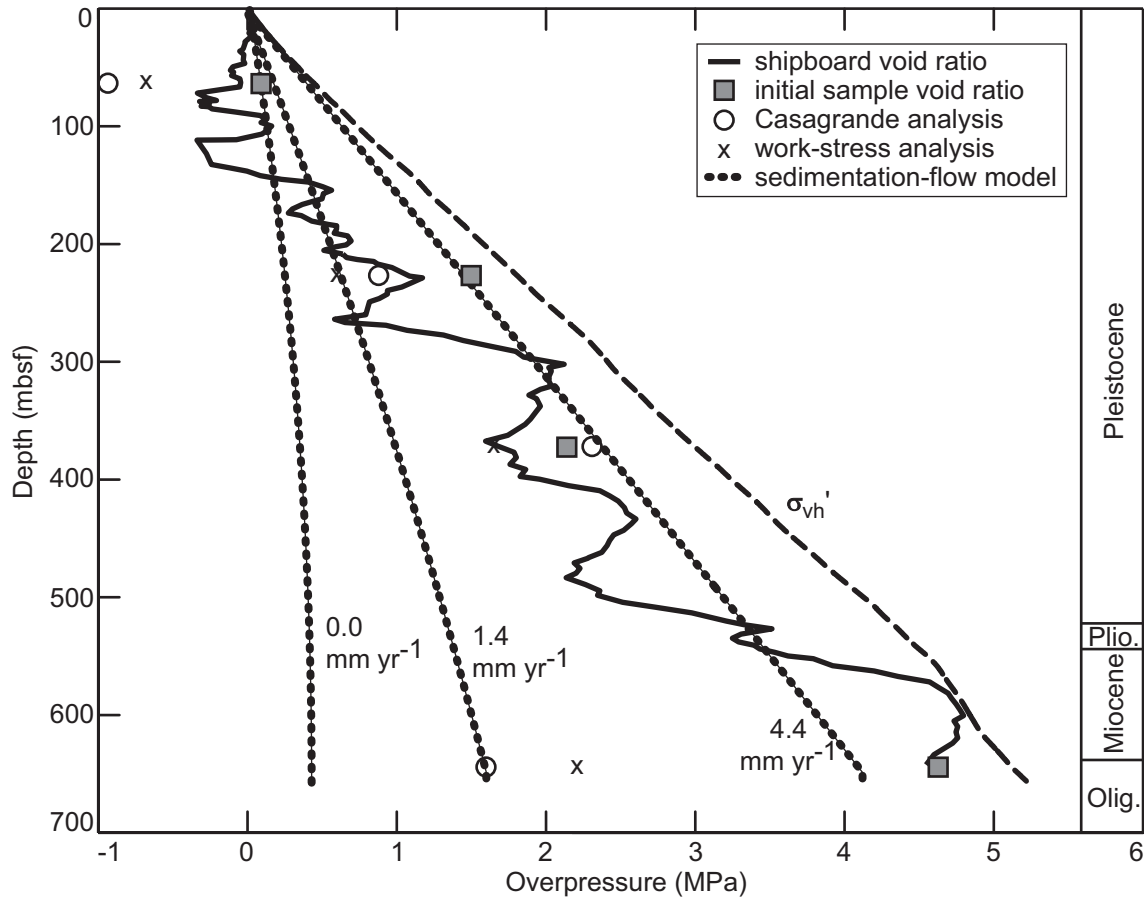
Figure 3.5: Overpressure plot for ODP Site 1073. The solid line is a moving average of the overpressure predicted from shipboard void ratio measurements (Equation 3.2). Overpressure from initial void ratio of experimental samples (grey squares) is from Equation 3.2. Overpressure estimates based on preconsolidation stresses from the Casagrande method (open circles) and the work-stress method (x's) are presented. Overpressure from all methods increases with depth. Overpressure gradient in the Pleistocene sediments is nearly lithostatic. Overpressure predictions for one-dimensional sedimentation model (Equation 3.5; dashed lines: no flow, 1.4 mm yr^{-1}, and 4.4 mm yr^{-1}) illuminate the role of an external fluid source in generating overpressure at ODP Site 1073.

Consolidation-based overpressures in the Pleistocene sediments are within 1 MPa of the void ratio estimates (Figure 3.5). Overpressure for Sample 41X (372 mbsf), based on consolidation experiments, is between 1.65 and 2.31 MPa. These estimates bound overpressure predictions from void ratio at 372 mbsf (Figure 3.5). Sample 26XB (227 mbsf) has predicted overpressure of 0.6 MPa (work-stress σ_{pc}') and 0.88 MPa (Casagrande σ_{pc}'). The void ratio-predicted overpressures exceed the σ_{pc}' predictions at 227mbsf. Sample 8HA (64 mbsf) has overpressure estimates ranging between 0.11 and -0.95 MPa (Figure 3.5). Negative overpressure indicates fluid pressure less than hydrostatic, an unrealistic condition for this location. We attribute the negative overpressure estimates to high σ_{pc}' values resulting from sample disturbance. We assume hydrostatic pressure for Sample 8HA based on the void ratio prediction and on the consolidation trend of the overlying and underlying sediments (Figure 3.2). Blum *et al*. (1996) interpreted near-hydrostatic pressures for depths less than 100 mbsf based on consolidation experiments of samples from nearby ODP Sites 902 and 903 (located in Figure 3.1).

The similar pressure predictions, in the Pleistocene sediments, from consolidation experiments and core void ratio demonstrates that shallow constraints can be applied to deeper sediments of similar rheology, mineralogy, and grain size, such as the Pleistocene section of ODP Site 1073 (Tables 3.1, 3.2; Figure 3.4). The stiffness of the cemented, Oligocene-Miocene sediments precluded reliable pressure estimates from void ratio based on the Pleistocene sediment properties.

3.3.4 Coefficient of Earth Pressure at Rest

The coefficient of earth pressure at rest is the ratio of horizontal to vertical effective stress under uniaxial strain conditions ($K_o = \sigma_h'/\sigma_v'$) (Craig, 1992). Our experiments began with isostatic loading ($K_o = 1$) to approximately 0.2 MPa. During uniaxial strain loading, K_o decreased to a minimum and then increased (Figure 3.6). K_o of the Pleistocene samples decreased during unloading (Figures 3.6A-3.6C). In contrast, K_o of the Oligocene sample was constant during unloading (Figure 3.6D).

Samples 8HA (64 mbsf), 26XB (227 mbsf), and 41X (372 mbsf) have K_o minima of approximately 0.44 that occur near the *in situ* stress (Figure 3.6; Table 3.4). This is followed by an increase in K_o to nearly constant values (Figure 3.6). A K_o value of approximately 0.6 at high stresses (e.g., Sample 8HA) paralleled silt and clay experimental results of Karig (1992). We also note that the reload of Sample 8HA (64 mbsf) has a K_o minimum at 4.79 MPa, which is similar to the maximum stress experienced by the sample prior to unloading (5.15 MPa) (Figure 3.6A; Table 3.4). Karig (1996) observed a similar relation on silty clay from ODP Site 897 where the minimum sediment modulus occurred at the preconsolidation stress. This systematic relation between K_o minima and the preconsolidation stress may prove to be useful when constraining *in situ* stress. Sample 71X (645 mbsf) had a K_o minimum of 0.27, did not approach a constant K_o value with increasing σ_v', and had a constant K_o during unloading (Figure 3.6). The low K_o values indicate high strength.
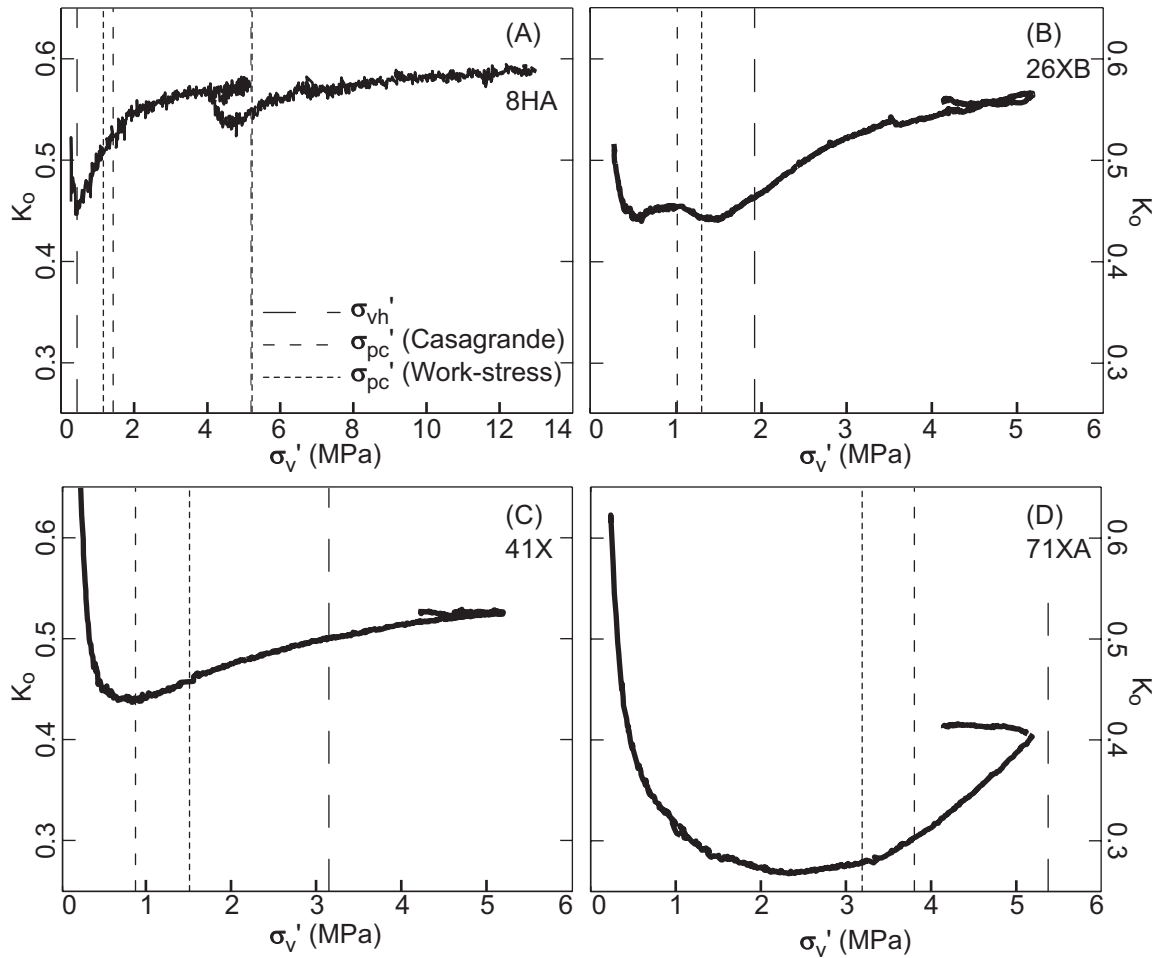
Figure 3.6: Coefficient of earth pressure at rest (K_o) as a function of vertical effective stress (σ_v') for (A) Sample 8HA (64 mbsf), (B) Sample 26XB (227 mbsf), (C) Sample 41X (372 mbsf), and (D) Sample 71X (645 mbsf). Hydrostatic effective stress (σ_{vh}') and preconsolidation stress (σ_{pc}') estimates are labelled (Table 3.4). Each sample shows a characteristic behavior where K_o decreases and then increases. The K_o minima for Samples 26XB (227 mbsf), 41X (372 mbsf), and 71X (645 mbsf) are similar to the preconsolidation stress estimates. Note: Figure 3.6A extends to σ_v' = 14 MPa whereas Figures 3.6B-3.6D extend to σ_v' = 6 MPa.

3.3.5 Permeability

Permeability (k) was measured on Samples 8HB (64 mbsf) and 71XB (645 mbsf) at multiple isostatic confining stresses (σ_c'). To determine k, a differential pressure (ΔP) was applied across the sample while the steady state fluid flux (Q), sample length (l), and sample radius (r) were monitored (Equation 3.4; Table 3.2).

$$k = \frac{\mu Q l}{\pi r^2 \Delta P} \qquad . \tag{3.4}$$

Permeability decreased with increasing effective stress (Figure 3.7A). The Oligocene sample (Sample 71XB, 645 mbsf) had its largest permeability decrease between $\sigma_c' = 2$ and $\sigma_c' = 3$ MPa (Figure 3.7). The mean stresses, $\left(\frac{\sigma_h' + \sigma_v'}{2}\right)$, associated with σ_{pc}' for Sample 71XA (645 mbsf) were 2.55 (Casagrande) and 2.04 (work-stress) MPa. These mean stresses coincide with the rapid permeability decrease on Sample 71XB (Figure 3.7A). We attribute the step-decrease in k to cement breakdown and reduction of pore-throat diameters. The Pleistocene sample (Sample 8HB, 64 mbsf) showed a steady permeability decrease with increasing σ_c'. Sample 8HB is finer-grained and has more clay than the Oligocene sample (Sample 71XB, 645 mbsf) (Table 3.1). This caused its lower permeability.
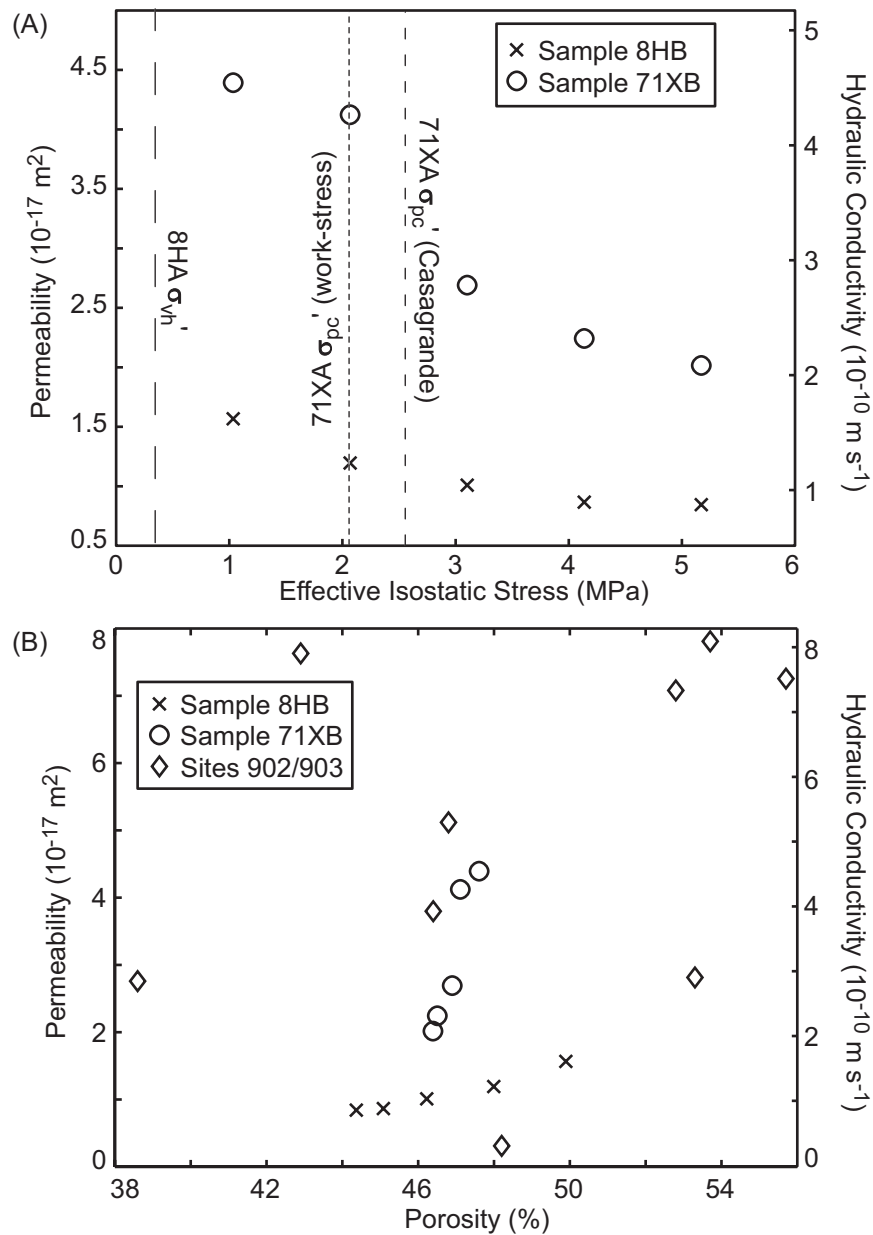
Figure 3.7: (A) Permeability as a function of stress for Samples 8HB (64 mbsf) and 71XB (645 mbsf) shows the lower permeability of the clay-rich Pleistocene sample relative to silt-dominated Oligocene sample. Sample 8HB has a consistent permeability-stress behavior interpreted to be a function of virgin consolidation at mean stresses exceeding σ_{vh}' of Sample 8HA. Step-decrease in permeability of Sample 71XB (645 mbsf) between 2 and 3 MPa is believed to result from increased consolidation after the breakdown of intergranular cement; the decrease occurs over the mean stress interval of the cement breakdown on Sample 71XA (σ_{pc}' from Casagrande and work-stress analyses). Hydraulic conductivity is labelled for reference. (B) Permeability as a function of porosity for Samples 8HB and 71X in comparison to measurement from ODP Sites 902 and 903 (located in Figure 3.1) (Blum *et al.*, 1996). Samples 8HB and 71X define the k-ϕ path for individual samples. Blum *et al.*'s (1996) are k-ϕ pair for separate samples. Our permeability experiments used a brine pore fluid (6% potassium chloride) with a dynamic viscosity (μ) of 9.7×10^{-4} Pa·s.

The permeability-porosity relations for the samples are quite different. Sample 71XB (645 mbsf) had a significant permeability decrease while porosity decreased from 47.6-46.4% (Figure 3.7B). The Pleistocene sample (Sample 8HB, 64 mbsf) experienced a smaller decrease in permeability but a larger decrease in porosity than the Oligocene sample (Figure 3.7B). These measurements describe how the permeability of individual samples changes with stress and porosity. The results are similar in value to individual porosity-permeability measurements from nearby ODP Sites 902 and 903 (Figure 3.7B) (Blum *et al.*, 1996). Blum *et al*. (1996) describe the permeability behavior at ODP Sites 902 and 903.

We combine our permeability measurements with core void ratio, lithology, and regional stratigraphy to interpret the permeability architecture of the Hudson Apron. Oligocene-Miocene sediments at ODP Site 1073 have a high void ratio, are coarser grained than the Pleistocene sediments, and are interpreted to hydraulic behavior similar to Sample 71XB; they are more permeable than the overlying Pleistocene mudstones. This results in a permeability structure where a thin, permeable layer is differentially covered by a lower permeability layer (e.g., Figure 3.8).
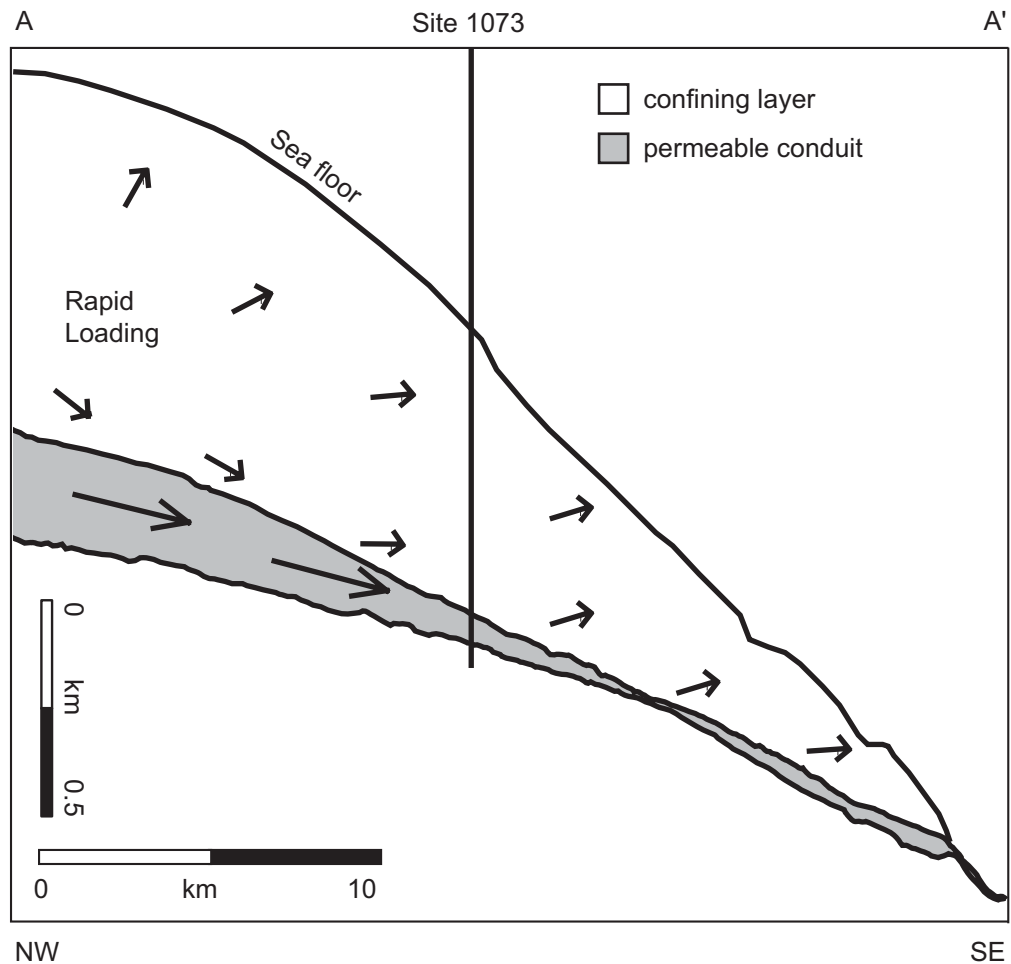
Figure 3.8: Line drawing of seismic cross-section (Figure 3.1B) overlain by conceptual two-dimensional flow system that redistributes fluids along the Hudson Apron. Fluid migration, driven by sediment loading, is focussed along high permeability lenses (grey-shaded) and discharged where overburden is thin. Arrows indicate flow directions and illustrate the difference in flow rates. Lateral transfer of fluids may provide the additional fluids to ODP Site 1073 that we predict are necessary to maintain the observed void ratio profile and interpreted overpressure.

3.4 Pressure Modelling

Dugan and Flemings (2000) proposed that high porosity along the Hudson Apron was controlled by a two-dimensional flow field where lateral flow along the Oligocene and Miocene sediments expelled fluids at the toe of these sediments (Figure 3.8). Two key components to the model were: (1) that Oligocene-Miocene sediments were more permeable than Pleistocene sediments and (2) that one-dimensional flow was not sufficient to generate high porosity and overpressure at ODP Site 1073. Our permeability measurements (Figure 3.7) confirmed higher permeability of the deeper, Oligocene sediments relative to the Pleistocene mudstones. We use a one-dimensional model (Equation 3.5), with our experimental compressibility and permeability values, to evaluate overpressure generation.

$$\frac{\partial u}{\partial t} = \left(\frac{k}{S_t \mu}\right) \nabla^2 P^* + \left[\frac{m_v}{m_v + \beta_f (1 - \phi)}\right]\frac{\partial \sigma_v}{\partial t} \quad . \tag{3.5}$$

S_t is the storage coefficient [$S_t = \phi m_v/(1-\phi) + \phi\beta_f$], m_v is the coefficient of volume compressibility, β_f is the fluid compressibility (5×10^{-10} Pa^{-1}), and μ is dynamic viscosity (1×10^{-3} Pa·s) (Table 3.2). $\frac{\partial \sigma_v}{\partial t}$ is defined by the sedimentation rate (Figure 3.2).

A uniform permeability of 1×10^{-17} m^2 was used based on our experimental results (Figure 3.7). A 50% porosity ($e = 1$) was assumed for all sediments (Figure 3.2). Compressibility

(m_v) was assumed constant (0.22 MPa^{-1}) based on the consolidation results for sediments

with e = 1 (Equation 3.2; Figure 3.2). The model had a hydrostatic boundary at the sea

floor ($P^* = 0.0$ MPa).

With these assumptions and no flow at the base of the system, very little overpressure is

simulated and the normalized overpressure, $\lambda^* = \dfrac{u - \rho_w g z}{\sigma_v - \rho_w g z}$, is ~0.08 (Figure 3.5). With flow

into the base of the system at 1.4 mm yr^{-1}-4.4 mm yr^{-1}, overpressure increases and λ^* is

0.3 - 0.8. These flow model results are compatible with the overpressure predictions from

consolidation experiments and void ratio observations (Figure 3.5).

Our one-dimensional model showed that the permeability and sedimentation rate at ODP

Site 1073 coupled with an additional fluid source simulates near lithostatic fluid pressure

(e.g., $\lambda^* = 0.8$) and high void ratio. Our model is one-dimensional, but we infer that the

extra fluid source is lateral flow (Figure 3.8). A two-dimensional flow field defined by the

regional sedimentation pattern and permeability architecture provides fluids to ODP Site

1073. Along the upper slope, thick Pleistocene accumulations consolidate and drive fluid

toward the sea floor and downward to the permeable Miocene and Oligocene sediments

(Figure 3.8). Fluids migrate laterally along the permeable lens and are discharged where

overburden is thin (Dugan and Flemings, 2000; Dugan and Flemings, 2002). For ODP Site

1073, fluids may have originated along the upper slope where Pleistocene sedimentation

rates were highest; discharge of these fluids from the Miocene/Oligocene sediments on the

middle and lower slope provide a fluid source to maintain the high void ratio and overpressure in the Pleistocene sediments (Figure 3.8).

3.5 Conclusions

We used uniaxial strain consolidation experiments to interpret overpressure that begins below 65 mbsf and increases at a lithostatic gradient in the Pleistocene sediments at ODP Site 1073 of the US mid-Atlantic continental slope. We estimate overpressure equal to 80% of the overburden stress in the Pleistocene sediments and up to 40% of the overburden stress in the Oligocene sediments. We conclude that high void ratio in the Pliocene-Pleistocene sediments along the US mid-Atlantic continental slope is controlled by overpressure. Overpressure is predicted in the Miocene and Oligocene sediments, but their high void ratio is controlled by cementation. The yield strength of the cements documented in experimental analysis provides a maximum estimate of the *in situ* stress otherwise the cement would have yielded *in situ*. A one-dimensional, sedimentation-flow model, with measured compressibility and permeability, simulated the conditions at ODP Site 1073. A two-dimensional flow field, with fluids migrating along the permeable Miocene-Oligocene sediments and then being discharged at the lower slope, maintains the high void ratio and overpressure of Pleistocene sediments on the Hudson Apron.

Acknowledgements

Appendix B: Experimental Relations and Constraints

Reference Porosity and Void Ratio

Initial porosity (ϕ_i) was calculated prior to experiments (Equation B1) assuming 100%

water saturation (water density, ρ_w, of 1022 kg m^{-3}) and using the grain density of the

sample (ρ_s) (Table 3.1).

$$\phi_i = \frac{\rho_s - \rho_b}{\rho_s - \rho_w} \qquad . \tag{B1}$$

Bulk density (ρ_b) was determined by measuring the mass (m) and volume (V) of each sam-

ple.

Stress-Strain Relations and Compression Indices

For the consolidation experiments, porosity was calculated at each stress assuming

incompressible grains and fully-drained conditions (Equation B2),

$$\phi_{\sigma_v' + \Delta\sigma_v'} = \frac{V_{\sigma_v'}\phi_{\sigma_v'} + (V_{\sigma_v' + \Delta\sigma_v'} - V_{\sigma_v'})}{V_{\sigma_v' + \Delta\sigma_v'}} \qquad . \tag{B2}$$

The compression index (Equation B3) characterizes virgin consolidation on the linear portion of the e-$\log(\sigma_v')$ plot (Craig, 1992),

$$C_c = \frac{e_{\sigma_v'} - e_{\sigma_v' + \Delta\sigma_v'}}{\log[(\sigma_v' + \Delta\sigma_v')/(\sigma_v')]} \quad . \tag{B3}$$

The recompression/expansion index (Equation B4) describes the elastic portion of the e-$\log(\sigma_v')$ plot (Craig, 1992). It is defined along the unloading/reloading curve,

$$C_e = \frac{e_{\sigma_v'} - e_{\sigma_v' + \Delta\sigma_v'}}{\log[(\sigma_v' + \Delta\sigma_v')/(\sigma_v')]} \quad . \tag{B4}$$

Hydrostatic Effective Stress

Hydrostatic effective stress ($\sigma_{vh}' = \sigma_v - u_h$) is the difference between total stress (σ_v) and hydrostatic fluid pressure ($u_h = \rho_w g z$). Total stress is determined by integrating the measured bulk density.

References

Becker, D.E., Crooks, J.H.A., Been, K., and Jefferies, M.G., 1987, Work as a criterion for determining *in situ* and yield stresses in clays, Canadian Geotechnical Journal, v. 24, p. 549-564.

Becker, K., Fisher, A.T., and Davis, E.E., 1997, The Cork Experiment in Hole 949C: Long-Term Observations of Pressure and Temperature in the Barbados Accretionary Prism, Proceedings of the Ocean Drilling Program Scientific Results, v. 156, p. 247-251.

Blum, P., Xu, J., and Donthireddy, S., 1996, Geotechnical properties of Pleistocene sediments from the New Jersey upper continental slope, *in* Mountain, G.S., Miller, K.G., Poag, C.W., and Twichell, D.C. (eds.), Proceedings of the Ocean Drilling Program, Scientific Results, Volume 150, College Station, Ocean Drilling Program, p. 377-384.

Boehm, A., and Moore, J.C., 2002, Fluidized sandstone intrusions as in indicator of paleo-stress orientation, Santa Cruz, California, Geofluids, v. 2, p. 147-161.

Bombolakis, E.G., 1981, Analysis of a Horizontal Catastrophic Landslide, *in* Carter, N.L., Friedman, M., Logan, J.M., and Stearns, D.W. (eds.), Mechanical Behavior of Crustal Rocks; The Handin Volume, Washington, American Geophysical Union, p. 251-258.

Casagrande, A., 1936, The determination of the pre-consolidation load and its practical significance, *in* Casagrande, A., Rutledge, P.C., and Watson, J.D. (eds.), Proceedings of the 1st International Conference on Soil Mechanics and Foundation Engineering, Volume 3, American Society of Civil Engineers, p. 60-64.

Craig, R.F., 1992, Soil Mechanics, London, Chapman & Hall, 427 p.

Davis, E.E., and Becker, K., 1994, Formation temperatures and pressures in a sedimented rift hydrothermal system; 10 months of CORK observations, holes 857D and 858G, Proceedings of the Ocean Drilling Program, Scientific Results, v. 139, p. 649-666.

Dugan, B., and Flemings, P.B., 2000, Overpressure and Fluid Flow in the New Jersey Continental Slope: Implications for Slope Failure and Cold Seeps, Science, v. 289, p. 288-291.

Dugan, B., and Flemings, P.B., 2002, Fluid flow and stability of the US continental slope offshore New Jersey from the Pleistocene to the present, Geofluids, v. 2, p. 137-146.

Dugan, B., Olgaard, D.L., Flemings, P.B., and Gooch, M.J., 2002, Data report: Bulk physical properties of sediments from ODP site 1073, *in* Christie-Blick, N., Austin Jr., J.A., and Malone, M.J. (eds.), Proceedings of the Ocean Drilling Program, Scientific Results, Volume 174A, College Station, Ocean Drilling Program, p. 1-62.

Gibson, R.E., 1958, The progress of consolidation in a clay layer increasing in thickness with time, Geotechnique, v. 8, p. 171-182.

Green, D.H., and Wang, H.F., 1986, Fluid pressure response to undrained compression in saturated sedimentary rock, Geophysics, v. 51, p. 948-956.

Hesselbo, S.P., and Huggett, J.M., 2001, Glaucony in ocean-margin sequence stratigraphy (Oligocene-Pliocene, offshore New Jersey, USA; ODP Leg 174A), Journal of Sedimentary Research, v. 71, p. 599-607.

Johnson, D.W., 1939, The Origin of Submarine Canyons: A Critical Review of Hypotheses, New York, Hafner, 126 p.

Karig, D.E., 1996, Uniaxial reconsolidation tests on porous sediments: mudstones from Site 897, *in* Whitmarsh, R.B., Sawyer, D.S., Klaus, A., and Masson, D.E. (eds.), Proceedings of the Ocean Drilling Program, Scientific Results, Volume 149, College Station, Ocean Drilling Program, p. 363-373.

Karig, D.E., and Hou, G., 1992, High-stress consolidation experiments and their geologic implications, Journal of Geophysical Research, v. 97, p. 289-300.

La Rochelle, P., Sarrailh, J., Tavenas, F., Roy, M., and Leroueil, S., 1981, Causes of Sampling Disturbance and Design of a New Sampler for Sensitive Soils, Canadian Geotechnical Journal, v. 18, p. 52-66.

Lambe, T.W., and Whitman, R.V., 1979, Soil Mechanics: SI Version, New York, John Wiley & Sons, 553 p.

McHugh, C.M.G., and Olson, H.C., 2002, Pleistocene chronology of continental margin sedimentation: new insights into traditional models, New Jersey, Marine Geology, v. 186, p. 389-411.

Ostermeier, R.M., Pelletier, J.H., Winker, C.D., and Nicholson, J.W., 2001, Trends in Shallow Sediment Pore Pressures - Deepwater Gulf of Mexico, Society of Petroleum Engineers, SPE/IADC 67772.

Rona, P.A., 1969, Middle Atlantic continental slope of United States; deposition and erosion, AAPG Bulletin, v. 53, p. 1453-1465.

Saffer, D.M., Silver, E.A., Fisher, A.T., Tobin, H., and Moran, K., 2000, Inferred Pore Pressures at the Costa Rica Subduction Zone: Implications for Dewatering Processes, Earth and Planetary Science Letters, v. 177, p. 193-207.

Santagata, M.C., and Germaine, J.T., 2002, Sampling Disturbance Effects in Normally Consolidated Clays, Journal of Geotechnical and Geoenvironmental Engineering, v. 128, p. 997-1006.

Schmertmann, J.H., 1955, The Undisturbed Consolidation Behaviour of Clay, Transactions of the American Society of Civil Engineers, v. 120, p. 1201-1233.

Shipboard Scientific Party, 1998, Site 1073, *in* Austin Jr., J.A., Christie-Blick, N., Malone, M.J., *et al*. (eds.), Proceedings of the Ocean Drilling Program, Initial Reports, Volume 174A, College Station, Ocean Drilling Program, p. 153-191.

Stump, B.B., and Flemings, P.B., 2002, Consolidation State, Permeability, and Stress Ratio as Determined from Uniaxial Strain Experiments on Mud Samples from the Eugene Island 330 Area, Offshore Louisiana, *in* Huffman, A.R., and Bowers, G.L. (eds.), Pressure regimes in sedimentary basins and their prediction, AAPG Memoir 76, p. 131-144.

Terzaghi, K., 1950, Mechanism of landslides, Application of geology to engineering practice: Berkey volume, New York, Geological Society of America, p. 83-123.

Terzaghi, K., 1943, Theoretical Soil Mechanics, London, Chapman and Hall, 510 p.

Winters, W.J., 2000, Stress History and Geotechnical Properties of sediment from the Cape Fear Diapir, Blake Ridge Diapir, and Blake Ridge, *in* Paull, C.K., Matsumoto, R., Wallace, P.J., and Dillon, W.P. (eds.), Proceedings of the Ocean Drilling Program, Scientific Results, Volume 164, College Station, TX, Texas A & M University, Ocean Drilling Program, p. 421-429.

Wood, D.M., 1990, Soil Behaviour and Critical State Soil Mechanics, Cambridge, Cambridge University Press, 462 p.

Chapter 4: Stress and Pressure of the US Mid-Atlantic Continental Slope from Core and Seismic Data

Abstract

Vertical effective stress interpreted from porosity and seismic velocity is less than 1 MPa in Pleistocene sediments of the US mid-Atlantic continental slope. Effective stress estimated from seismic velocity of the Miocene sediments increases to 8 MPa; however, porosity-estimated vertical effective stress at Ocean Drilling Program Sites 902-904 and 1073 is less than 1 MPa for much of the Miocene and Oligocene section. High porosity of the Miocene sediments yields these low estimates. The porosity of the Miocene-Oligocene sediments may record early cementation and therefore does not record stress. Cement increases velocity, which produces high stress estimates from seismic velocity data. Over-pressure estimates for the Miocene-Pleistocene sediments are greatest where Pleistocene accumulations are thickest. This demonstrates the importance of Pleistocene sediments in pressure generation and as a pressure seal. Overpressure generation was most rapid during periods with the highest Miocene and Pleistocene sedimentation rates. Flow focussing in permeable lenses controls regional pressure and stability. Miocene clinoforms with permeable layers provide steep surfaces and pressure sources that could have triggered slope failure and headward erosion of canyons along the US mid-Atlantic margin.

4.1 Introduction

The US mid-Atlantic continental slope has three distinct morphologies: (1) large river canyons; (2) small, slope-isolated canyons; and (3) smooth regions without erosional features (Figures 4.1, 4.2). Large river canyons record river systems during sea-level lowstands when major rivers, such as the Hudson River, extended out onto the continental shelf. In some regions, deposition has created a uniform and smooth slope (Figure 4.1). In other regions, erosional processes have created a slope incised with multiple canyons (Figures 4.1, 4.2). Two competing hypotheses have been formulated for the origin of these canyons: (1) downslope erosional processes initiated by oversteepening on the upper slope (Shepard, 198; Pratson *et al*., 1994; Pratson and Coakley, 1996); or (2) headward erosion initiated by lower slope failure (Johnson, 1939; Rona, 1969; Twichell and Roberts, 1982).

To test these hypotheses, we study the influence of sedimentation patterns, lithologic variability, and fluid flow on the slope stability. We characterize the lithology, porosity, pressure, and stress with borehole and seismic data from the US mid-Atlantic continental slope. Borehole data constrain local conditions and use seismic data to for regional analyses. We first describe the porosity and lithology at four Ocean Drilling Program (ODP) sites. Porosity data are used to estimate effective stress and pressure at each site. We use the borehole interpretations to constrain an interval velocity-effective stress relationship. The velocity-stress model is used to predict stress along two-dimensional, multi-channel seismic lines. We conclude with a discussion of how the regional variations in lithology, deposition, and fluid flow may create smooth, stable slopes and failed slopes.
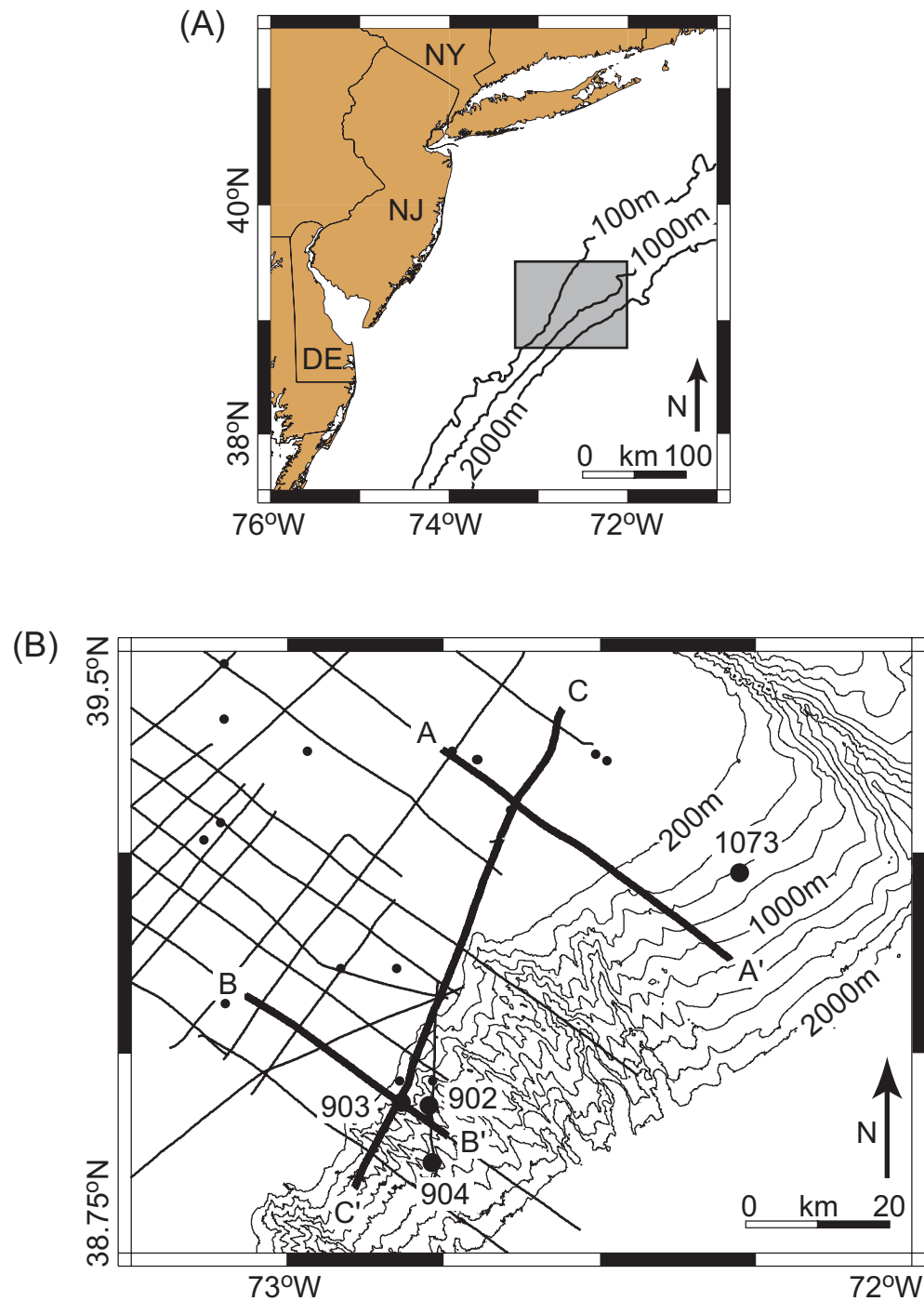
Figure 4.1: (A) Location of the study region along (grey box) the US mid-Atlantic continental slope. (B) Bathymetry of the study region. The slope has large paleoriver canyons, smooth canyonless regions, and small, slope-isolated canyons. Ocean Drilling Program Sites 902, 903, 904, and 1073 and seismic lines A-A', B-B', and C-C' are used to define lithology, stratigraphy, pressure, and stress in this study. Solid lines and circles are other seismic and well data in the region. Bathymetry contour interval is 200m.
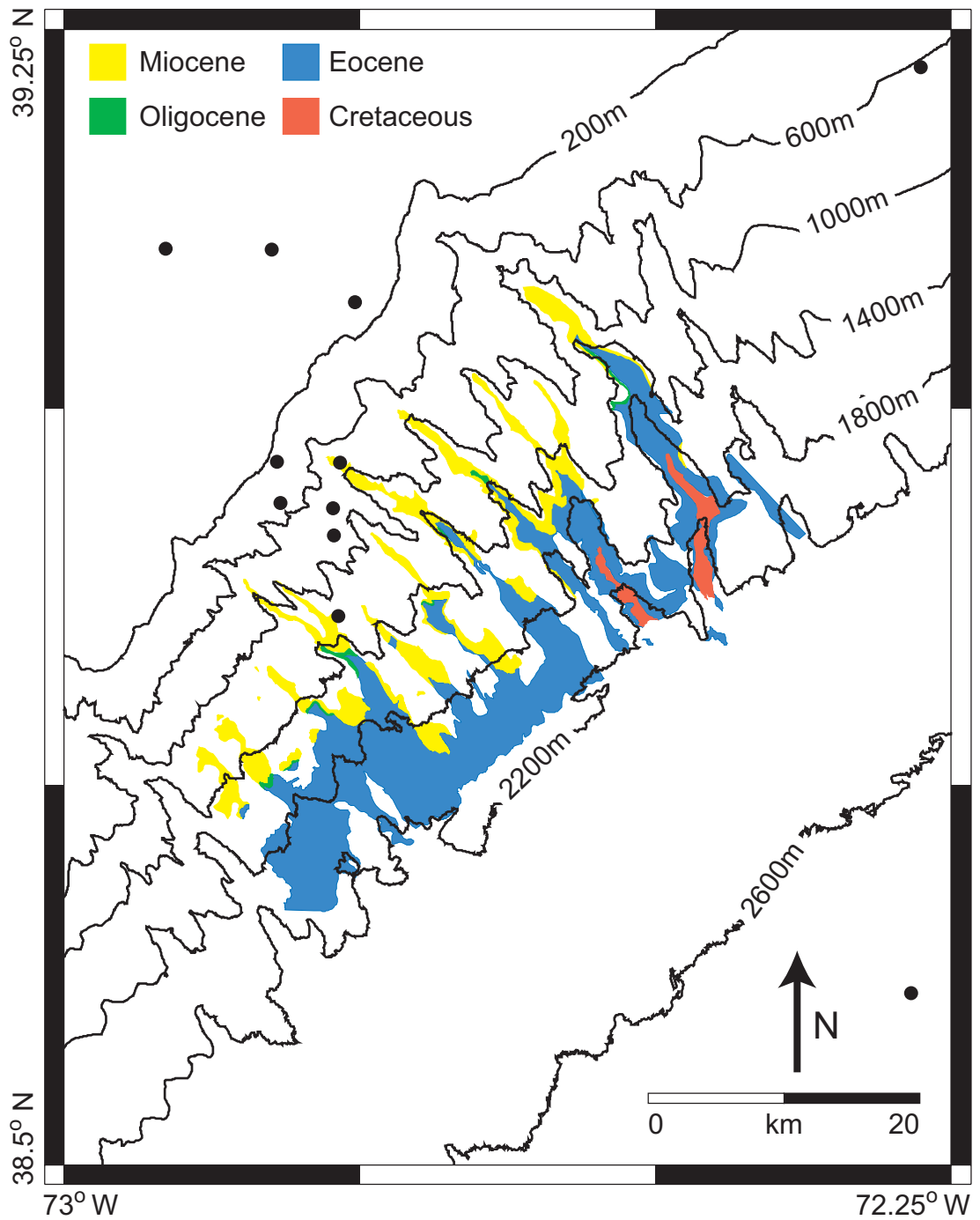
Figure 4.2: Bathymetric and outcrop map for a region of the slope with multiple slope canyons. Bathymetry contour interval is 200m. Ages of outcrop surfaces are color coded. Outcrop map modified from Hampson and Robb (1984). Uncolored sea floor is interpreted as Pleistocene sediments.

4.2 Overview

4.2.1 Geology

Oligocene through Pleistocene sedimentation on the US mid-Atlantic continental shelf and slope was dominated by progradation of siliciclastic sediments across a nearly flat Eocene carbonate ramp (e.g., Poag and Sevon, 1989; Fulthorpe *et al*., 2000). Progradation of Miocene clinoforms delivered sand-rich sediments to the shelf and slope. In the Miocene, depocenters migrated to the southwest, which created a complex, three-dimensional clinoform geometry where sediments thin and fine away from the depocenters (Poulsen *et al*., 1998). As the Miocene clinoforms migrated to the south, their surface gradients varied. Clinoform surfaces had ~3° slopes at 13.6 Ma, increased to >6° by 11 Ma, and decreased to approximately 5° by 8 Ma (Fulthorpe and Austin, 1998). Clinoforms surfaces were steepest near the depocenter and their slopes decreased with distance from the depocenters (Poulsen *et al*., 1998).

In the Pleistocene, the Hudson river system became the dominant sediment source in this region and the depocenter migrated north of the Miocene depocenters (Fulthorpe and Austin, 1998). This shift in sediment source included a fining of the sediments. Pleistocene sediments covered the Miocene strata, thinning downslope and to the southwest (Figures 4.3-4.5). Pleistocene deposition created the modern continental slope with an average gradient of 3° (Figure 4.1) (McAdoo *et al*., 2000). Sea floor mapping of this region shows a

slope that is dominantly covered by Pleistocene sediments with outcrops of Cretaceous, Eocene, Oligocene, and Miocene existing in some of the slope canyons (Figure 4.2) (Hampson and Robb, 1984).

4.2.2 ODP Borehole Data

Ocean Drilling Program (ODP) Sites 902-904 and 1073 (Figure 4.1) provide lithologic, stratigraphic, and age data along the US mid-Atlantic continental slope (Figures 4.6-4.9). ODP Sites 902-904 document downslope thinning of Pleistocene sediments from 350m at ODP Site 903 to 100m at ODP SIte 904 (Figures 4.7-4.9). In this region, Pleistocene sediments are underlain by a thicker Miocene layer that also thins downslope (Figures 4.7-4.9). In contrast, ODP Site 1073 has >500m of Pleistocene sediments that are underlain by thin layers of Oligocene, Miocene, and Pliocene sediments (Figure 4.6). Across the margin, silt is the dominant Pliocene-Pleistocene lithology whereas the Miocene and Oligocene sediments are composed of silt and sand with glauconite (Mountain *et al*., 1994; Shipboard Scientific Party, 1998).
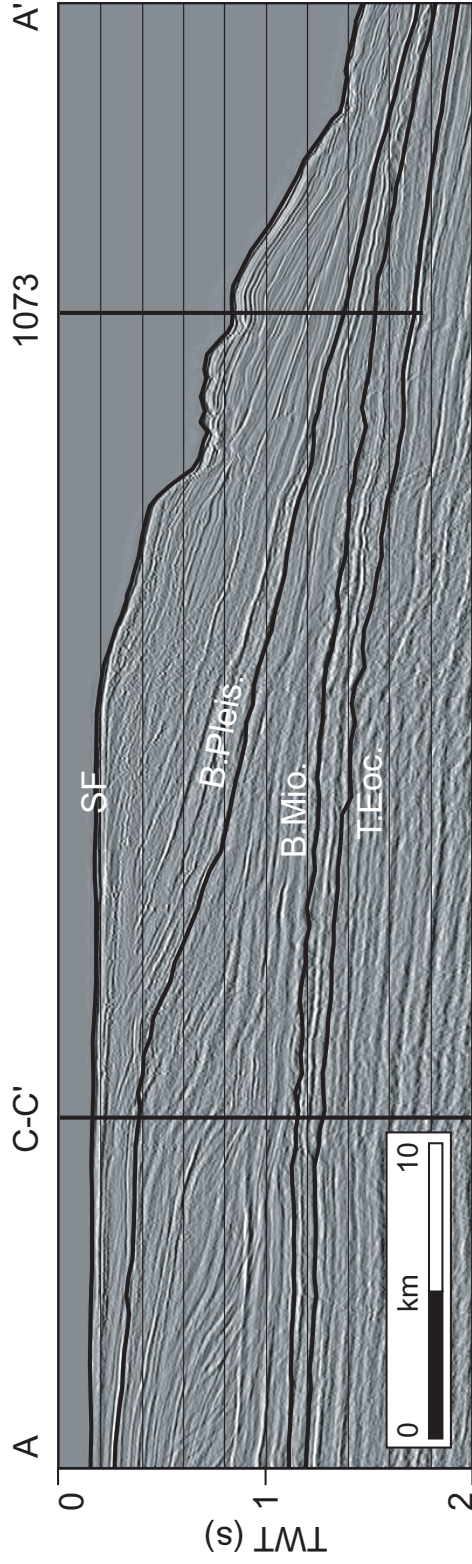
Figure 4.3: Seismic cross-sections A-A' (Ew9009 Line 1002, Mountain *et al.*, 1994) that is located in Figure 4.1. The seafloor (SF), the base of the Pleistocene section (B.Pleis.), the base of the Miocene section (B.Mio.) and the top of the Eocene section (T.Eoc.) are identified (solid black lines). Data are presented in two-way travel time (TWT). One second of TWT is approximately one km in the sedimentary section.
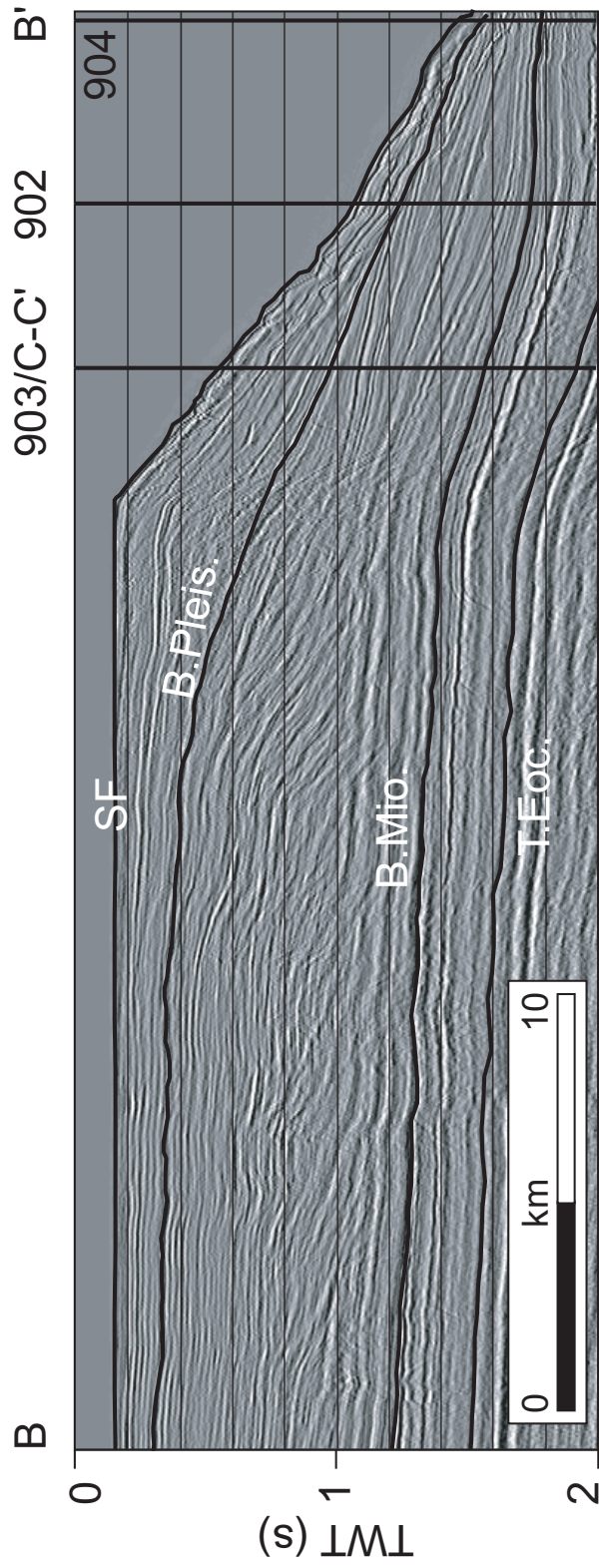
Figure 4.4: Seismic cross-sections B-B' (Ew9009 Line 1005, Mountain *et al.*, 1994) that is located in Figure 4.1. The seafloor (SF), the base of the Pleistocene section (B.Pleis.), the base of the Miocene section (B.Mio.) and the top of the Eocene section (T.Eoc.) are identified (solid black lines). Data are presented in two-way travel time (TWT). One second of TWT is approximately one km in the sedimentary section.
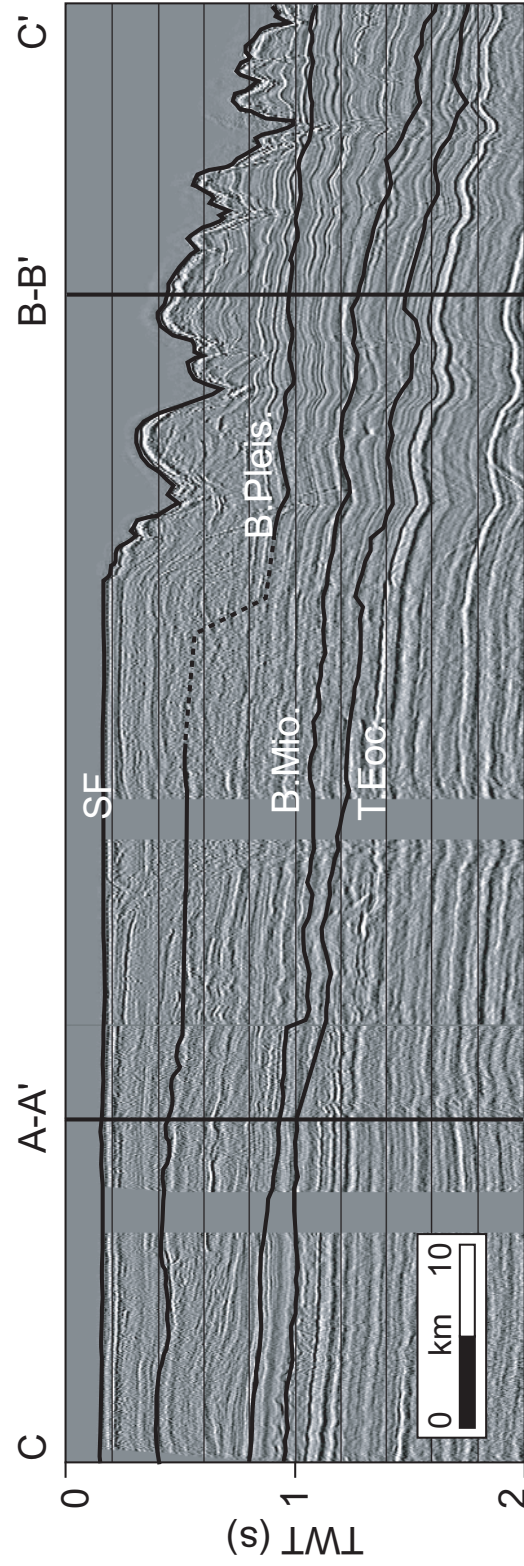
Figure 4.5: Seismic cross-sections A-A' (Ew9009 Line 1002, Mountain *et al.*, 1994) that is located in Figure 4.1. The seafloor (SF), the base of the Pleistocene section (B.Pleis.), the base of the Miocene section (B.Mio.) and the top of the Eocene section (T.Eoc.) are identified (solid black lines). Data are presented in two-way travel time (TWT). One second of TWT is approximately one km in the sedimentary section.

ODP Site 1073 recovered Eocene through Pleistocene silt and clay (Figure 4.6). Interpretation of the wireline gamma ray log is relatively homogeneous lithology without any divergences from the general baseline. This is consistent with the grain size observations which indicate silt and clay dominate the sedimentary section (Shipboard Scientific Party, 1998). Wireline bulk density is <2.1 g/cm^3 but highly variable in the Pleistocene section. At the top of the Pliocene section bulk density shifts to 1.7 g/cm^3 and then shows a slight decrease at the top of the Miocene followed by a gradual increase to the base of the site. Wireline velocity increases with depth within the Pleistocene section, but velocity decreases at the top of the Pliocene section. Velocity then increases within the Pliocene and Miocene sediments. Seismic interval velocity from the projection of ODP Site 1073 on Line 1002 (Figures 4.3, 4.6) match the wireline velocities in the Pleistocene section but exceed wireline velocity in the Pliocene-Miocene section. Porosity, as measured on core samples (Shipboard Scientific Party, 1998), decreases from 62% at the seafloor to 45% by 100 metres below sea floor (mbsf). Porosity ranges from 45-50% from 100-550 mbsf and then increases to >60%. Porewater Cl$^-$ and Sr^{2+} at ODP Site 1073 have near-sea water concentrations through the Pleistocene and increase within the deeper, older sediments (Figure 4.6). These chemical profiles are indicative of a system that is diffusion-dominated with little vertical advection (Dugan and Flemings, 2000). Sedimentation rates were highest in the Pleistocene (0.4 to 1.1 mm/yr) which is ten times greater than the Oligocene-Pliocene sedimentation rates.
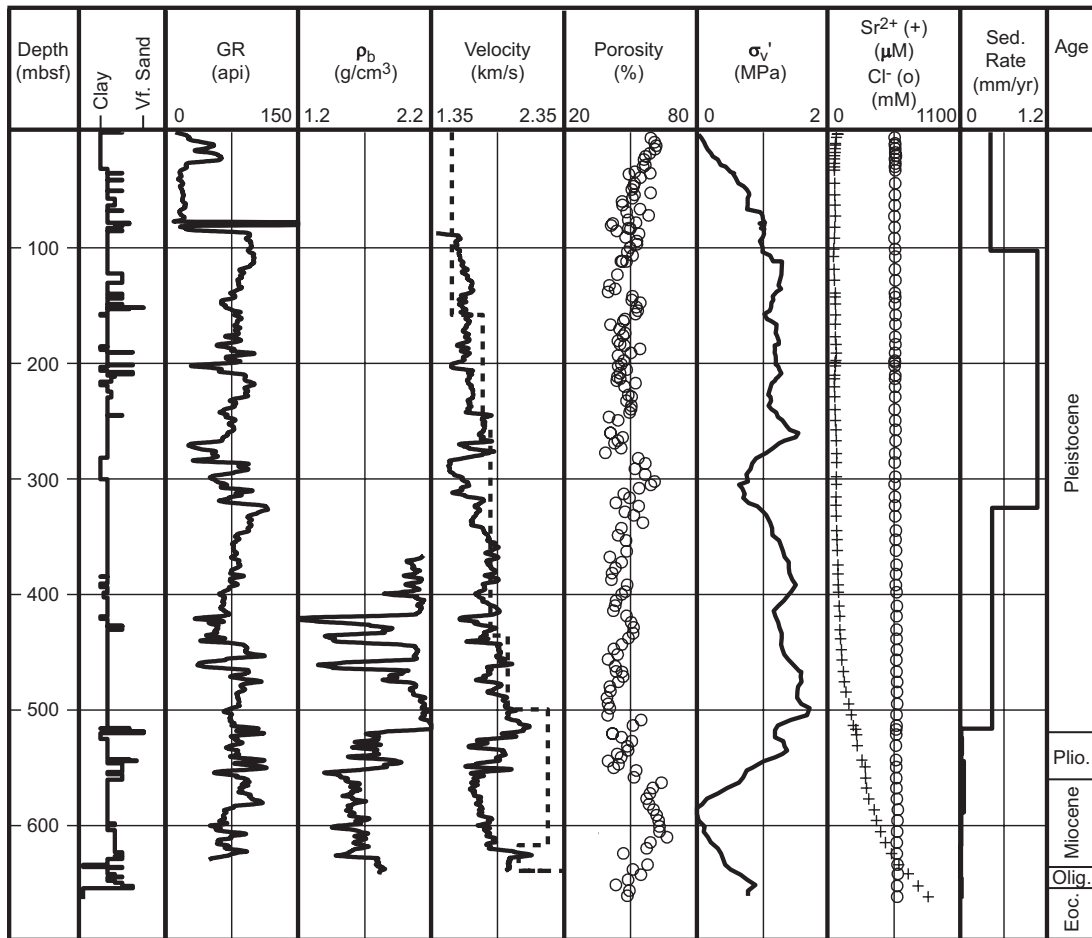
Figure 4.6: Core and log data for ODP Site 1073 defining the lithology, density, velocity, porosity, pore-water chemistry, and sedimentation rates. Solid velocity line is wireline velocity and dashed velocity line is interval velocity at projection of ODP Site 1073 on seismic line A-A' (Figure 4.3). Vertical effective stress is estimated from porosity-stress model (Equation 4.2).

ODP Site 903 has an increase in grain size relative to ODP Site 1073 with increasing silt and very fine sand percentages (Figure 4.7). Wireline bulk density at this site is less than 2.2 g/cm^3 in the Pleistocene with lower density near 200 and 300 mbsf. Within the Pliocene and Miocene sediments, bulk density decreases with depth. Wireline and seismic interval velocity increase with depth through the Pleistocene and Pliocene but decreases with the Miocene to 800 mbsf (Figure 4.7). The velocity profile correlates to the core-measured porosity which decreases as velocity increases. In the Miocene sediments, the wireline velocity decreases as porosity increases. The Cl$^-$ and Sr^{2+} profiles have approximately sea water values in the Pleistocene and then increase with depth throughout the Miocene and Oligocene sediments. Sedimentation rates ranged from 0.4 to 1.2 mm/yr with in the Pleistocene and part of the Pliocene, which greatly exceeded the sedimentation rates for the Eocene through Miocene. (Figure 4.7)

ODP Site 902, located downslope from ODP Site 903 (Figure 4.1), has less very-fine sand and increase silt content (Figure 4.8). A major lithology change is noted from core observations and the gamma ray signature between the Eocene sediments and the overlying Oligocene-Pleistocene sediments. Bulk density is less than 2.0 g/cm^3 throughout the entire logged section and has a downhole-increasing trend with the highest density occurring in the Eocene sediments. The low bulk density of the Miocene-Pleistocene sediments corresponds to wireline velocity that is less than 1.85 km/s (Figure 4.8). The Eocene-Miocene section below 600 mbsf has the highest gamma ray values, bulk density, and has velocity >1.85 km/s. Core-measured porosity at ODP Site 902 is consistently less than 50% and

increases from the seafloor to 500 mbsf. An abrupt porosity decrease occurs at observed at 600 mbsf; this corresponds to increases in bulk density, velocity, and the gamma ray log. Similar to ODP Site 903, near-sea water Cl^- and Sr^{2+} concentration exist in the Pleistocene section, but they increase in the Miocene sediments. Below 600 mbsf, Cl^- and Sr^{2+} decrease to near-zero. Sedimentation rates at ODP Site 902 are greatest in the Pleistocene, but lower than those at upper slope ODP Site 903. In the early Miocene, sedimentation rates were low, but they increased with time (Figure 4.8). This may reflect the southward migration of Miocene depocenters (Fulthorpe and Austin, 1998; Poulsen *et al*., 1998).

ODP Site 904 is homogeneous silty clay in the Pleistocene section and has increasing median grain size with depth though the Miocene and Oligocene sediments (Figure 4.9). In the Eocene section, gamma ray measurements and grain size decrease. Bulk density and wireline velocity are nearly constant in the Miocene section and increase in the Oligocene and Eocene section. Measured porosity decreases from the sea floor to 100 mbsf and then increases to >60% for the Miocene and Oligocene sections (Figure 4.9). The Eocene sediments have high porosity at shallow depth below sea floor and then decrease with increasing depth. Porewater Cl^- and Sr^{2+} concentrations increase with depth in the Miocene and older sediments. ODP Site 904 has lower Pleistocene sedimentation rates than upper-slope ODP Sites 902-903. Miocene and Oligocene sedimentation rates are low, similar to the upper slope sites.
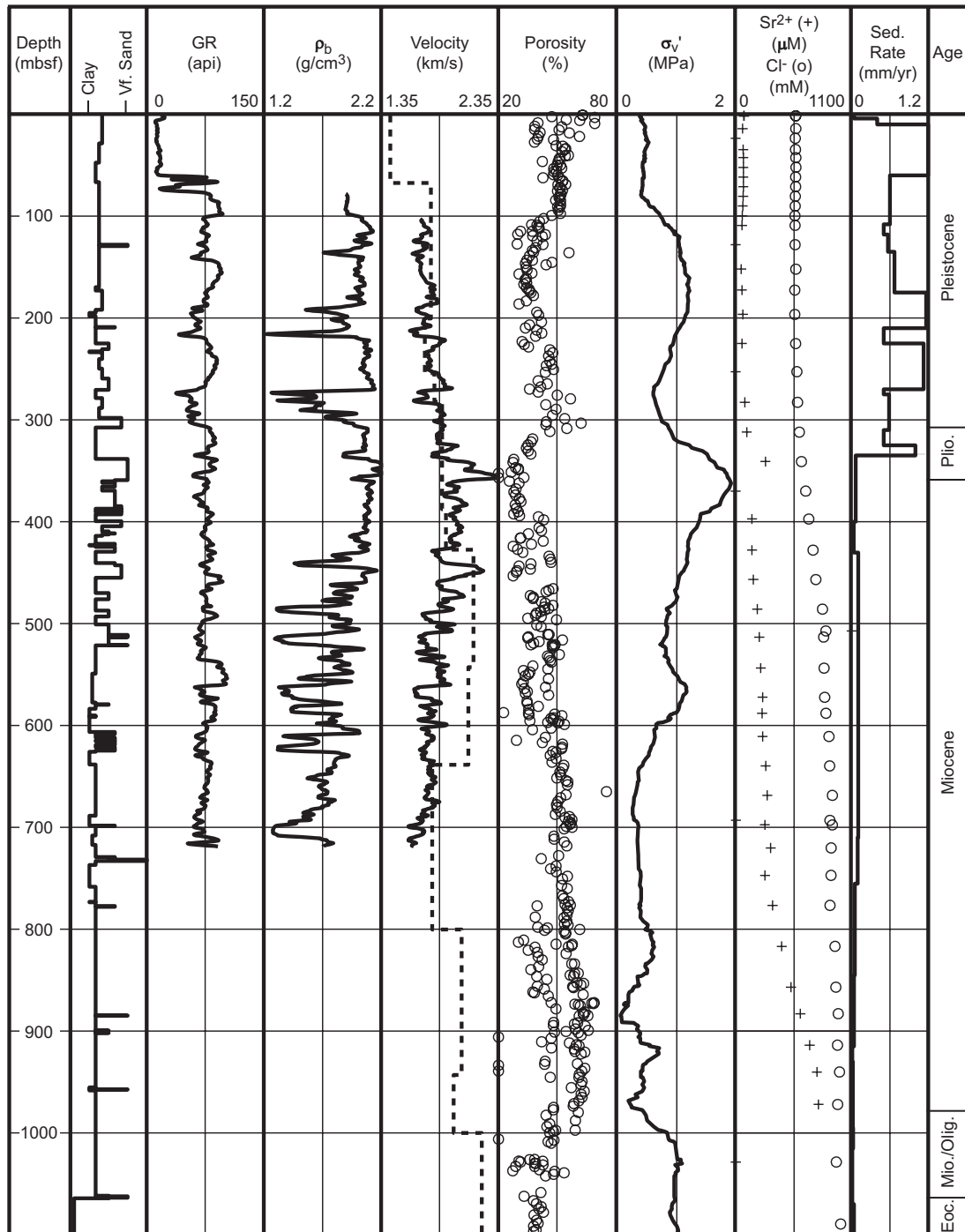
Figure 4.7: Core and log data for ODP Site 903 defining the lithology, density, velocity, porosity, pore-water chemistry, and sedimentation rates. Solid velocity line is wireline velocity and dashed velocity line is interval velocity at projection of ODP Site 903 on seismic line B-B' (Figure 4.4). Vertical effective stress is estimated from porosity-stress model (Equation 4.2).
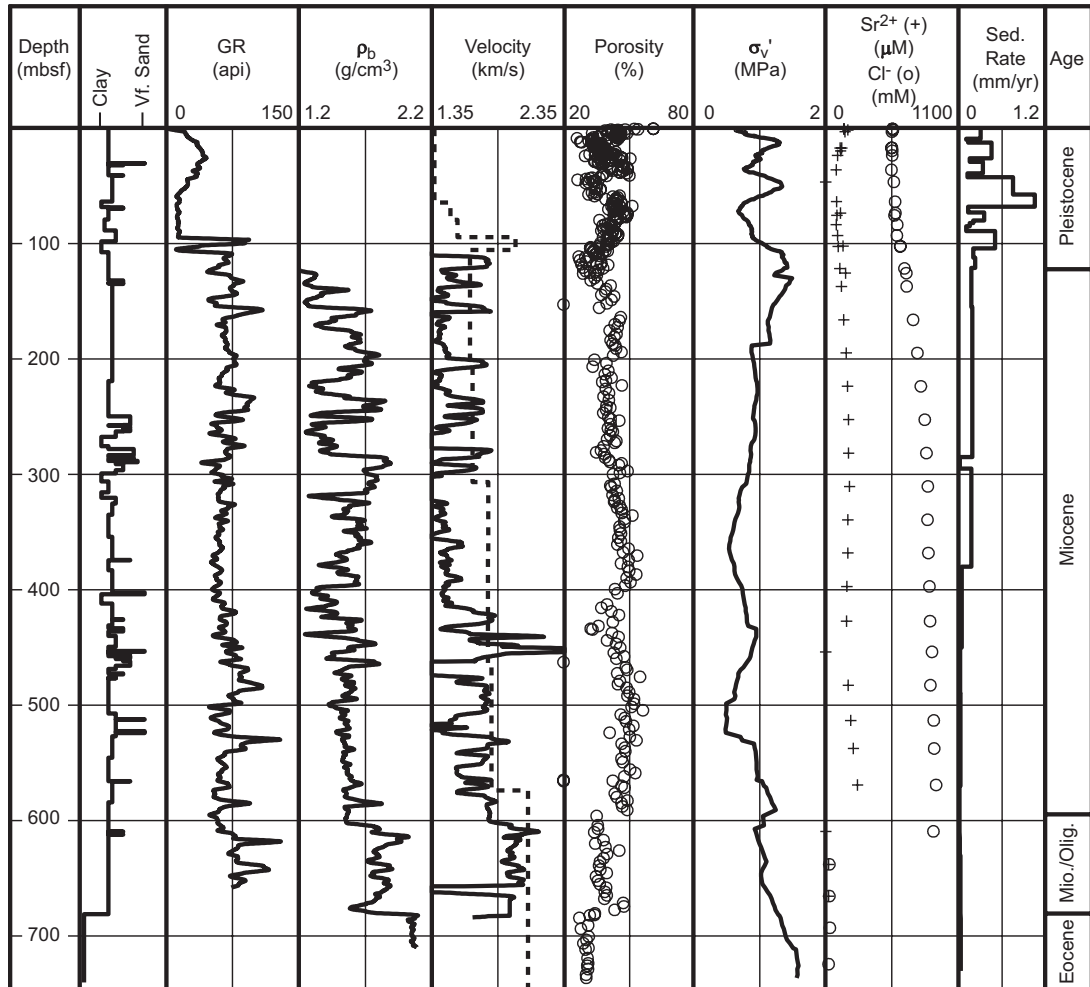
Figure 4.8: Core and log data for ODP Site 902 defining the lithology, density, velocity, porosity, pore-water chemistry, and sedimentation rates. Solid velocity line is wireline velocity and dashed velocity line is interval velocity at projection of ODP Site 902 on seismic line B-B' (Figure 4.4). Vertical effective stress is estimated from porosity-stress model (Equation 4.2).
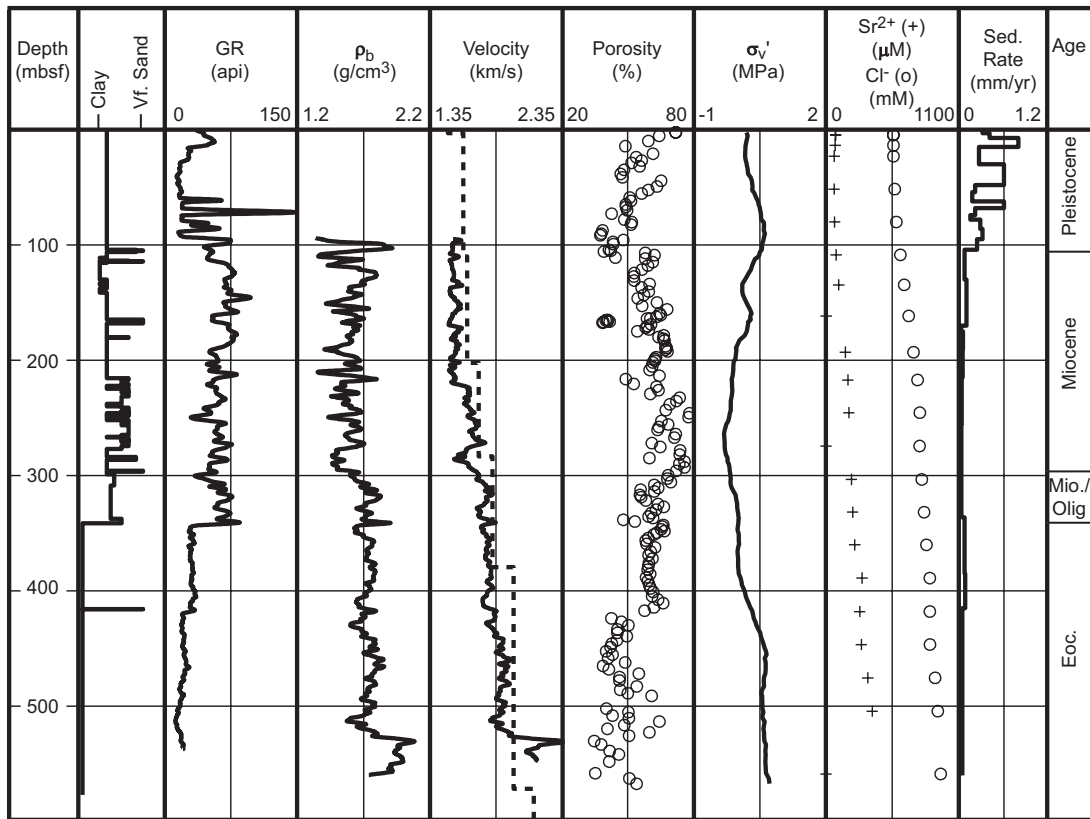
Figure 4.9: Core and log data for ODP Site 904 defining the lithology, density, velocity, porosity, pore-water chemistry, and sedimentation rates. Solid velocity line is wireline velocity and dashed velocity line is interval velocity at projection of ODP Site 904 on seismic line B-B' (Figure 4.4). Vertical effective stress is estimated from porosity-stress model (Equation 4.2).

4.2.3 Seismic Data

Two-dimensional, multi-channel seismic Lines 1002, 1005, and 1025/6 (Figures 4.1, 4.3-4.5) (Mountain *et al.*, 1994) were processed to evaluate the interval velocity of the Oligocene through Pleistocene sediments (Table 4.1). Seismic stacking (RMS) velocities were picked along stratigraphic horizons using an iterative process until horizon depths and velocities were unchanged. RMS velocities (v_{rms}) were converted to interval velocity (v_i) following the approach of Dix (1955) (Equation 4.1). Variables are defined in Table 4.2

$$v_{i_n}^2 = \frac{(v_{rms}^2 t)_n - (v_{rms}^2 t)_{n-1}}{t_n - t_{n-1}} \qquad . \qquad\qquad (4.1)$$

4.3 Pressure and Stress

Effective stress and pressure models were constrained from porosity observations at ODP Site 1073. These relations were used to calibrate a velocity-effective stress for the slope sediments. Porosity is related to the maximum state of stress to which the sample has been exposed (e.g., Casagrande, 1936; Terzaghi, 1943). Seismic interval velocity can also be associated with porosity or effective stress (e.g., Bangs *et al.*, 1990; Bowers, 1994; Dutta, 2002). The conceptual framework for the velocity model-stress model is that sediments with a low interval velocity have high porosity and low effective stress; in contrast, high-velocity sediments are more consolidated and have high effective stress.

Table 4.1: Seismic data processing

Seismic Process	Function
CMP gather	create full fold; increase signal-to-noise ratio
Amplitude gain	increase amplitude for velocity analyses
Bandpass filter	limit frequency range of data
Velocity analysis	pick velocity on seismic horizons
Multiple removal	use velocity data to remove seafloor multiples
Velocity analysis	re-pick velocity on seismic horizons
Bandpass filter	limit frequency range of data
NMO correction	convert all traces to zero offset
CMP stack	stack all traces at each CDP

Table 4.2: Nomenclature

Variable	Definition	Dimensions
A	effective stress-depth model constant	dimensionless
B	effective stress-depth model constant	dimensionless
C	effective stress-velocity model constant	dimensionless
D	effective stress-velocity model constant	dimensionless
g	acceleration due to gravity	L/T^2
n	index counter	integer
P*	overpressure	M/LT^2
t	time	T
v_i	interval velocity	L/T
z_{bsf}	depth below sea floor	L
β	bulk compressibility	LT^2/M
β_f	fluid compressibility	LT^2/M
ϕ	porosity	dimensionless
ϕ_o	initial porosity	dimensionless
ρ_w	water density	M/L^3
σ_v	overburden stress	M/LT^2
σ_{vbsf}	overburden stress below sea floor	M/LT^2
σ_v'	effective vertical stress	M/LT^2
σ_{vh}'	hydrostatic effective stress	M/LT^2

4.3.1 Borehole Interpretations

Porosity can be related to vertical effective stress through an exponential porosity-stress relationship (e.g., Rubey and Hubbert, 1959; Hart *et al*., 1995) (Equation 4.2),

$$\phi = \phi_o e^{-\beta\sigma_v'} \qquad .\tag{4.2}$$

ϕ_o is the reference porosity, β is the bulk compressibility, and σ_v' is the vertical effective stress ($\sigma_v' = \sigma_v - \rho_w gz - P^*$). All variables are defined in Table 4.2. ϕ_o (0.61) and β (0.44 MPa^{-1}) were constrained from 0-80 mbsf at ODP Site 1073 assuming hydrostatic fluid pressures ($P^* = 0$) (Dugan and Flemings, 2000). Bulk density measurements were integrated to define the overburden stress (σ_v) at ODP Site 1073 (Figure 4.6). We used these data to evaluate stress as a function of depth below sea floor (Equation 4.3) in the shallow subsurface of the US mid-Atlantic slope.

$$\sigma_{v_{bsf}} = A z_{bsf}^{B} \qquad .\tag{4.3}$$

z_{bsf} is the depth below sea floor. A equal to 0.015 and B equal to 1.03 are based on the observations at ODP Site 1073. A, B, and z_{bsf} in meters provide vertical stress below sea floor (σ_{vbsf}) in MPa (Equation 4.3).

From porosity at ODP Site 1073, we interpret effective stress less than 1 MPa for the

entire sedimentary section (Equation 4.2; Figure 4.6). In the high porosity Miocene and

Oligocene sediments, estimates of effective stress approach zero.

Porosity at ODP Sites 902-904 and the constants constrained at ODP Site 1073 were used

to evaluate how stress changes downslope in a region with submarine canyons. Effective

stress was estimated at ODP Sites 902-904 (Equation 4.2; Figures 4.7-4.9). These bore-

hole predictions were used to construct a downslope stress profile (Figure 4.10). The

downslope profile through ODP Site 903, 902, and 904 has effective stress <2 MPa. Effec-

tive stress increases with depth in the Pleistocene sediments. Stress decreases are esti-

mated within the Miocene sediments where porosity increases (Figures 4.7-4.9). Stress

also decreases moving downslope; ODP Site 904 has the lowest predicted stresses.
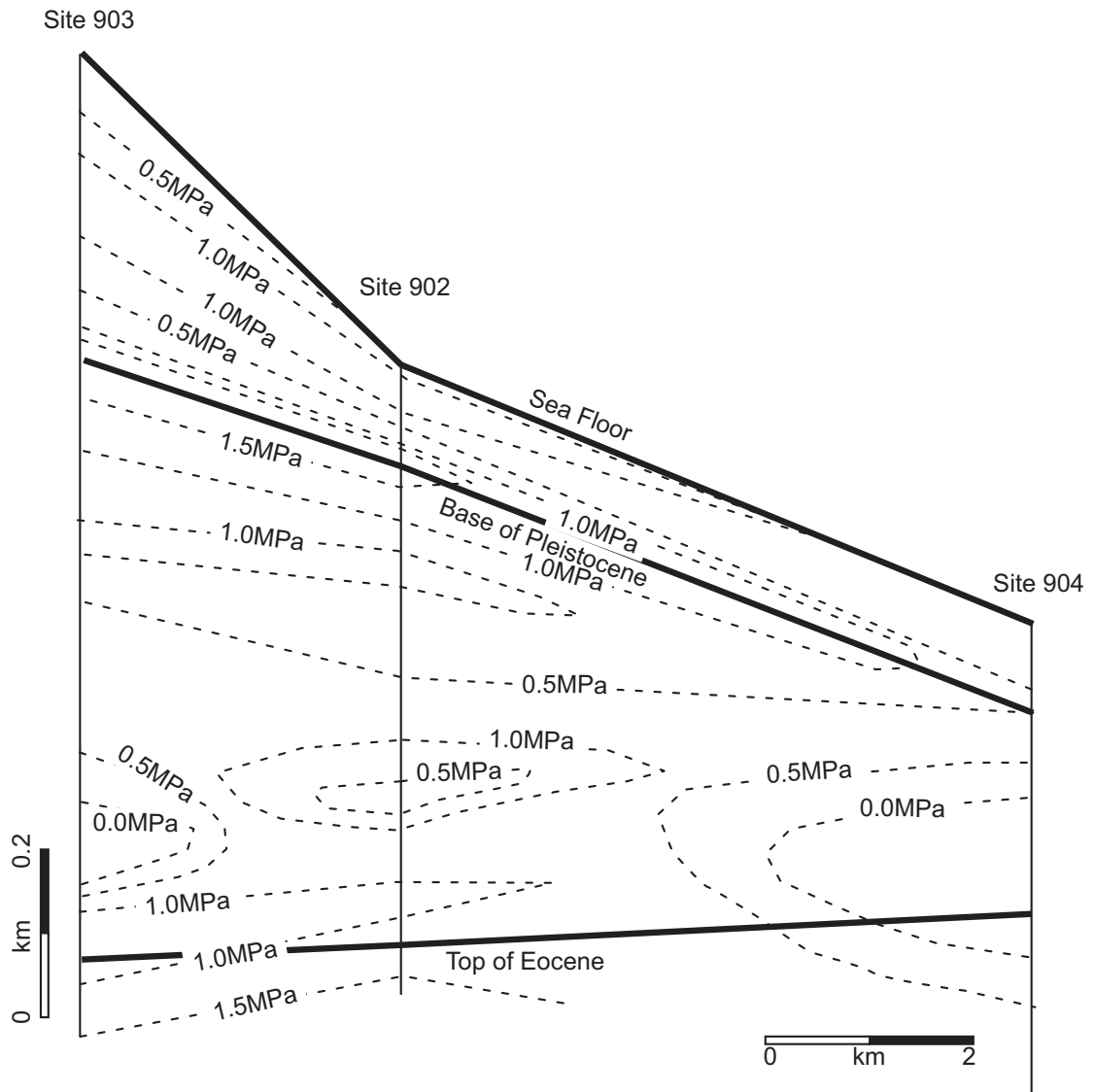
Figure 4.10: Effective stress profile interpreted between ODP Sites 903, 902, and 904 (located in Figure 4.1). Effective stress at each site was inverted from porosity (Figures 4.7-4.9) using Equation 4.2 assuming $\phi_o = 0.61$ and $\beta = 0.44$ MPa^{-1} as determined from 0-80 mbsf at ODP Site 1073 (Dugan and Flemings, 2000). The well profiles were used to constrain the contours (dashed lines). Contour interval is 0.5 MPa.

4.3.2 Seismic Interpretation

A vertical effective stress-interval velocity model (Equation 4.4) (e.g., Bowers, 1994) was calibrated at ODP Site 1073 using the effective stresses interpreted from porosity data and the seismic interval velocity on Line 1002 at the projected intersection of ODP Site 1073 (Figure 4.6);

$$v_i = C\sigma_v'^D + 1524 \tag{4.4}$$

C (379) and D (0.425) are empirical constants, interval velocity is in m/s, and vertical effective stress is in MPa (Table 4.2).

Seismic interval velocities along Ewing 9009 Line 1002 (A-A' located Figure 4.1) increase from 1500 m/s at the sea floor to 2000 m/s in the Pleistocene section (Figure 4.11A). Near the seafloor, velocity increases with depth at a constant gradient. The velocity gradient is lower where Pleistocene sediments are thickest. Effective stresses based on these interval velocities (Equation 4.4) are low in the shallow Pleistocene section and increase with depth below the sea floor (Figure 4.11B). An effective stress decrease with depth is predicted at the base of the Pleistocene section beneath the modern shelf-slope break. Overpressure ($P^* = \sigma_v - \sigma_v' - \rho_w gz$) can be estimated along the seismic section by comparing the vertical effective stress, the overburden stress and the depth below sea level (Figure 4.11C). Interval velocity-predicted overpressure increases rapidly from the base of the Miocene section to the top of the Eocene section.
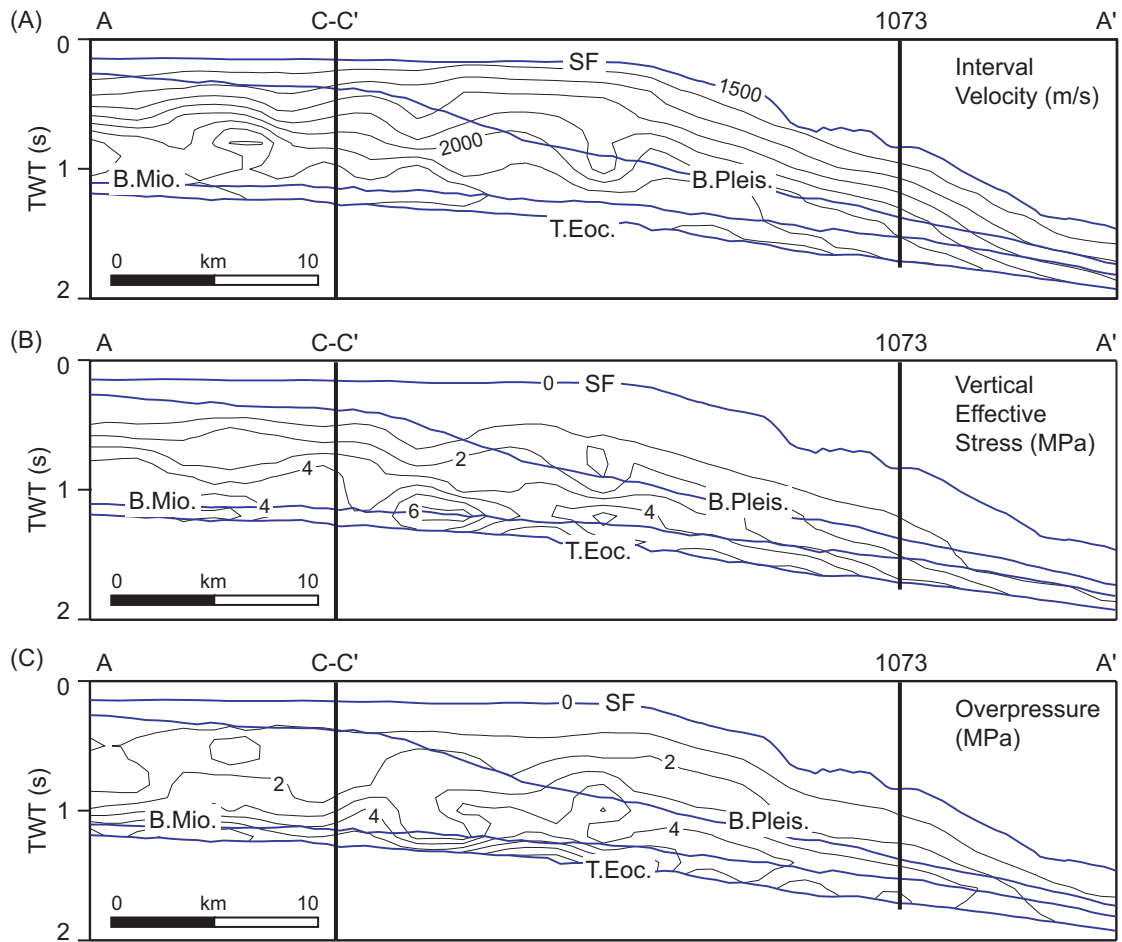
Figure 4.11: (A) Interval velocity, (B) vertical effective stress, and (C) overpressure profiles for seismic line A-A' (Figures 4.1, 4.3). Interval velocity contour interval is 100 m/s. Vertical effective stress and overpressure contour intervals are 1 MPa. Data are presented in two-way travel time (TWT). Seafloor (SF), base of Pleistocene (B.Pleis.), base of Miocene (B.Mio.) and top of Eocene (T.Eoc.) surfaces are labelled for reference.

Interval velocity along Ew9009 Line 1005 (B-B' in Figures 4.1, 4.12A) increases down-

ward with a constant gradient in the Pleistocene sediments, increases at a steeper gradient

in the middle of the Miocene sediments, and then increases at a slower rate in the deeper

Miocene and Oligocene sediments (Figure 4.12A). Within the Pleistocene sediments a

maximum velocity of 1900 m/s occurs beneath the shelf-slope break. Velocity increases to

2500 m/s in the Oligocene-Miocene sediments.

Effective stress estimated from interval velocity (Equation 4.4) increases with depth along

Line 1005 (Figure 4.12B). Effective stress along is less than 1 MPa throughout the Pleis-

tocene sediments; within the Miocene sediments, however, effective stress increases to >8

MPa. The total stress and effective stress prediction yield overpressure estimates along

Line 1005 (Figure 4.12C) that increases with depth to the 2 MPa contour. Beneath the

shelf-slope break a decreased overpressure gradient is present from 2.0 to 2.5 MPa and

then overpressure increases rapidly. A maximum overpressure of 5 MPa exists in the

Miocene sediments just seaward of the shelf-slope break (Figure 4.12C). This high over-

pressure zone has a high pressure gradient and corresponds to a pull-down in the velocity

contours (Figure 4.12A).
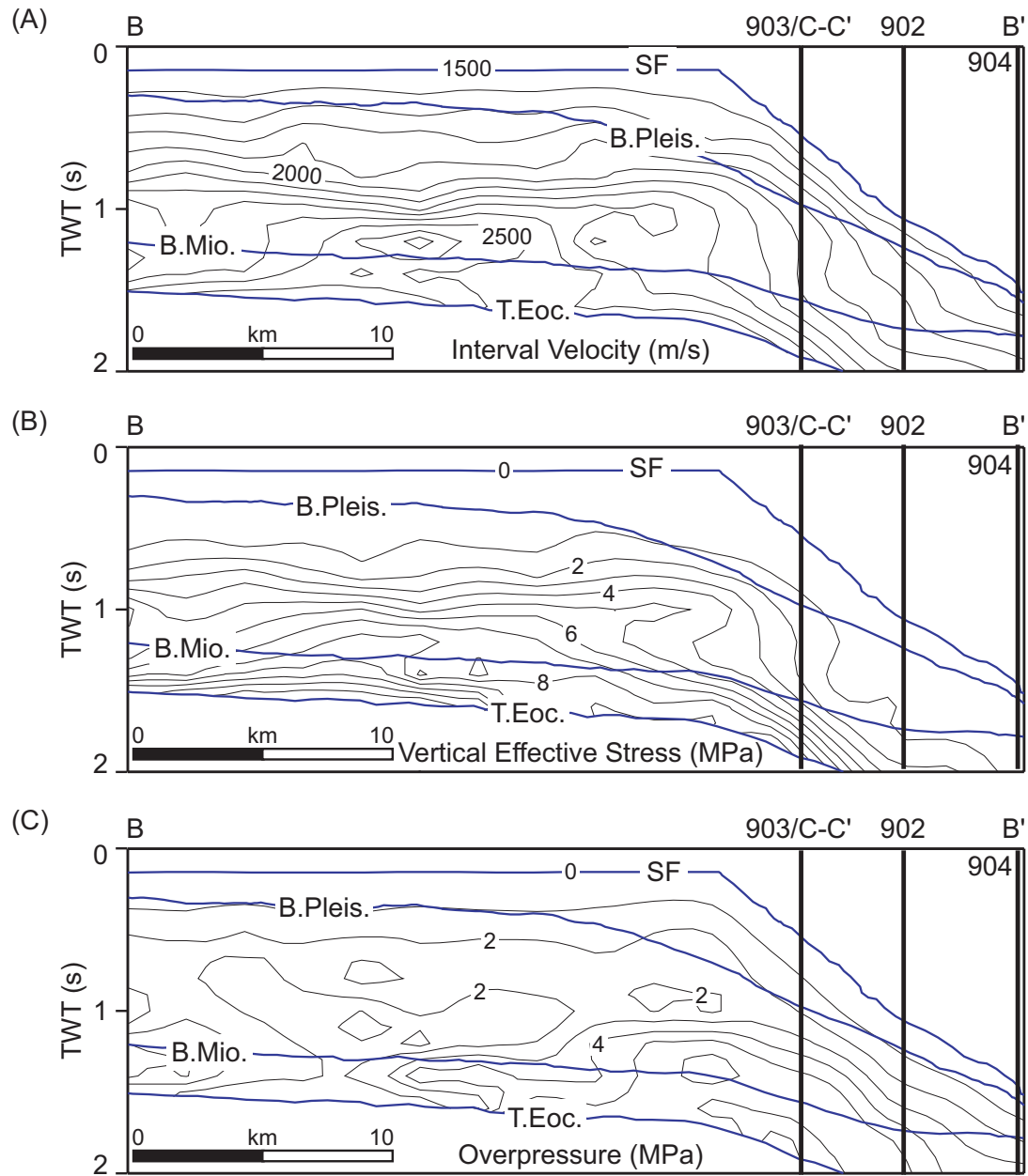
Figure 4.12: (A) Interval velocity, (B) vertical effective stress, and (C) overpressure profiles for seismic line B-B' (Figures 4.1, 4.4). Interval velocity contour interval is 100 m/s. Vertical effective stress and overpressure contour intervals are 1 MPa. Data are presented in two-way travel time (TWT). Seafloor (SF), base of Pleistocene (B.Pleis.), base of Miocene (B.Mio.) and top of Eocene (T.Eoc.) surfaces are labelled for reference.

Seismic section C-C' (Figures 4.1-4.2, 4.13) is composed of portions of Ew9009 Lines

1025 and 1026. The section provides an image of the shelf and slope from the Hudson

Apron to the canyons southwest of the apron. Interval velocity for section C-C' parallels

the seafloor in the Pleistocene sediments and increases at a constant gradient (Figure

4.13A). Velocity increases slowly in the deeper Miocene sediments to a maximum of 2200

m/s. Vertical effective stress estimates (Equation 4.4) are <1 MPa for most of the Pleis-

tocene section (Figure 4.13B). Vertical effective stress increases with depth beneath the

continental shelf but a decrease with depth is predicted beneath the thickest Pleistocene

accumulations. Maximum effective stresses occur at the base of the interpreted section

beneath the modern continental shelf. The interpreted overpressure profile (Figure 4.13C)

differs beneath the continental shelf and slope. Overpressure along the shelf increases

slowly with depth, reaching a maximum overpressure of 4 MPa beneath the shelf-slope

break. Along the slope, overpressure increases to greater than 6 MPa. Beneath the slope,

overpressure parallels the sea floor with pressure contours even where canyons are

encountered (Figure 4.13C).
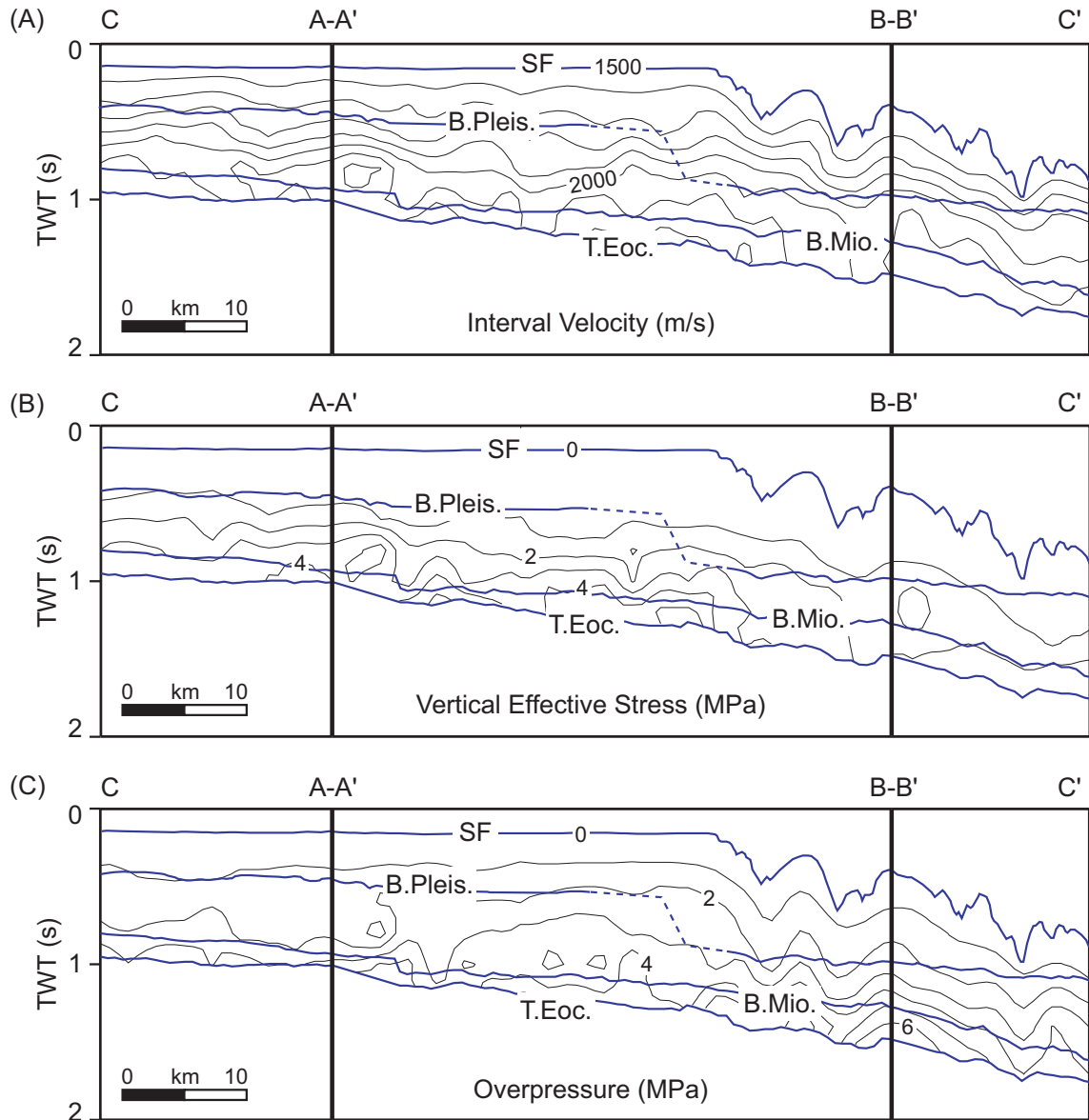
Figure 4.13: (A) Interval velocity, (B) vertical effective stress, and (C) overpressure profiles for seismic line C-C' (Figures 4.1, 4.5). Interval velocity contour interval is 100 m/s. Vertical effective stress and overpressure contour intervals are 1 MPa. Data are presented in two-way travel time (TWT). Seafloor (SF), base of Pleistocene (B.Pleis.), base of Miocene (B.Mio.) and top of Eocene (T.Eoc.) surfaces are labelled for reference.

4.4 Discussion

Core and seismic data analyses are used to characterize stratigraphy, pressure, and stress across the US mid-Atlantic continental margin. From this we interpret the processes that contribute to the hydrodynamics of this slope. High Pleistocene sedimentation was dominated by silt and clay and this precludes fluid drainage which creates low effective stress and overpressure (e.g. Gibson, 1958). In the Pleistocene sedimentary section, this is recorded by high porosity and low velocities (Figures 4.6-4.9, 4.11-4.13). Maximum overpressures are interpreted where Pleistocene accumulations are thickest. This overpressure drives fluids along permeable beds, which increases overpressure and decreases effective stress on the middle and lower slope where Pleistocene overburden is thin (Figure 4.14) (Dugan and Flemings, 2000). In locations where overpressure is decreased by fluid discharge, effective stress increases and the forces resisting slope failure increase (Lambe and Whitman, 1979; Loseth, 1998; Dugan and Flemings, 2002). Seismic cross-sections A-A' and B-B' have effective stress pull-downs at the lower slope where the Miocene sediments are thinnest (Figures 4.11, 4.12), which is similar to the simulation results for sedimentation and fluid flow along this margin (Figure 4.14). The porosity analysis also predicts an effective stress minimum at ODP Site 904 in the coarse-grained, glauconitic sand where Pleistocene overburden is thin (Figures 4.9-4.10). Two sandy, glauconitic layers are identified in the Miocene section through ODP Site 903, 902, and 904 (Figure 4.15). These sandy layers may be a flow conduits that focus fluids to the lower slope (e.g, Figure 4.14), decrease stress on the lower slope (e.g., Figure 4.10-4.13) and potentially contributed to slope failures in this region of the US mid-Atlantic slope (Figure 4.2).
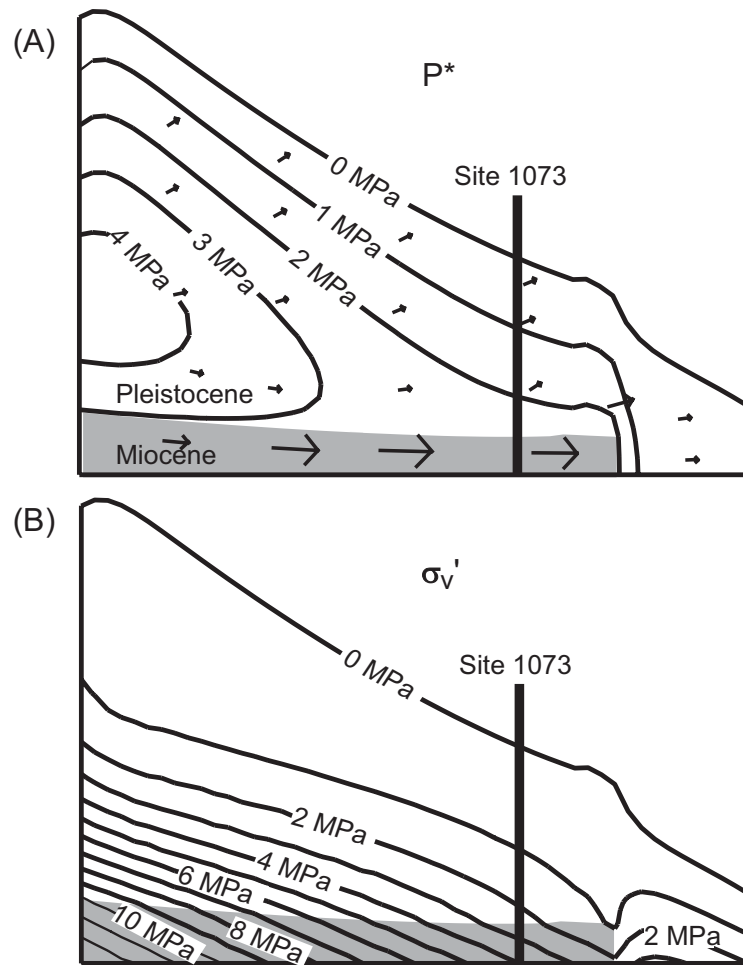
Figure 4.14: Simulated (A) overpressure and (B) effective stress for the modern New Jersey slope. Model is described and explained in Dugan and Flemings (2000; 2002). Arrows indicate relative flow velocities and emphasize the role of flow focussing in increasing overpressure and decreasing stress on the lower slope. Note vertical exaggeration.
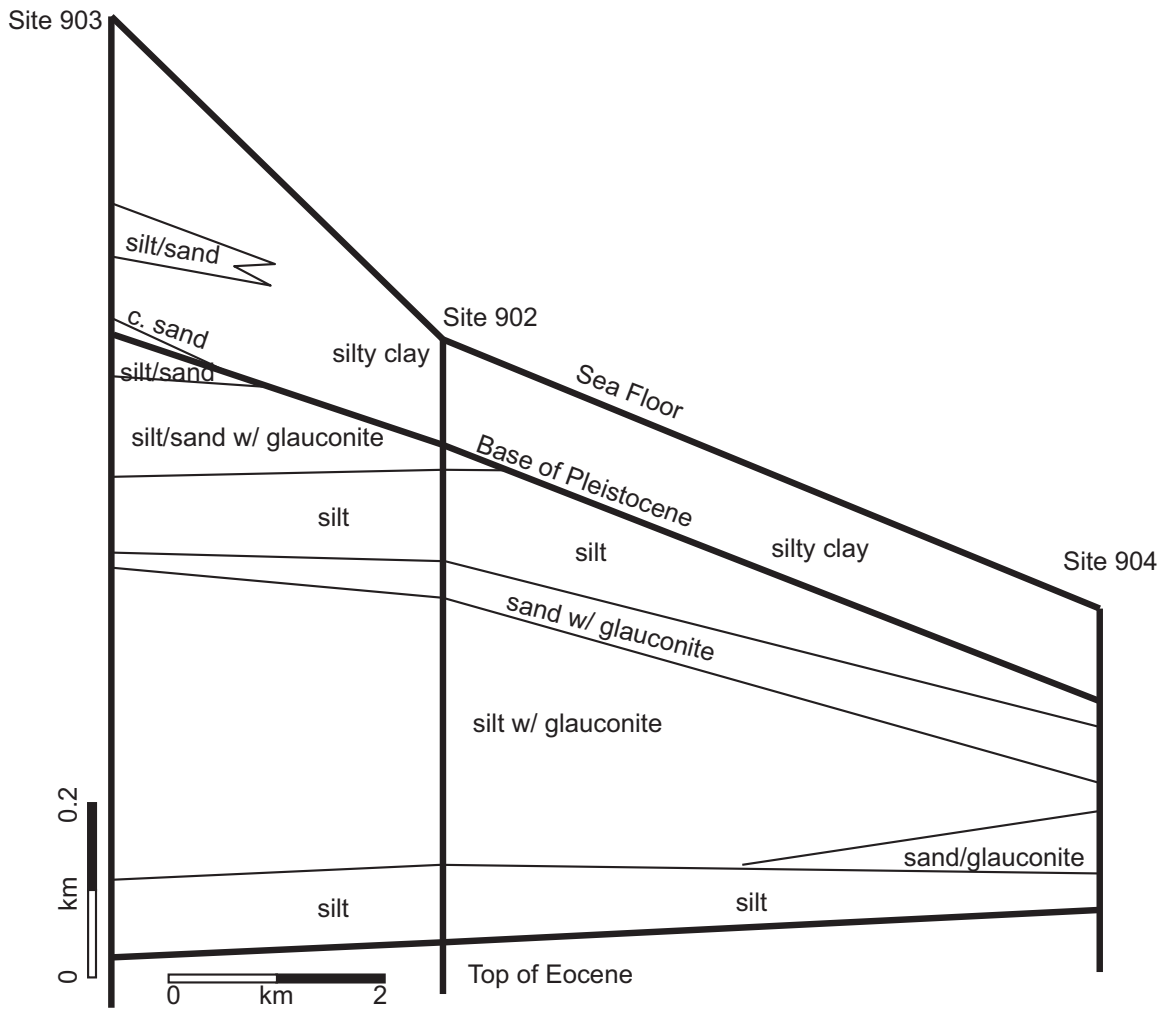
Figure 4.15: Simplified lithologic cross-section through ODP Sites 903, 902, and 904 (located in Figure 4.1) based on shipboard lithologic interpretations (Figures 4.7-4.9) (Mountain *et al.*, 1994). Note presence of isolated sandy units within the Miocene section. These may be conduits for flow focussing as simulated in Figure 4.14.

Effective stress estimates from interval velocity of seismic sections A-A', B-B', and C-C'

indicate that the modern slope is dominated by positive effective stress, therefore the mar-

gin is at stable conditions from an infinite slope analysis. Failure, as evident in the form of

slope canyons, however, was active during the evolution of the margin (Figure 4.2). Pulses

of high sediment influx during the Pleistocene contributed to pressure generation and

slope failure (Dugan and Flemings, 2000; Dugan and Flemings, 2002). Dugan and Flem-

ings (2002) describe how failure events are tied to periods when sedimentation rates are

highest. Some shelf Miocene sediments in near the canyons were also deposited rapidly

(Mountain *et al*., 1994) and have alternating layers of silt, silty glauconite, and sandy glau-

conite (Figure 4.15). The porous and permeable lenses coupled with Miocene through

Pleistocene deposition may have focussed fluids, produced unstable conditions, and initi-

ated failure on the slope. Dugan and Flemings (2002) presented a sensitivity analysis of

the sedimentation-flow conditions for this margin and described how different permeabil-

ity and loading conditions influence failure. Local sea floor gradient variations also influ-

enced the stability of the margin. Failures probability increases as the sea floor gradient

increases as defined by the infinite slope analysis (e.g. Lambe and Whitman, 1979; Loseth,

1998). The steep Miocene clinoform faces in the southwest of the study region where can-

yons are present (Figure 4.2) (Poulsen *et al*., 1998) therefore provide an increased chance

of failure from infinite slope perspective.

Sediment flux to the margin has decreased in the modern environment (e.g., Mountain *et

al*., 1994; Austin *et al*., 1998). This has produced a situation in which overpressure gener-

ation has ceased and allows existing overpressure to dissipate. As the pressures decrease to

hydrostatic, the stability of the margin increases. Overpressure contours beneath canyons parallel the sea floor (e.g. Figure 4.13C). We interpret this to reflect continued drainage of fluids along permeable outcrops in the canyon walls. Discharge of fluids also contributes to grain-scale erosion (Robb, 1990) and maintains fresh exposure surfaces for additional dissipation of excess fluid pressures.

4.5 Conclusions

Core porosity and seismic data analyses provide effective stress and overpressure estimates for the US mid-Atlantic continental slope. Overpressure begins near the sea floor and increases with depth. Regional overpressure varies in magnitude depending on the thickness of Pleistocene sediments and sedimentation rate. Where Miocene and Pleistocene accumulations are thickest, overpressure is highest and effective stress is lowest. The combined Miocene-Pleistocene sedimentation is interpreted drive fluids laterally along the slope and contribute to slope failure. Subsequent headward erosion along the US mid-Atlantic continental slope may have created the rugose morphology that exists along some portions of this slope. In regions where overpressure did not reach a critical value, the slope remains stable, such as the Hudson Apron. Sedimentation rates have decreased in the modern environment so discharge of fluids leads to the dissipation of overpressure and increased stability of the slope.

Acknowledgements

References

Austin, J.A., Jr., Christie-Blick, N., Malone, MJ., *et al*., 1998, Proceedings of the Ocean
Drilling Program, Initial Reports, 174A, College Station, Ocean Drilling Program,
324p.

Bangs, N.L., Westbrook, G.K., Ladd, J.W., and Buhl, P., 1990, Seismic velocities from the
Barbados ridge complex: indicators of high pore fluid pressures in an accretionary
complex, Journal of Geophysical Research, 95, p. 8767-8782.

Bowers, G.L., 1994, Pore pressure estimation from velocity data: Accounting for over-
pressure mechanisms besides undercompaction, Society of Petroleum Engineers, p.
515-529.

Casagrande, A., 1936, The determination of the pre-consolidation load and its practical
significance, *in* Casagrande, A., Rutledge, P.C., and Watson, J.D., eds., Proceedings of
the 1st International Conference on Soil Mechanics and Foundation Engineering, Vol-
ume 3, American Society of Civil Engineers, p. 60-64.

Dix, C.H., 1955, Seismic velocities from surface measurements, Geophysics, v. 20, p. 68-
86.

Dugan, B., and Flemings, P.B., 2000, Overpressure and Fluid Flow in the New Jersey
Continental Slope: Implications for Slope Failure and Cold Seeps, Science, v. 289, p.
288-291.

Dugan, B., and Flemings, P.B., 2002, Fluid flow and stability of the US continental slope
offshore New Jersey from the Pleistocene to the present, Geofluids, v. 2, p. 137-146.

Dugan, B., Olgaard, D.L., Flemings, P.B., and Gooch, M.J., 2002, Data report: Bulk physical properties of sediments from ODP site 1073, *in* Christie-Blick, N., Austin Jr., J.A., and Malone, M.J., eds., Proceedings of the Ocean Drilling Program, Scientific Results, Volume 174A, College Station, Ocean Drilling Program, p. 1-62.

Dutta, N.C., 2002, Geopressure prediction using seismic data: current status and the road ahead, Geophysics, 67, p. 2012-2041.

Fulthorpe, C.S., and Austin Jr., J.A., 1998, Anatomy of rapid margin progradation: three-dimensional geometries of Miocene clinoforms, New Jersey margin, AAPG Bulletin, v. 82, p. 251-273.

Fulthorpe, C.S., Austin Jr., J.A., and Mountain, G.S., 2000, Morphology and distribution of Miocene slope incisions off New Jersey: are they diagnostic of sequence boundaries?, GSA Bulletin, v. 112, p. 817-828.

Gibson, R.E., 1958, The progress of consolidation in a clay layer increasing in thickness with time, Geotechnique, v. 8, p. 171-182.

Hampson, J.C., and Robb, J.M., 1984, A Geologic Map of the Continental Slope off New Jersey, Lindenkohl to Toms Canyon, Boulder, USGS.

Hart, B.S., Flemings, P.B., and Deshpande, A., 1995, Porosity and pressure: role of compaction disequilibrium in the development of geopressures in a Gulf Coast Pleistocene basin, Geology, 23, p. 45-48.

Johnson, D.W., 1939, The Origin of Submarine Canyons: A Critical Review of Hypotheses, New York, Hafner, 126 p.

Lambe, T.W., and Whitman, R.V., 1979, Soil Mechanics: SI Version, New York, John Wiley & Sons, 553 p.

Loseth, T.M., 1998, Submarine Massflow Sedimentation: Computer Modeling and Basin-Fill Stratigraphy, New York, Springer-Verlag, 156 p.

McAdoo, B.G., Pratson, L.F., and Orange, D.L., 2000, Submarine landslide geomorphology, US continental slope, Marine Geology, v. 169, p. 103-136.

Mountain, G.S., Miller, K.G., Blum, P., *et al*., 1994, Proceedings of the Ocean Drilling Program, Initial Reports, 150, College Station, Ocean Drilling Program, 883 p.

Poulsen, C.J., Flemings, P.B., Robinson, R.A.J., and Metzger, J.M., 1998, Three-dimensional stratigraphic evolution of the Miocene Baltimore Canyon region: implications for eustatic interpretations and the systems tract model, GSA Bulletin, v. 110, p. 1105-1122.

Poag, C.W., and Sevon, W.D., 1989, A record of Appalachian denudation in postrift Mesozoic and Cenozoic sedimentary deposits of the US middle Atlantic continental margin, Geomorphology, v. 2, p. 119-157.

Pratson, L.F., and Coakley, B.J., 1996, A model for the headward erosion of submarine canyons induced by downslope-eroding sediment flows, Geological Society of America Bulletin, v. 108, p. 225-234.

Pratson, L.F., Ryan, W.B., Mountain, G.S., and Twichell, D.C., 1994, Submarine canyon initiation by downslope-eroding sediment flows; evidence in late Cenozoic strata on the New Jersey continental slope, Geological Society of America Bulletin, v. 106, p. 395-412.

Robb, J.M., 1990, Groundwater processes in the submarine environment, *in* Higgins, C.G., and Coates, D.R., eds., Groundwater Geomorphology: The Role of Subsurface Water in Earth-Surface Processes and Landforms, Volume 252, Boulder, Geological Society of America, p. 267-281.

Rona, P.A., 1969, Middle Atlantic continental slope of United States; deposition and erosion, AAPG Bulletin, v. 53, p. 1453-1465.

Rubey, W.W. and Hubbert, M.K., 1959, Overthrust belt in geosynclinal area of western Wyoming in light of fluid-pressure hypothesis: role of fluid pressure in mechanics of overthrust faulting, GSA Bulletin, 70, p. 167-205.

Shepard, F.P., 1981, Submarine canyons: multiple causes and long-time persistence, AAPG Bulletin, v. 65, p. 1062-1077.

Shipboard Scientific Party, 1998, Site 1073, *in* Austin Jr., J.A., Christie-Blick, N., Malone, M.J., *et al*., eds., Proceedings of the Ocean Drilling Program, Initial Reports, Volume 174A, College Station, Ocean Drilling Program, p. 153-191.

Terzaghi, K., 1943, Theoretical Soil Mechanics, London, Chapman and Hall, 510 p.

Twichell, D.C., and Roberts, D.G., 1982, Morphology, distribution, and development of submarine canyons on the United States Atlantic continental slope between Hudson and Baltimore Canyons, Geology, v. 10, p. 408-412.

Appendix C: Physical Modeling

Overview

Preliminary physical models of a continental slope demonstrate how fluid flow within high permeability conduits can initiate sedimentary failures near the slopeward termination of the conduit where overburden is thin. Focussed flow and failure created in the experiments allow observation and measurement of the hydrodynamic conditions during slope failures. The experimental results provide data to test theoretical and numerical models that couple sedimentation, fluid flow, and slope stability. Advancements of the model will provide quantitative results that will characterize the factors (e.g., permeability, angle of slope, overpressure) that control the styles and rates of failures on low-angle slopes. Comparison of experimental and theoretical results will be useful for extending our analysis and understanding of flow and failure in geologic settings.

Introduction

Fluid pressures that approach the lithostatic stress can produce unstable conditions on submarine sedimentary slopes. The origin and maintenance of these elevated pressures are a function of the sedimentation rate, bulk compressibility, permeability, and geometry of the system (e.g., Gibson, 1958; Koppula and Morgenstern, 1982; Bethke, 1986). In regions with low effective stress, slight variations in total stress or fluid pressure can result in slope

failure, even on nearly horizontal slopes (e.g. Rubey and Hubbert, 1959; Schwarz, 1982; Iverson *et al*., 1997). Failures of this type have been documented on slopes less than 1° (Schwarz, 1982; Hampton *et al*., 1996).

Failure can occur as slump blocks that rotate and move as cohesive blocks, as fluidized density currents, or as erosion of individual grains through groundwater sapping. The rates at which these failures occur also varies and this contributes to the impacts of the failure events. For example large, rapid failures can generate large waves that are devastating to shorelines, subsea infrastructure, and society. To better understand the potential for failure, the mechanics controlling failure and the rates of failure, we constructed a physical model in which pressure gradients and stratigraphy can be controlled. This design allows the evaluation of how fluid pressures, lithology, and stratigraphy influence the style and rates of submarine slope failures.

Background

Submarine failures and instability along low-angle failure planes have been documented at many locations (e.g., Rubey and Hubbert, 1959; Shepard, 1981). Previous studies of natural failures characterized run-out distances and volume of failed sediments (e.g., Iverson, 1997; Iverson *et al*., 1997). Other studies described how overpressure, earthquakes, and slope oversteepening may have produced these failures (Johnson, 1939; Rona and Clay, 1967; Rona, 1969; Shepard, 1981; Robb, 1990; Mello and Pratson, 1999). In this study, we use experiments to link failure mechanisms with failure type. We consider two end-

member categories for failure: (1) Mohr-Coulomb failure (see discussions in Hubbert and

Rubey, 1959 and Schwarz, 1982); and (2) liquefaction (see discussion in Iverson *et al.*,

1997). Mohr-Coulomb failure (Figure 3.1A) is the results of a critical shear stress along a

plane subject to a defined normal effective stress. It can be described as

$$\tau = \sigma' \tan\phi + c \qquad . \tag{C1}$$

τ is the shear stress on the failure plane, σ' is the normal effective stress on the failure sur-

face, ϕ is the angle of internal friction for the sediments, and c is the cohesive strength of

the sediment. σ' is a function of the total normal stress (σ) and the total fluid pressure (p)

$$\sigma' = \sigma - p \qquad . \tag{C2}$$

The shear stress at any depth in the sedimentary section can be defined as

$$\tau = (\rho_b - \rho_w)gh\sin\alpha \qquad , \tag{C3}$$

where ρ_b is the bulk density, ρ_w is the density of water, g is the acceleration due to gravity,

h is the vertical depth measured from the sediment surface to the location of interest, and

α is the angle of the slope.

(A)

(B)
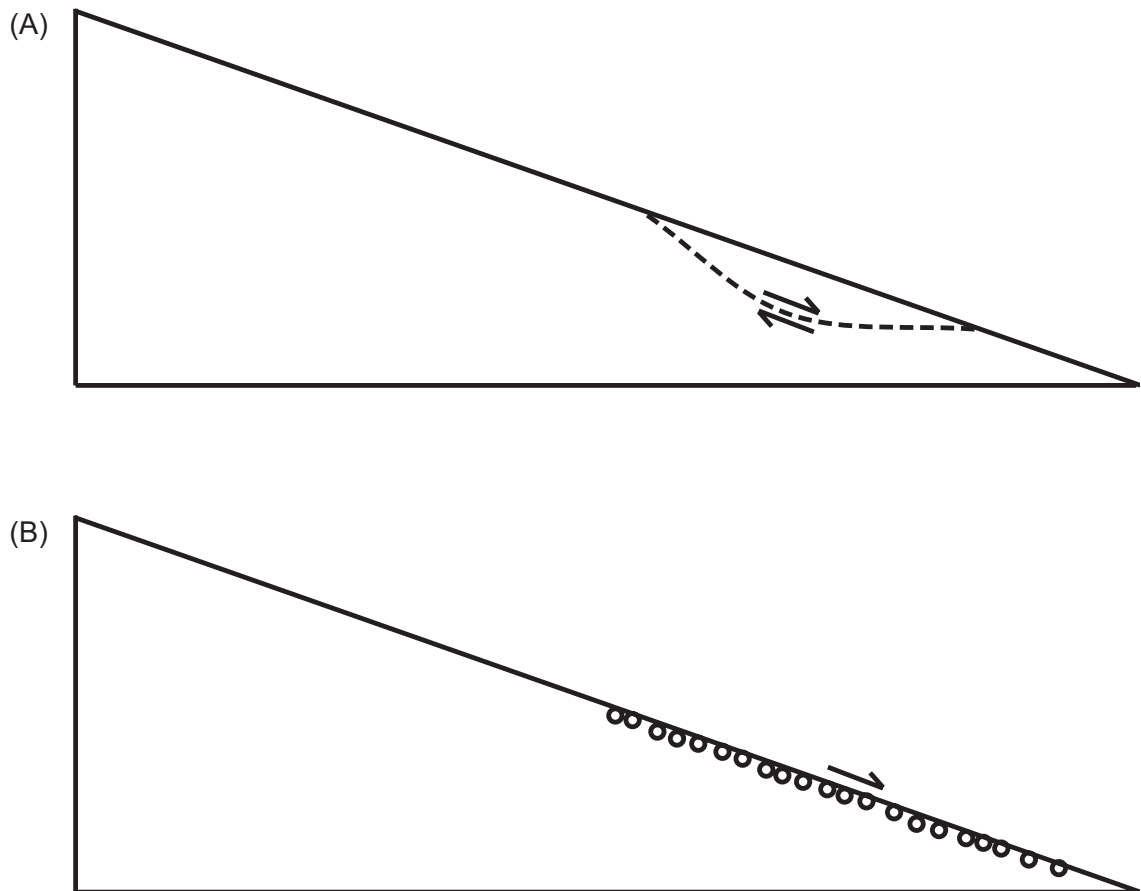
Figure C.1: Cartoon of failure types that can be initiated by high fluid pressures on continental slopes. (A) Mohr-Coulomb failure where sediments fail along a defined failure surface. (B) Liquefaction and grain-flow on a slope where failed sediments behave like a fluid and flow downslope.

The overpressure (P^*) required for Mohr-Coulomb failure can be determined with Equations C1, C2, and C3, and assuming that the sediments have zero cohesive strength and that the infinite slope approximation is valid (e.g., Lambe and Whitman, 1979),

$$P^* = (\rho_b - \rho_w)gh\left(1 - \frac{\sin\alpha}{\tan\phi}\right) \qquad . \tag{C4}$$

Liquefaction occurs in non-cohesive sediments when the effective stress is zero. Liquefied sediments on an inclined surface will flow downslope as a dense fluid (Figure C.1B). To generate liquefaction (or quick conditions), the vertical upward fluid pressure gradient must be equal to the downward stress gradient created by the sediments,

$$\frac{dp}{dz} = \frac{d\sigma}{dz} = \rho_b g \qquad . \tag{C5}$$

The two failure models are inherently different. Mohr-Coulomb analysis predicts shear failure to occur under a positive effective stress, whereas liquefaction requires zero effective stress for failure. They both, however, depend on overpressure and thus the hydrogeology. Few studies have used experimental approaches to study the linkage between stress-state, fluid pressure, and the type of failure (e.g, Howard and McLane, 1988). One obstacle that hinders these studies is that typical observations and analyses are of pre- or post-failure sediments. Rarely are observatories in place to gather data during a failure event. A controlled, physical experiment provides the opportunity to make observations on fluid

pressures, total stress, and types of failures. These experimental observations can be scaled to geological problems.

Experimental Design

To evaluate the relationship between hydrogeology and sedimentary failure, we constructed a controlled physical system (Figure C.2). The model allows (1) the input of any two-dimensional stratigraphic geometry, and (2) the control of the pressure gradient imposed on the geometry. The general stratigraphy employed in the model is a layered, heterogeneous system of fine- and coarse-sand (Figure C.2). The basal layer is fine-grained sand. The middle layer is coarse sand to simulate a conductive, sandy aquifer, similar to aquifers that exist in some continental shelf and slope settings. The top, confining layer is fine-grained sand that merges with the basal layer to completely enclose the aquifer (Figure C.2). This geometry and permeability structure is based on observations of the U.S. mid-Atlantic continental slope, a system that has adjacent failed and stable slopes (Veatch and Smith, 1939; Hampson and Robb, 1984; Poag and Mountain, 1987; Mountain *et al*., 1996).

The model has a no flow barrier (Figure C.2) that simulates a groundwater divide separating seaward and landward fluid migration while facilitating pressure control for the model. In a rapidly deposited margin, this divide corresponds to the location of the highest sedimentation rate, if topographic-driven flow is negligible (e.g. Gordon and Flemings, 1999).
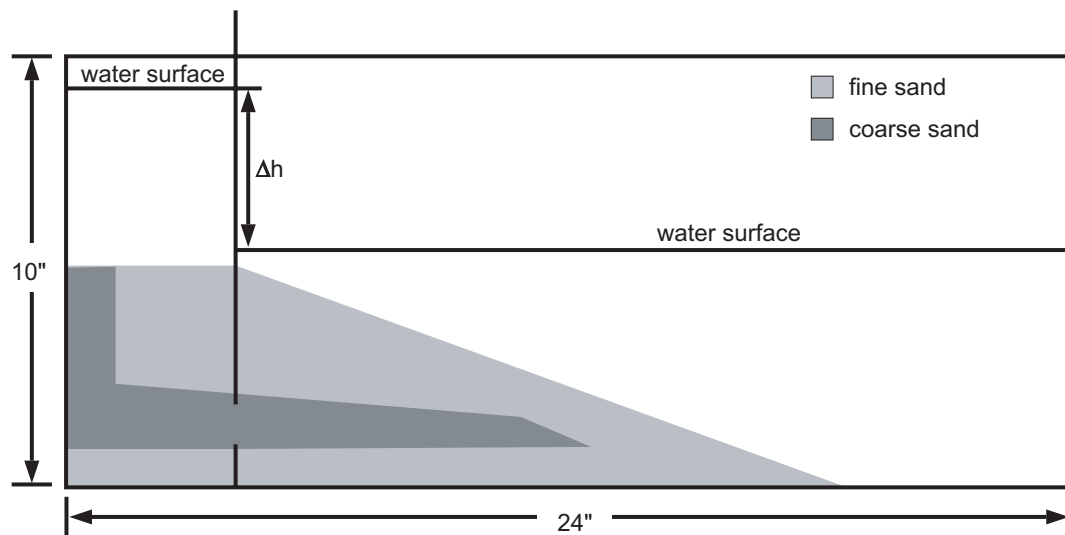
Figure C.2: Illustration of the physical model. The coarse sand is the aquifer through which focussed flow occurs. This flow that leads to the failures illustrated in Figure C.1. The model allows the input of a defined head differential (Δh) to impose overpressure and to initiate failure on the slope.

A small gap near the base of this barrier provides a means to impose overpressure ($\Delta h \rho_w g$) on the aquifer system. Overpressure is controlled in the aquifer because that is where rapid pressure transfer will occur in a geologic system where flow focussing along high permeability conduits exists (e.g. Phillips, 1991; Dugan and Flemings, 2000; Saffer *et al*., 2000). In a completely sealed system (i.e., confining layer of zero permeability), the aquifer would equilibrate with the imposed overpressure (Stump, 1998; Flemings *et al*., 2002). The confining layer in the model has finite permeability, therefore excess pressure in the aquifer will drive flow through the confining layer and can create unstable conditions.

The existing model and simulations provide quantitative measurements of failure. The clear, Plexiglas® model allows the stratigraphic geometry to be traced pre- and post-failure. The clear model also allows the entire simulation to be viewed and recorded. This provides observations of where failures begin and how they progress, and allows volume of the failure to be measured. A series of piezometers were installed in the system to measure hydraulic head at multiple locations during the experiments. With these data, we can calculate the pressure and effective stress throughout the experimental system. Pressure data can be coupled with permeability data to model the fluid flow occurring before, during, and after failure. Qualitative observations are also made during experiments including the form of the failures (grain flow, glide plane, slump blocks, etc.) and the progression of failures (one event, multiple events, coupled events).

Results

Qualitative observations were made on the prototype system. Initial experimental efforts focussed on establishing a system that did not leak and that had reproducible results. Flaws with preliminary experiments included: (1) an aquifer with permeability that was too low, which resulted in flow between permeability units not through them; (2) fluid leakage along the no flow barrier creating sand expulsion (e.g. volcanoes) at the upslope section; and (3) displacement of sediment in the small gap that yielded unrestricted flow, instead of flow through porous media.

After some experimental modifications, a working and reproducible system was developed and the preliminary results were promising. We generated grain flows with a system of sand (confining unit) and gravel (aquifer). These sediment flows began at the truncation of the permeable, gravel aquifer and progressed upslope. The progression of failure upslope was accelerated when the head differential was continually increased after the initial failure.

Discussion

Preliminary experimental results agree with Mohr-Coulomb and liquefaction failure criteria, but additional experiments are required to constrain the conditions that produce different types of failure. Failure began above the pinch-out of the aquifer, which is consistent with numerical models of focussed flow within differentially loaded systems (e.g., Dugan

and Flemings, 2002). Numerical models predict that effective stresses will be least where the overburden over the aquifer is thinnest, thus increased pressure will drive Mohr-Coulomb failure in these regions (Figure C.3). Where overburden is thinnest over the aquifer, the pressure gradient from the aquifer to the sea floor is highest, therefore the potential for liquefaction increases. Future experiments will be performed to describe the causes and controls of Mohr-Coulomb versus liquefaction failure.

Future Models and Analyses

With the current model and a qualitative inspection of its behavior, we can begin to collect data to understand flow and failure. Below I outline the key measurements and analyses that can be done to expand the model.

A constant geometry will be run for every simulation. All experiments will have nine pressure gauges: three in the permeable aquifer and six in the confining sediments. This will provide an image of what is the hydrologic conditions pre-, during- and post-failure. Total stress will also be calculated for the system (vertical stress based on bulk density and thickness; various scenarios for the horizontal stress such as constant stress ratio of poroelasticity). From this, the pressure increase required to liquefy the sediments or create Mohr-Coulomb failure can be calculated (Figure C.3). These calculations can also be used as a guideline when designing experiments.
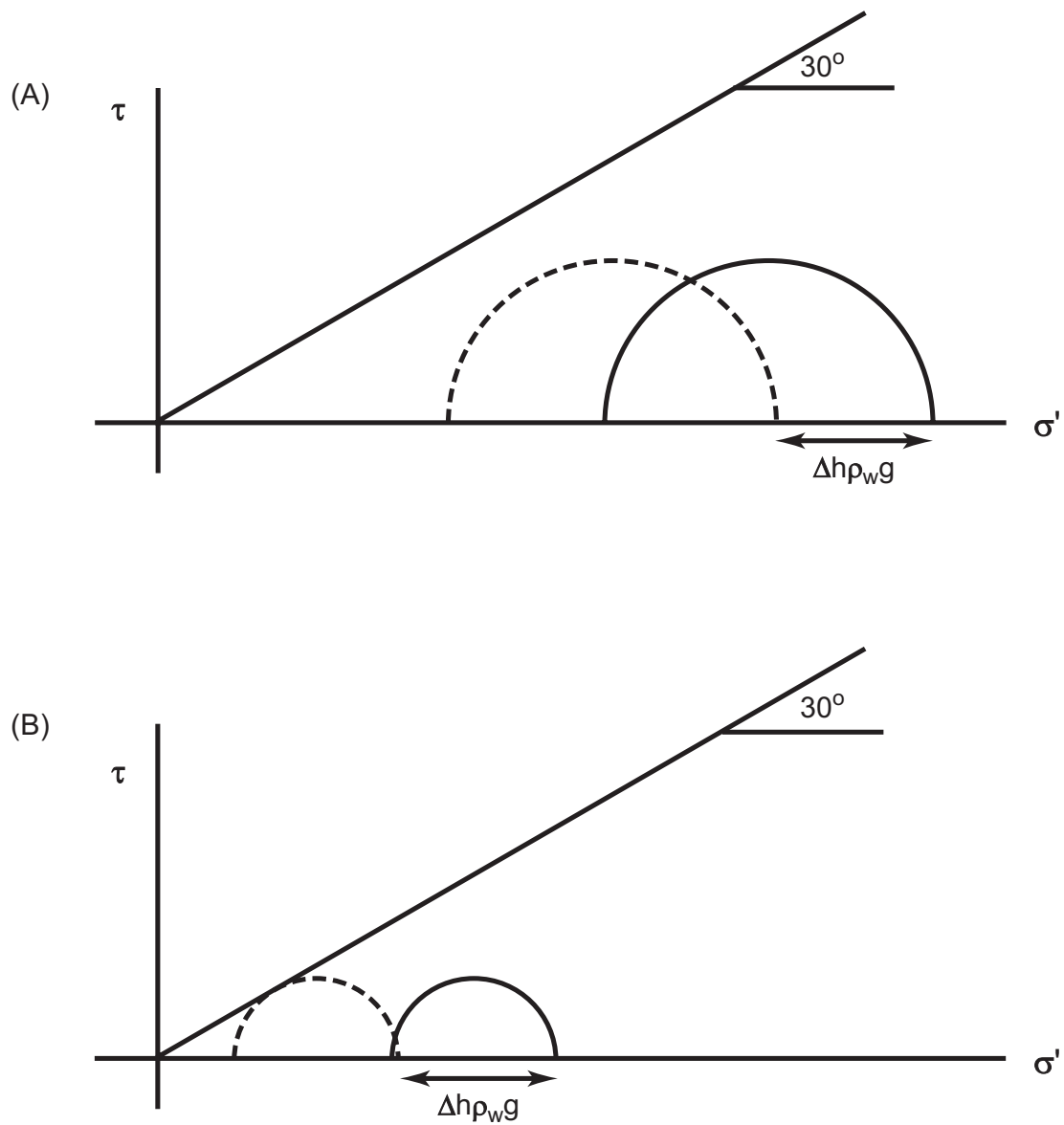
Figure C.3: Mohr-Coulomb analysis demonstrates the effects of an imposed head differential on the state of stress for the physical model. Solid circles are the stress before the overpressure is induced in the aquifer. Dashed circles are the state of effective stress after imposing the overpressure on the system. (A) Stress on the upper slope where overburden is thick. The excess pressure ($\Delta h \rho_w g$) decreases the effective stress but does not produce failure. (B) Stress on the lower slope near the termination of the aquifer. The same excess pressure drives the lower slope to failure because total stresses are low.

The same general stratigraphic geometry for all simulations with a series of confining layers will be evaluated. I will begin with a 100% fine-grained system (no aquifer) and then to a 100% coarse-grained system (all aquifer). These will be base cases for comparison to layered systems (e.g., Figure C.2). A suite of confining layer mixtures will be evaluated, each having a different percentage of fine-grained sand and silt/clay. The increasing silt/clay content will decrease the confining layer permeability and alter the flow system. Cohesion associated with silt and clay content may influence when grain flows stop and failure occurs as slump blocks.

Permeability measurements for the system will be made on each lithology of the system and on the overall system. This is required so we can expand the scale of the model back to geologic settings and problems. Each sample layer will also be tested for the natural angle of repose. This will be done to evaluate the relationships between the angle of the failure, the at-rest angle (post-failure) of the sediments and the angle that the sediments can sustain under hydrostatic conditions.

With these pressure and geometric data we can begin looking the data in terms of permeability contrast versus head differential for failure and characteristic time (or length) for failure. This should help determine the controlling parameters of failure style and failure rate. A series of controlled experiments will therefore provide datasets from which we can characterize failure criteria and test hydrodynamic models. The results will also provide insights on failure mechanisms that can be expanded to coupled flow, deformation, and failure in geologic settings where observations are limited.

References

Bethke, C.M., 1986, Inverse hydrologic analysis of the distribution and origin of gulf coast-type geopressured zones, Journal of Geophysical Research, 91(6), p. 6535-6545.

Dugan, B. and Flemings, P.B., 2000, Overpressure and fluid flow in the New Jersey continental slope: implications for slope failure and cold seeps, Science, 289, p. 288-291.

Dugan, B. and Flemings, P.B., 2002, Fluid flow and stability of the US continental slope offshore New Jersey from the Pleistocene to the present, Geofluids, 2, p. 137-146.

Flemings, P.B., Stump, B.B., Finkbeiner, T., and Zoback, M., 2002, Flow focussing in overpressured sandstones: theory, observations, and implications, American Journal of Science, 302, p. 827-855.

Gibson, R.E., 1958, The progress of consolidation in a clay layer increasing in thickness with time, Geotechnique, 8, p. 171-182.

Gordon, D.S. and Flemings, P.B., 1999, Two-dimensional modeling of groundwater flow in an evolving deltaic environment. In J.W. Harbaugh *et al*. (Eds.), Numerical experiments in stratigraphy; recent advancements in stratigraphic and sedimentologic computer simulations, p. 301-312.

Hampson, J.C., Jr. and Robb, J.M., 1984, A geologic map of the continental slope off New Jersey; Lindenkohl Canyon to Tom's Canyon, MIS-USGS, I-1608.

Hampton, M.A., Lee, H.J., and Locat, J., 1996, Submarine landslides, Reviews of Geophysics, 34(1), p. 33-59.

Howard, A.D. and McLane III, C.F., 1988, Erosion of cohesionless sediment by groundwater seepage, Water Resources Research, 24, p. 1659-1674.

Hubbert, M.K., and Rubey, W.W., 1959, Mechanics of fluid-filled porous solids and its application to overthrust faulting, part 1 of role of fluid pressure in mechanics of overthrust faulting, GSA Bulletin, 70(2), p. 115-166.

Iverson, R.M., 1997, The physics of debris flows, Reviews of Geophysics, 35(3), p. 245-296.

Iverson, R.M., Reid, M.E., and LaHusen, R.G., 1997, Debris-flow mobilization from landslides, Annual Review of Earth and Planetary Sciences, 25, p. 85-138.

Johnson, D., 1939, The origin of submarine canyons, Hafner, New York, 126p.

Koppula, S.D. and Morgenstern, N.R., 1982, On the consolidation of sedimenting clays, Canadian Geotechnical Journal, 19(3), p. 260-268.

Lambe, T.W. and Whitman, R.V., 1979, Soil Mechanics: SI Version, John Wiley & Sons, New York, 553 p.

Mello, U.T., and Pratson, L.F., 1999, Regional slope stability and slope-failure mechanics from the two-dimensional state of stress in an infinite slope, Marine Geology, 154(1-4), p. 339-356.

Mountain, G.S., Damuth, J.E., McHugh, C.M.G., Lorenzo, J.M., and Fulthorpe, C.S., 1996, Origin, reburial and significance of middle Miocene canyons, New Jersey, Proceedings of the ODP Scientific Results, 150, p. 283-292.

Phillips, O.M., 1991, Flow and reactions in permeable rocks, Cambridge University Press, 285p.

Poag, C.W. and Mountain, G.S. 1987, 30. Late Cretaceous and Cenozoic evolution of the New Jersey continental slope and upper rise: an integration of borehole data with seismic reflection profiles. In C.W. Poag *et al*. (Eds.), Initial Reports, DSDP, 95, p. 673-724.

Robb, J.M., 1990, Groundwater processes in the submarine environment. In C.G. Higgins and D.R. Coates (Eds.), Groundwater geomorphology: the role of subsurface water in Earth-surface processes and landforms, GSA, Boulder, p. 267-281.

Rona, P.A., 1969, Middle Atlantic continental slope of United States: deposition and erosion, AAPG Bulletin, 53, p. 1453-1465.

Rona, P.A., and Clay, C.S., 1967, Stratigraphy and structure along a continuous seismic reflection profile from Cape Hatteras, North Carolina to the Bermuda Rise, Journal of Geophysical Research, 72, p. 2107-2130.

Rubey W.W. and Hubbert, M.K., 1959, Overthrust belt in geosynclinal area of western Wyoming in light of fluid-pressure hypothesis, part 2 of role of fluid pressure in mechanics of overthrust faulting, GSA Bulletin, 70(2), p. 167-205.

Saffer, D.M., Silver, E.A., Fisher, A.T., Tobin, H., and Moran, K., 2000, Inferred pore pressures at the Costa Rica subduction zone: implications for dewatering processes, Earth & Planetary Science Letters, 177(3-4), p. 193-207.

Schwarz H-U., 1982, Subaqueous slope failures - experiments and modern occurrences, Contributions in Sedimentology 11, 116p.

Shepard, F.P., 1981, Submarine canyons; multiple causes and long-time persistence, AAPG Bulletin, 65(6), p. 1062-1077.

Stump, B.B., 1998, Illuminating basinal fluid flow in Eugene Island 330 (Gulf of Mexico) through in situ observations, deformation experiments, and hydrodynamic modeling, M.S. Thesis, Penn State University, University Park, Pennsylvania.

Veatch, A.C. and Smith, P.A., 1939, Atlantic submarine valleys of the United States and the Congo submarine valley, GSA Special Paper 7, 101p.

Vita

Brandon Dugan

Education

1997-2003   Ph.D., geosciences, Penn State University
                Thesis: Hydrodynamics of the US Mid-Atlantic Continental
                Slope, Offshore New Jersey
1993-1997   B.GeoE., geological engineering, University of Minnesota, Twin Cities
                Summa Cum Laude Honors

Research Experience

1997-present   Graduate research assistant, Penn State University
Aug-Sept 2001   Visiting scientist, Conoco Inc.
                Seismic data processing, velocity modeling, fluid pressure prediction
May-July 2001   Visiting scientist, ExxonMobil Upstream Research Company
                Deformation experiments on unconsolidated sediments
Jan-Mar 2001   Physical properties scientist, ODP Leg 194, Marion Plateau
                Measured and analyzed bulk physical properties of sediments
June-Aug 1998   Intern, Exxon Production Research Company
                Numerical modeling of secondary migration in faulted reservoirs

Teaching Experience

Fall 1998/9   Teaching assistant, multi-channel seismic processing and interpretation

Selected Publications

Dugan, B. and P.B. Flemings, 2002, Fluid flow and stability of the US continental slope
     offshore New Jersey from the Pleistocene to the present, *Geofluids* 2(2), p. 137-146.
Dugan, B. and P.B. Flemings, 2000, Overpressure and fluid flow in the New Jersey
     continental slope: Implications for slope failure and cold seeps, *Science* 289, p. 288-
     291.

Honors and Awards

2002-2003   PSU Alumni Association Dissertation Award
2001-2002   Link Foundation Fellow in Ocean Engineering and Instrumentation
2001-2003   NASA Space Grant Fellow
2001-2002   Scholten-Williams-Wright Scholarship
2000-2001   Shell Foundation Doctoral Fellow
2000-2001   College of Earth and Mineral Sciences Muan Fellow
1999-2000   JOI/USSAC Ocean Drilling Fellow
1998-1999   Exxon Fellow in Quantitative Geosciences
2000   Session chair for hydrodynamics session at Fall AGU meeting
2000   Invited speaker at PSU Graduate Student Convocation
2000   Geosciences colloquium speaker, University of Oregon
1999   Outstanding student paper in Ocean Sciences, Fall AGU meeting

Professional Affiliations

AAAS, AAPG, AGU, GSA, Sigma Xi